

---

# Studies on the Z boson reconstruction in $t\bar{t}Z$ events at the ATLAS detector

---

Ludwig-Maximilians-Universität München  
Master thesis at the Faculty of Physics



submitted by

**Maximilian Riepe**

Munich, 10<sup>th</sup> September 2020

**Supervisor:** M.Sc. Florian Fischer  
**Examiner:** Prof. Dr. Otmar Biebel

---

# Studien zur Z-Boson Rekonstruktion in $t\bar{t}Z$ Events am ATLAS Detektor

---

Ludwig-Maximilians-Universität München  
Masterarbeit an der Fakultät für Physik



vorgelegt von

**Maximilian Riepe**

München, 10. September 2020

**Betreuer:** M.Sc. Florian Fischer  
**Prüfer:** Prof. Dr. Otmar Biebel

# Abstract

One well suited process for extending our knowledge of the Standard Model of particle physics is the associated production of a top-anti-top quark pair with a Z boson. Since measuring this cross section provides direct sensitivity to the coupling between the top quark and the Z boson, a precise measurement in this regard would allow for testing many models of physics beyond the Standard Model which expect a significantly varied top-Z coupling. Moreover,  $t\bar{t}Z$  events represent an important background in  $t\bar{t}H$  analyses wherefore an improved understanding of  $t\bar{t}Z$  processes could help with their suppression in Higgs physics research.

To assist  $t\bar{t}Z$  studies in general, this analysis focuses on improving the reconstruction of Z bosons in events with specifically three or four final state leptons. There especially, combinatoric effects complicate the reconstruction and directly impact the performance of the unfolding technique used in differential  $t\bar{t}Z$  cross section measurements. Therefore, the goal is to reduce the influence of events which are wrongly reconstructed or stem from other particle configurations than  $t\bar{t}Z$  on  $t\bar{t}Z$  studies. In order to accomplish that, different truth-matching based reference histogram methods are investigated, tested and in the end compared among each other, as well as to the one currently employed by the ATLAS  $t\bar{t}Z$  group with regard to their reconstruction efficiency. For all that, we use Monte Carlo simulations, corresponding to the 2018 LHC Run-2 data taking period at the ATLAS experiment at a center-of-mass energy of 13 TeV, normalized to an integrated luminosity of  $66 \text{ fb}^{-1}$ .



# Kurzfassung

Ein für die Erweiterung unseres Verständnisses des Standardmodells der Teilchenphysik gut geeigneter Prozess ist die vereinte Produktion eines top Quark Paares mit der eines Z Bosons. Da die Messung des Wirkungsquerschnitts dieser Prozesse direkte Rückschlüsse auf die Kopplung zwischen top Quarks und Z Bosonen zulässt, würde höhere Messpräzision die Möglichkeit bieten, Physik und Theorien jenseits des Standardmodells zu testen, welche signifikant unterschiedliche Dimensionen dieser Größe voraussagen. Darüber hinaus stellen  $t\bar{t}Z$  Prozesse einen wichtigen Signaluntergrund in  $t\bar{t}H$  Analysen dar, der durch ein vertieftes Verständnis besser vom Signal getrennt werden könnte.

Um demnach Untersuchungen zu  $t\bar{t}Z$  Events zu unterstützen, zielt diese Studie darauf ab, die Rekonstruktion der Z Bosonen speziell für Zerfallskanäle mit drei und vier Leptonen im Endzustand zu verbessern. Gerade in diesen Signalregionen komplizieren kombinatorische Effekte diese Rekonstruktion, welche währenddessen zusätzlich negative Auswirkungen auf die Unfolding-Methoden der differentiellen  $t\bar{t}Z$  Wirkungsquerschnittsmessungen hat. Daher ist es das Ziel dieser Arbeit, den Einfluss von Events, die falsch rekonstruiert wurden, beziehungsweise erst gar nicht von  $t\bar{t}Z$  Konfigurationen stammen, auf  $t\bar{t}Z$  Analysen zu verringern. Um dies zu erreichen, werden basierend auf einem Teilchenabgleich mit truth-Informationen verschiedene Variablen auf ihre Eignung in Z Boson Rekonstruktionen untersucht. Aus den geeigneten Variablen konstruierte Referenzhistogram-Methoden werden anschließend in Bezug auf ihre Effizienz Z Bosonen richtig zu rekonstruieren untereinander, so wie auch mit der momentan von der ATLAS  $t\bar{t}Z$  Arbeitsgruppe verwendeten Z Boson Rekonstruktionsstrategie verglichen. Dazu werden zu einer Luminosität von  $66 \text{ fb}^{-1}$  normalisierte Monte Carlo Simulationsdaten verwendet, die den 2018 mit dem ATLAS Detektor aufgenommenen Daten des LHC Run-2 bei 13 TeV Schwerpunktsenergie entsprechen.



# Contents

|  |           |
|--|-----------|
| <b>Abstract</b>                                      | <b>I</b>  |
| <b>Contents</b>                                      | <b>V</b>  |
| <b>1 Introduction</b>                                | <b>1</b>  |
| <b>2 Theory</b>                                      | <b>3</b>  |
| 2.1 The Standard model of particle physics . . . . . | 3         |
| 2.1.1 Particle content and interactions . . . . .    | 3         |
| 2.1.2 Limitations and extensions . . . . .           | 8         |
| 2.2 The top quark . . . . .                          | 8         |
| 2.2.1 Top quark production . . . . .                 | 9         |
| 2.2.2 Top quark decay . . . . .                      | 10        |
| 2.3 The Z boson . . . . .                            | 12        |
| 2.3.1 Z boson production . . . . .                   | 12        |
| 2.3.2 Z boson decay . . . . .                        | 15        |
| 2.4 $t\bar{t}Z$ events . . . . .                     | 16        |
| 2.4.1 $t\bar{t}Z$ production . . . . .               | 16        |
| 2.4.2 $t\bar{t}Z$ decay . . . . .                    | 17        |
| <b>3 Experimental setup</b>                          | <b>19</b> |
| 3.1 CERN . . . . .                                   | 19        |
| 3.2 The Large Hadron Collider . . . . .              | 20        |
| 3.3 The ATLAS experiment . . . . .                   | 20        |
| 3.3.1 Detector sub-systems . . . . .                 | 20        |
| 3.3.2 Trigger and data acquisition . . . . .         | 22        |
| 3.3.3 Coordinate system . . . . .                    | 23        |
| <b>4 Monte Carlo data simulation</b>                 | <b>27</b> |
| 4.1 Monte Carlo generation . . . . .                 | 27        |
| 4.2 Monte Carlo generators . . . . .                 | 29        |
| 4.3 Monte Carlo samples . . . . .                    | 29        |
| 4.3.1 Detector-level data . . . . .                  | 30        |
| 4.3.2 Truth-level data . . . . .                     | 31        |

|          |   |           |
|----------|---|-----------|
| 4.3.3    | Final state differences . . . . .   | 31        |
| <b>5</b> | <b>Object and event selections</b>  | <b>33</b> |
| 5.1      | Object definitions . . . . .  | 33        |
| 5.2      | Relevant decay channels for Z boson reconstruction . . . . .                      | 35        |
| 5.2.1    | Exclusion of two lepton events . . . . .  | 35        |
| 5.2.2    | Exclusion of events containing tauons . . . . .                                   | 35        |
| 5.3      | Signal regions . . . . .  | 37        |
| 5.4      | Final event selection . . . . .   | 39        |
| 5.4.1    | Summary of selected decay channels . . . . .                                      | 40        |
| <b>6</b> | <b>Z boson reconstruction</b>   | <b>43</b> |
| 6.1      | Motivation and status quo . . . . .   | 43        |
| 6.2      | Method of reconstruction . . . . .  | 45        |
| 6.2.1    | Truth-matching . . . . .  | 45        |
| 6.2.2    | Reference histograms . . . . .  | 46        |
| 6.2.3    | Implementation . . . . .  | 46        |
| 6.3      | Variable selection . . . . .  | 46        |
| 6.3.1    | $m_{\ell\ell}$ and $\Delta m_Z$ . . . . .   | 47        |
| 6.3.2    | $\Delta R(\ell, \ell)$ . . . . .  | 49        |
| 6.3.3    | $E_T^{miss}$ . . . . .  | 50        |
| 6.3.4    | $\Delta R(\ell, E_T^{miss})$ . . . . .  | 51        |
| 6.3.5    | $\Delta R(Z_{\ell\ell}, E_T^{miss})$ . . . . .                                    | 53        |
| 6.3.6    | $p_T$ -correlation . . . . .  | 54        |
| 6.4      | Reference histograms . . . . .  | 56        |
| 6.4.1    | 1D reference histograms . . . . .   | 56        |
| 6.4.2    | 2D reference histograms . . . . .   | 58        |
| 6.4.3    | 3D reference histograms . . . . .   | 60        |
| 6.4.4    | Masking . . . . .   | 60        |
| 6.5      | Evaluation method . . . . .   | 64        |
| 6.5.1    | Truth- vs. detector-level evaluation . . . . .                                    | 64        |
| 6.5.2    | Uncertainties . . . . .   | 65        |
| 6.6      | Reconstruction efficiencies . . . . .   | 65        |
| 6.6.1    | 1D reference histogram efficiencies . . . . .                                     | 66        |
| 6.6.2    | 2D reference histogram efficiencies . . . . .                                     | 70        |
| 6.6.3    | 3D reference histogram efficiencies . . . . .                                     | 72        |
| 6.6.4    | Method comparison and efficiency summary . . . . .                                | 74        |
| <b>7</b> | <b>Conclusion</b>   | <b>81</b> |
| <b>A</b> | <b>Appendix</b>   | <b>83</b> |
| A.1      | Previously used three lepton signal regions . . . . .                             | 83        |
| A.2      | Signal region specific efficiencies for superior reconstruction methods . . . . . | 84        |

|                                  |           |
|----------------------------------|-----------|
| <b>List of Figures</b>           | <b>91</b> |
| <b>List of Tables</b>            | <b>93</b> |
| <b>Bibliography</b>              | <b>95</b> |
| <b>Eidesstattliche Erklärung</b> | <b>99</b> |

# 1 | Introduction

Along the way from the first mentions of subatomic particles to our current understanding of the smallest structures in our universe a lot of breakthroughs have been achieved. With the discovery of the electron in 1897 [1], J. J. Thomson paved the way for years of research in the field of particle physics to come. Since then, a plethora of theories predicted different ideas and structures of the most fundamental particles of which the Standard Model of particle physics is the most extensively tested and renowned one today. The Higgs boson's discovery in 2012 by the ATLAS and CMS Collaborations [2, 3] confirmed its last to remain undiscovered particle, consolidating its place in particle physics even further. However, despite explaining most to this day observed phenomena with great precision, this theory is not a complete one. Besides some open questions, which seem not to fit the Standard Model's descriptions, the ones it describes well rely on many free parameters a couple of which are not yet very well constrained by measurements.

A major role in the latter mentioned free parameters plays the top quark. As one of the half-integer spin fermions of the Standard Model, and especially as the heaviest of all the included particles in that theory, its mass, as well as its couplings to other particles are examples of free parameters themselves. With more and more powerful particle accelerators like the Large Hadron Collider at CERN, measurements of the in 1995 [4] discovered top quark became more accessible on a larger, more precise scale only recently.

This analysis focuses on the special case of the production of a top-anti-top quark pair in association with a Z boson, a very massive whole-integer spin boson, to investigate a strategy for a more efficient reconstruction of these events and especially the Z boson. Specifically it is aimed for higher efficiencies in the  $t\bar{t}Z$  decay channels with three or four leptons in their final states final state. This would improve the general ability to accurately detect these events in the first place, which is necessary to be able to precisely measure any  $t\bar{t}Z$  properties. The importance of  $t\bar{t}Z$  research stems not only from the, thereby, possible measurement of the  $t$ -Z-coupling, but also from  $t\bar{t}Z$  events being a main background in  $t\bar{t}H$  analyses. A better understanding of the associated production of a top quark pair with a Z boson, therefore, could lead to an improved background rejection in Higgs physics research.

The for investigation chosen Z boson reconstruction method is based on a lepton-wise truth-matching approach with a reference histogram implementation the foundation of which is built by Monte Carlo simulation data corresponding to the 2018 LHC Run-2 data taking period of the ATLAS Collaboration at the Large Hadron Collider at 13 TeV. This data set, therefore, is normalized to an integrated luminosity of 66 inverse femtobarn ( $\text{fb}^{-1}$ ) and consists of  $t\bar{t}Z$  events with leptonically decaying Z bosons producing pairs of either  $e^+e^-$ ,

$\mu^+\mu^-$  or  $\tau^+\tau^-$ . To actually investigate different iterations of the method, first, a selection of variables, suited for the separation of signal and background, namely Z boson decay lepton combinations and other opposite-sign-same-flavour lepton pairings, respectively, is made. After that, reference histograms based on the selected variables are built with support of truth-matching information. Finally, the efficiencies of the found methods are presented and compared to one another, as well as to the currently in the ATLAS  $t\bar{t}Z$  group's ATLAS-CONF-2020-028 analysis [5] used method, in order to determine the best performing one for the Z boson reconstruction.

The following chapter 2 presents an overview of the Standard Model's relevant aspects for  $t\bar{t}Z$  events, while chapter 3 describes the underlying experimental set-up. In chapter 4 used Monte Carlo data samples are explained with respective cuts and selections for events shown in chapter 5. Thereafter, chapter 6 presents the previously mentioned steps and results of the Z boson reconstruction from which a conclusion is drawn in chapter 7.

For everything presented in this analysis natural units ( $\hbar = c = 1$ ), as well as the English notation for decimal numbers ( $\pi = 3.1415\dots$ ) are used. Furthermore, for Feynman diagrams the convention of time passing in positive x direction and traversed space being displayed on the y axis is employed.

## 2 | Theory

### 2.1 The Standard model of particle physics

Since its development in the 1960s and 1970s, the *Standard Model of Particles* (SM) successfully describes the smallest, most fundamental building blocks of our world's matter as well as all their non-gravitative interactions. By unifying the electroweak theory, established by S. Glashow, A. Salam and S. Weinberg, a combined description of electromagnetism and weak interactions, with that of the strong nuclear force, today formulated through quantum chromodynamics, the SM yields a combined description of three out of the four fundamental forces of our universe. Withstanding various types of experimental testing and measurements over the years, the SM really consolidated its place in particle physics with the confirmation of its to this point last predicted yet missing particle in 2012 by the ATLAS [2] and the CMS Collaborations [3] at CERN's Large Hadron Collider.

Despite the success of the Standard Model, it suffers from a few shortcomings and is not able to answer every question raised in its field. First and foremost gravity, the fourth fundamental force, is not included in this theory. Other examples like dark matter, dark energy, the matter-antimatter asymmetry as well as neutrino mass possibly larger than zero to just name a few, are beyond the Standard Model's scope.

To build a foundation for this analysis a brief overview of the, in this regard, relevant aspects of the Standard Model is given in the following chapter, which is based on [6], [7] and [8] if not stated otherwise.

#### 2.1.1 Particle content and interactions

Particles of the SM are generally separated into two groups of either half-integer spin, so called *fermions*, or whole-integer spin, so called bosons. Both are with no known substructure, expected to be point-like and play fundamentally different roles in the Standard Model's description of our universe.

On the one hand, there are fermions, named after their behaviour according to Fermi-Dirac statistics. These 12 particles make up all matter and are further subdivided twice. For the first part into two groups, 6 *leptons* and 6 *quarks* based on, among other things, them having or lacking a *colour charge* of values either red (r), blue (b) or green (g). And for the second part quarks and leptons each into a generation structure of three pairs of differently charged

particles per grouping. The six quarks named *up* ( $u$ ), *down* ( $d$ ), *charm* ( $c$ ), *strange* ( $s$ ), *top* ( $t$ ) and *bottom* ( $b$ ), are massive and have a colour charge, as well as an electric charge  $Q$  of either  $+\frac{2}{3}e$  or  $-\frac{1}{3}e$ . Accordingly, they are termed as *up-type* and *down-type* quark, respectively (tables 2.1 and 2.2). Leptons, besides not being colour charged, differ from quarks in their whole-integer electric charge  $Q$ . They come with either electric charges of  $Q = -1e$  and massive, in the cases of electrons  $e^-$ , muons  $\mu^-$  and tauons  $\tau^-$  or as electrically neutral particles of  $Q = 0$  in the form of the *neutrinos*  $\nu_e$ ,  $\nu_\mu$  or  $\nu_\tau$ . The latter mentioned neutrinos are labelled in their indices according to their generation partner and are massless, as predicted by the SM. However, at this time their masses are not confirmed to be zero. On the contrary, experiments by the Super-Kamiokande Collaboration published first in 1998 [9] and later backed by work of the Sudbury Neutrino Observatory suggest a non-zero neutrino mass due to neutrino oscillations. These results are often treated as the first evidence for beyond SM physics. By measurements of different experiments the neutrino masses are confirmed to be smaller than the upper mass limits given in table 2.2.

| Fermions | Generations |           |            | electr. charge  | colour charge | third component of the weak Isospin |              | Spin          |
|----------|-------------|-----------|------------|-----------------|---------------|-------------------------------------|--------------|---------------|
|          | 1           | 2         | 3          |                 |               | left-handed                         | right-handed |               |
| Leptons  | $\nu_e$     | $\nu_\mu$ | $\nu_\tau$ | $\pm 0e$        | —             | +1/2                                | —            | $\frac{1}{2}$ |
|          | $e^-$       | $\mu^-$   | $\tau^-$   | $-1e$           |               | -1/2                                | 0            |               |
| Quarks   | $u$         | $c$       | $t$        | $+\frac{2}{3}e$ | $r, b, g$     | +1/2                                | 0            | $\frac{1}{2}$ |
|          | $d$         | $s$       | $b$        | $-\frac{1}{3}e$ |               | -1/2                                | 0            |               |

Table 2.1: Fermions of the Standard Model [10, 11].

Table 2.2 also shows the range of the fermion masses which spans over seven orders of magnitude, not including neutrinos. In general the particles of earlier generations are lighter than those of the subsequent ones.

In addition to the particles listed in table 2.2, for each fermion there is an *anti-fermion* of the exact same mass and opposite electric and colour charge as well as opposed spin. These anti-particles are denoted by a macron on top of the abbreviated notation for quarks and neutrinos ( $t \rightarrow \bar{t}$  &  $\nu_e \rightarrow \bar{\nu}_e$ ) while for charged leptons the sign in the exponent is flipped ( $e^- \rightarrow e^+$ ).

| Generations | Quarks  |                                    | Leptons    |                                 |
|-------------|---------|------------------------------------|------------|---------------------------------|
|             | Flavour | Mass [MeV]                         | Flavour    | Mass [MeV]                      |
| 1           | $u$     | $m_u \approx 2.16_{-0.26}^{+0.49}$ | $e^-$      | $m_e \approx 0.511$             |
|             | $d$     | $m_d \approx 4.67_{-0.17}^{+0.48}$ | $\nu_e$    | $m_{\nu_e} < 1.1 \cdot 10^{-6}$ |
| 2           | $c$     | $m_c \approx 1270_{-20}^{+20}$     | $\mu^-$    | $m_\mu \approx 105.7$           |
|             | $s$     | $m_s \approx 93_{-5}^{+11}$        | $\nu_\mu$  | $m_{\nu_\mu} < 0.19$            |
| 3           | $t$     | $m_t \approx 172760_{-300}^{+300}$ | $\tau^-$   | $m_\tau \approx 1777$           |
|             | $b$     | $m_b \approx 4180_{-20}^{+30}$     | $\nu_\tau$ | $m_{\nu_\tau} < 18.2$           |

Table 2.2: Masses of fermions [10].

On the other hand, apart from fermions, there are the whole-integer-spin particles called vector- or gauge *bosons*. They behave according to Bose-Einstein statistics, hence their name, and are responsible for the mediation of all up until now observed interactions described by the SM. Whether or not any particle of the SM is interacting electromagnetically, weakly or strongly depends on their coupling to the corresponding gauge boson of the forces, indicated in figure 2.1, and of what magnitude this coupling is. One important aspect in this regard is self-coupling of the gauge bosons which is made possible by them possessing the characteristics they couple to. It can substantially dictate different aspects of the respective interaction as will be discussed in the following along with the interactions themselves.

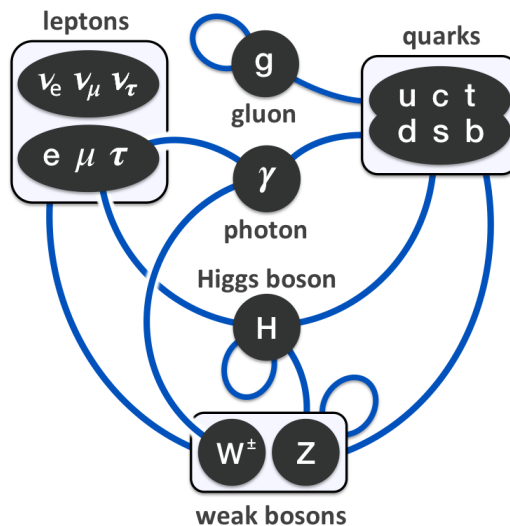


Figure 2.1: Interactions of the Standard Model particles [12].

| Boson          | Symbol   | Interaction | Electric Charge | Colour Charge | Mass [GeV]                                    | Spin |
|----------------|----------|-------------|-----------------|---------------|---|------|
| Photon         | $\gamma$ | el.-mag.    | 0               | —             | $m_\gamma = 0$                                | 1    |
| Gluon          | $g$      | strong      | 0               | $r, b, g$     | $m_g = 0$                                     | 1    |
| $W^\pm$ Bosons | $W^\pm$  | weak        | $\pm 1$         | —             | $m_{W^\pm} \approx 80.379^{+0.012}_{-0.012}$  | 1    |
| $Z^0$ Boson    | $Z^0$    | weak        | 0               | —             | $m_{Z^0} \approx 91.1876^{+0.0021}_{-0.0021}$ | 1    |
| Higgs Boson    | $H$      | Higgs mech. | 0               | —             | $m_H \approx 125.10^{+0.14}_{-0.14}$          | 0    |

Table 2.3: Bosons of the SM [10].

The *electromagnetic force* is mediated by the *photon*  $\gamma$  as its gauge boson which couples only to electrically charged particles. It does so, with an infinite range, in contrast to the other two SM forces. This is suggested by the proportionality of the Yukawa potential  $V_{Yukawa}$  following

$$V_{Yukawa} \propto \frac{e^{-m_{ex}r}}{r}.$$

With  $m_{ex}$  as the mass of the exchanged gauge boson and the photon's mass being  $m_\gamma = 0$ , the only range-limiting factor to the strength of electromagnetic interactions becomes the distance  $r$  between the interacting particles or rather their charges. With that the electromagnetic force between two electrically charged particles is only truly zero in the limit of infinite distances, even if at much shorter distances the force can already be negligible. [11, 8]

The *strong force* is mediated by eight different, twice colour charged but, like the photon, also massless gluons  $g_\alpha$   $\alpha \in \{1, 2, \dots, 8\}$ , which themselves couple to colour charges, implying the before mentioned self-coupling. Because of this self-coupling, amongst other things, photons and gluons behave vastly different, regardless of the  $m = 0$ -commonality. One difference being that the strong force is strength-wise of a far greater magnitude than its electromagnetic counterpart. An around 137-fold strength increase between the two, combined with the self-coupling of gluons and especially the strong force's dependency on the distance between two colour charges, or better, the lack of such a dependency, leads to a rather short interaction range of the strong force.

With this *constant* force in regard to distances in between two arbitrarily far separated colour charges, it quickly becomes energetically favourable for this *strong* bond, or otherwise called *string* or *gluon flux tube*, to break and for a quark-anti-quark pair to materialise. This, yet to be proven, *quantum chromodynamic* effect is called *confinement* and accounts for a *colour-net-neutrality* beyond distances of around  $10^{-15}m - 10^{-14}m$ , closely resembling the diameter of a proton or an atomic nucleus. Therefore the strong force keeps the quarks of protons together. While confined to the proton's diameter the quarks behave more independently the closer they are to the center of the proton due to the strong force becoming weaker. This

effect is called *asymptotic freedom*. Between protons themselves mesons (hadrons as quark-anti-quark bound-states) become a kind of mediator of the strong force as they connect theoretical gluon-quark vertices of different protons to one another. Thereby they cause a much greater attractive force than the electromagnetic repulsion between them due to identical electric charges, hence the interchangeably used name "strong *nuclear force*". [13, 8]

The *weak force* is mediated by three different bosons which couple to particles with non-zero third components of the weak isospin, also called *weak charges*. These mediating particles are the two  $W$  bosons,  $W^+$  and  $W^-$ , as well as the  $Z$  boson, sometimes denoted  $Z^0$ , where the exponents indicate the electric charges. Thus, both  $W$  bosons are able to interact electromagnetically. Additionally, the  $W^+$ ,  $W^-$  and  $Z$  bosons are massive particles unlike photons  $\gamma$  and gluons  $g$ . In fact, they are quite heavy particles allowing for decays in many different ways, further described in the following sections 2.2 and 2.3.

The weak force's eponymous characteristic being the strength-wise *weakest* SM force, again neglecting gravity, is responsible for it to be the only incapable of forming bound states of any sort. However, changing the flavour of a particle, i.e. turning a top quark into a bottom quark, is reserved for weak interactions only. One other feature strongly contrasting from the previously mentioned forces is that the weak force exclusively acts on right-handed common-matter particles and left-handed anti-particles of the SM, since their counterparts do not carry weak charges. First evidence for this *violation of parity*, where the weak force distinguishes between particles of different chirality, was given in the famous *Wu experiment* [14] by Wu et al. in 1957, when all of physics was still expected to be the same for a mirrored world. [15]

As was already stated at the very beginning of this SM chapter, the electromagnetic and the weak force can be described in a unified manner by the *electroweak theory*. Despite appearing very differently on the energy scales common in our universe, once a certain energy level, called unification energy ( $\approx 250$  GeV), is exceeded, those two forces merge into one. This unification was demanded by the renormalizable gauge theory, proposed by Glashow, Salam and Weinberg, solving the problems with the weak force's parity violation and neutral currents. Their electroweak theory, however, required four massless bosons. With the three gauge bosons of the weak force, namely the two  $W$  bosons and the  $Z$  boson, measured to be massive, their theory needs a fourth SM interaction breaking the SM's own symmetry below unification energy in order to be consistent. This symmetry breaking mechanism would allow for massive *weak* gauge bosons of the unified interaction. [16]

This symmetry breaking mechanism is called *Higgs mechanism* giving mass to the *weak* gauge bosons by interaction with the otherwise unseen *Higgs field*. The Higgs field's excitation or gauge boson is the Higgs boson, a *spin-0* particle. This mechanism, postulated by its eponym Peter Higgs in 1964, later turned out to not only give mass to the three weak bosons but also to fermions. The stronger, in terms of strength not *SM-strongly*, a particle couples to the Higgs boson and therefore, the more intensely it interacts with the Higgs field, the more massive a particle is. [16]

### 2.1.2 Limitations and extensions

Despite its success in predicting particles, which were at the time of the theory's development yet to be discovered, and withstanding experimental testing to the highest degree of precision, the Standard Model suffers of a few limitations. As already mentioned, gravity is not within scope of it. Even though gravity's effects on subatomic levels is minuscule, they are not accounted for at all. Furthermore, at the theory's current state there are about 19 free parameters needed in the description of the other three fundamental forces, seen by many as inelegant. Also the SM gives no answer to the unanswered questions of dark matter and dark energy which can not be explained by the current formulation, yet they are believed to make up about 95% of the observable energy of the universe. Additionally, the already mentioned neutrino mass is possibly of a magnitude greater than zero, which is suggested by so called neutrino oscillations between the different flavours. The matter-antimatter asymmetry observed in our universe, as everything on our macroscopic scale is made up of our common matter and not of its anti-counterpart, also makes matters worse for the SM.

Baking these different phenomena, from forces to general questions yet to be answered, into new theories *beyond* the SM is one of the major goals of modern particle physicists and represents its own field. *Supersymmetry (SUSY)*, *loop quantum gravity* and *string theory* are popular examples to only name a few for these beyond SM options. Nevertheless, these come with some problems and limitations themselves. As more in-detail descriptions of the above mentioned extensions of the Standard Model are beyond the scope of this analysis, please refer to [7] for more information.

## 2.2 The top quark

A particle of the SM with properties fundamentally connected to the SM's formulation and its inherent free parameters is the *top* quark. Probably the most striking feature of this third generation up-type quark is its mass. With  $m_{top} = 172.76 \pm 0.30$  GeV it is about as heavy as a gold atom and by far the most massive elementary particle in the SM. After the discovery of the tauon  $\tau^-$  in 1975 [4] and the thereby implied neutrino  $\nu_\tau$ , first observed in 2000 by the DONUT collaboration [17], an imbalance was introduced into the generation count of the now three lepton generations, but only two discovered generation pairs of quarks, namely *up* and *down* quarks, as well as *charm* and *strange* quarks. The instantly triggered hunt for further, heavier quarks quickly confirmed the existence of the *bottom* quark after just two years. This encouraged the search for this now almost certainly missing elementary particle even more. Nevertheless, it would take almost 20 more years until particle accelerators became powerful enough to provide the center-of-mass energy as well as a sufficient amount of data needed for the discovery of the top quark by the DØ collaboration at the Fermilab Tevatron in 1995 [18] due to its great mass.

Since a particle's mass is directly linked to its lifetime  $\tau$ , as can be seen from the relations

below, the resulting  $\tau_{top}$  is very short, in the order of  $10^{-25}s$ . In this extremely short time window the top quark itself can not reach the detector from its origin for direct detection and not even *hadronize*. *Hadronization*, the process of quarks forming colour-neutral particles called *hadrons*, sets in after the *hadronization time* of about  $\tau_{had} \approx 10^{-24}s$  has passed. That is why top quarks do not form any hadrons and can only be reconstructed by detection of their decay particles.

$$\tau_{top} = \frac{1}{\Gamma_{top}} \propto \frac{1}{m_{top}^3} \quad \text{and} \quad 10^{-25}s \approx \tau_{top} < \tau_{had} \approx 10^{-24}s$$

### 2.2.1 Top quark production

Top quarks generally are produced in one of two ways. Either as single top quark or in a top-anti-top quark pair. Even though very recently in early 2020 evidence for four-top-quark-production was published by ATLAS Collaboration [19], the production cross sections for these processes are negligibly small in comparison to the other two and are not further discussed here. The single production as well as the pair production processes, however, are presented in the following sections. Each process is only described from the regular top quark rather than for the top anti-quark as well, since they are identical when all participating particles are exchanged for their corresponding counterpart. [10]

#### Single top quark production

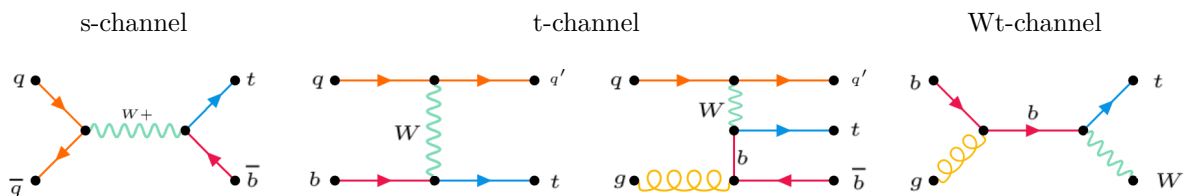


Figure 2.2: Lowest-order Feynman diagrams of single top quark production [15].

The single top production in all cases stems from weak interactions of a bottom quark through an W boson creating a top quark in the process. One differentiates these into three channels based on the "orientation" of the W-b-t-vertex in a given Feynman diagram as well as their on-shell products as depicted in figure 2.2. The *s-channel* describes the creation and subsequent decay of an virtual W boson. Therefore, a pair of one quark and one anti-quark of different kinds but from the same generation, namely one up-type and one down-type, is annihilated forming a W boson, the decay of which creates a top quark and a bottom quark one of which is an anti-quark. For the *t-channel* production a virtual  $W^\pm$  boson is exchanged by an arbitrary up-/down-type quark and a bottom quark, which are then transformed by a *weak* flavour change into their generation partner. Here, the weak interacting bottom quark can either be a virtual particle like the W boson or can be produced on an previous vertex

in another process. The *Wt-channel*, on the other hand, produces an on-shell W boson in association with the top quark via the decay of an bottom quark which was excited before by a gluon.

### Top quark pair production

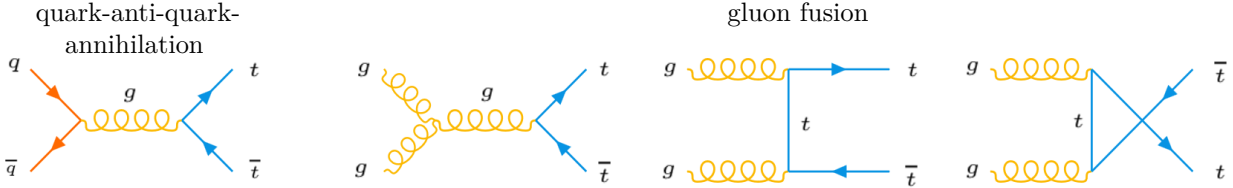


Figure 2.3: Lowest-order Feynman diagrams of top quark pair production [15].

However, in the context of hadron colliders, like in our case the Large Hadron Collider (section 3.2), pair produced top quarks are far more likely. In contrast to the dominantly *weak* single production, these processes rely solely on *strong* interactions, driven by the abundance of high energy gluons and quarks, which protons carry at center-of-mass energies of  $\sqrt{s} = 14$  TeV.

There again are two different ways of pair production one can differentiate between. On the one hand a quark anti-quark pair can create a gluon through annihilation which then, given enough energy, is able to decay in a top anti-top quark pair. This quark driven process though is the by far less likely variant at the Large Hadron Collider. In about 90% of the cases top quark pairs originate from *strong* self-interaction of gluons resulting in a top anti-top on-shell pair. To assign numbers to these processes, the particle data group cites in its 2020 review of particle physics [10] a production cross section of

$$\sigma_{t\bar{t}}^{NNLO+NNLL(@\sqrt{s}=14TeV)} = 984.5^{+23.2+41.3}_{-34.7-41.3} pb .$$

### 2.2.2 Top quark decay

As mentioned in section 2.2, top quarks decay rather quickly after they come into existence. In our current understanding they exclusively do so via an on-shell-combination of a W boson and a *down-type* quark. Since generation changes of quarks through weak interaction are heavily suppressed in comparison to changing flavour inside a generation, this *down-type* quark is almost always a bottom quark (99.18%). To fully classify the top quark's decay one takes the decay of the W boson into account as well. The W boson does decay in one third of the cases into leptons (33%), a charged lepton with its neutral neutrino generation partner, and otherwise into two quarks (67%), which gives a few different final state options for the top quark decays.

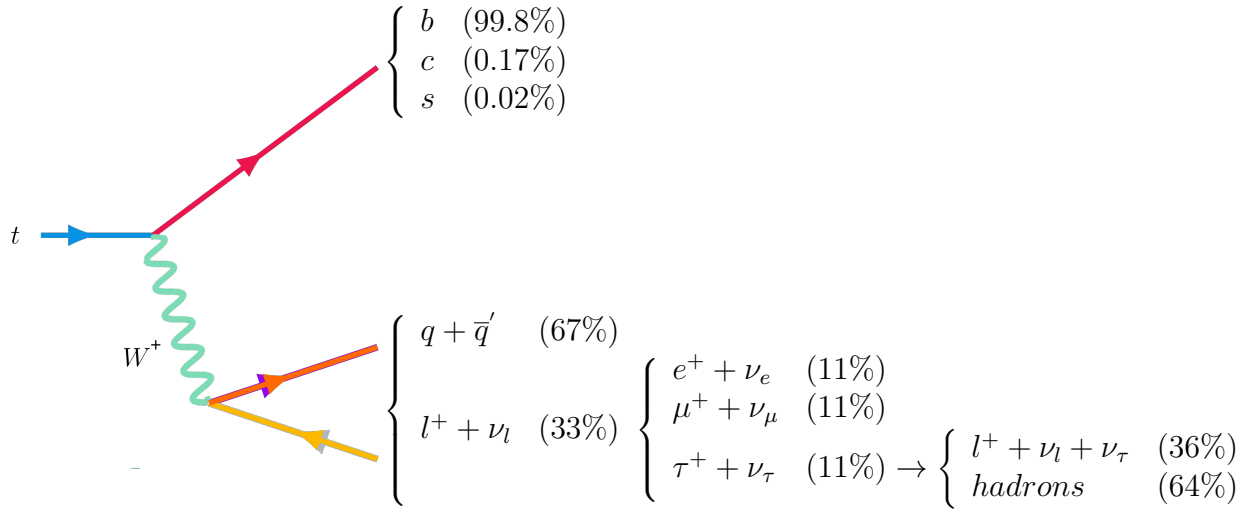


Figure 2.4: Decay channels of a top quark.

Combining these possible decay processes of a single top quark for a top-anti-top quark pair leaves us with three different classes of  $t\bar{t}$  final states called *fully-hadronic*, *semi-leptonic* and *di-leptonic* (figure 2.5), named after their most likely detectable final state after *hadronization* according to the leptons (section 4.1). These following branching ratios are expected in this regard:

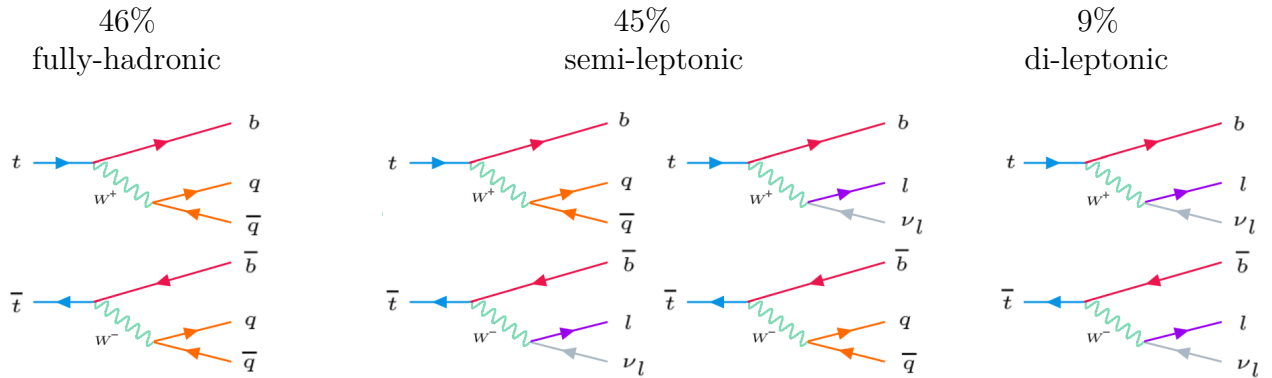


Figure 2.5: Branching ratios and first order Feynman diagrams of  $t\bar{t}$  decay channels [15].

The *fully-hadronic* channel is with about 46% the most likely case. With no undetectable neutrinos in the final state, given that both W bosons decay hadronically, it is the only channel perfectly suited for a complete kinematic reconstruction, given there are no other

neutrino producing secondary interaction vertices simultaneously. Nevertheless, this channel is bound to produce a lot of jets bringing its own disadvantages with it including difficult jet separation as well as background rejection.

The other two channels produce charged leptons in conjunction with neutrinos. According to the *lepton universality*, which states that the gauge bosons' coupling strength to any lepton is flavour independent, the branching ratios of the different lepton generations have to be equal. While electrons are stable and muons are stable enough, taus generally decay inside the detector as indicated in figure 2.4. As this becomes important for the analysis later, chapter 5 will discuss it in more detail. For now we note that this shifts the branching ratios towards final states with more hadrons and less leptons, which was already accounted for in the percentages listed above.

The *semi-leptonic* channel is almost equally likely to occur as the *fully-hadronic* channel since it includes final states reached by the most decay channel combinations and is therefore affected the most by combinatoric effects. Even though one neutrino is created maximally for one W boson decaying hadronically while the other does so via an electron or a muon and the according neutrino its energy and direction can be determined very accurately via the *missing transverse energy*  $E_T^{miss}$ , described in section 3.3.3.

The *di-leptonic* channel is the rarest one of the three with potentially the most neutrinos. Yet, as there are very few quarks and especially no light ones, the background contamination is fairly low, making final states in the *di-leptonic* channel very clean.

## 2.3 The Z boson

The second particle to which further information is needed is the Z boson as this analysis covers  $t\bar{t}Z$  events. The first to suggest the existence of such an electrically neutral weak gauge boson were Glashow, Weinberg and Salam in their electroweak theory, from 1967 (section 2.1.1). Not long thereafter the *Gargamelle* experiment at CERN provided evidence of the Z boson's existence through the observation of elastic neutrino scattering, paving the Standard Model's way in 1973 [20]. The direct measurement of the Z boson came ten years later with for the first time sufficient center-of-mass energy from proton-anti-proton collisions in the *Super Proton Synchrotron* as well at CERN in 1983 [21, 22].

*Weak* interactions mediated by the Z boson, also called *neutral weak currents*, do not change any of the charges nor the flavour of the participating particles when scattered according to today's knowledge of the process. This process amongst others shall be further introduced while describing the production as well as the decay of Z bosons in the following two subsections.

### 2.3.1 Z boson production

Generally there are two main mechanisms Z bosons take part in as the carrier of the weak force. For one there is the already mentioned neutral current scattering. The second would

be the annihilation of particles and their anti-particles.

Starting with the first case, we want to look at the scattering of neutrinos  $\nu$  (or anti-neutrinos  $\bar{\nu}$ ), especially of muon-neutrinos  $\nu_\mu$  (or  $\bar{\nu}_\mu$ ), on electrons as this process, displayed in figure 2.6, played a key role in the  $Z$ 's observation and with that in its establishment in the SM. Shooting a muon-neutrino-anti-neutrino-beam on electrons inside atomic shells, the processes

$$\nu_\mu + e^- \longrightarrow \nu_\mu + e^- \quad \text{or} \quad \bar{\nu}_\mu + e^- \longrightarrow \bar{\nu}_\mu + e^-$$

are induced and traceable by subsequent measurements of the electrons' final states. The only gauge boson able to mediate this scattering is the  $Z$  boson, making the above stated scattering a very important process in  $Z$  boson research.

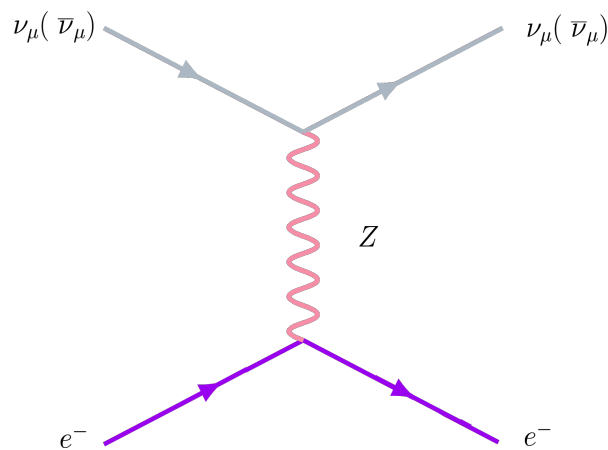


Figure 2.6: moun-(anti-)neutrino electron scattering.

For the annihilation based  $Z$  boson production process there are mainly two scenarios, the annihilation of two charged leptons or of two quarks. Here, the latter one, also called *Drell-Yan process*, is by far the most common  $Z$  boson production path in the **L**arge **H**adron **C**ollider. In contrast to the  $\nu_\mu$ - $e$ -scattering though, both of the participating particle pairs carry electric charge and their interaction can therefore also be mediated electromagnetically by the photon  $\gamma$  as depicted in figure 2.7.

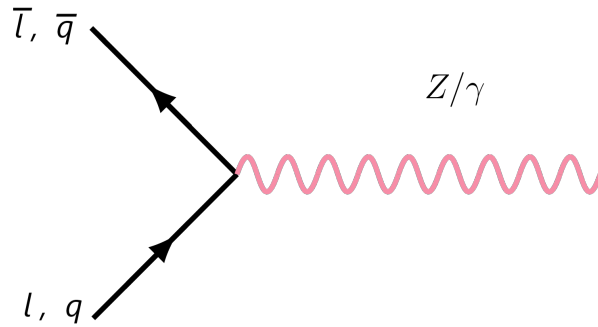


Figure 2.7: Z boson production through annihilation of particle-anti-particle pairs of leptons or quarks.

Looking at the scattering example one can see, that if a quark carries enough energy a Z boson can simply be emitted without changing any quantum number or charge of the quark but only its momentum in the process, like depicted in figure 2.8. Since the top quarks are created very close to the primary collision vertex they tend to have sufficient energy to do so.

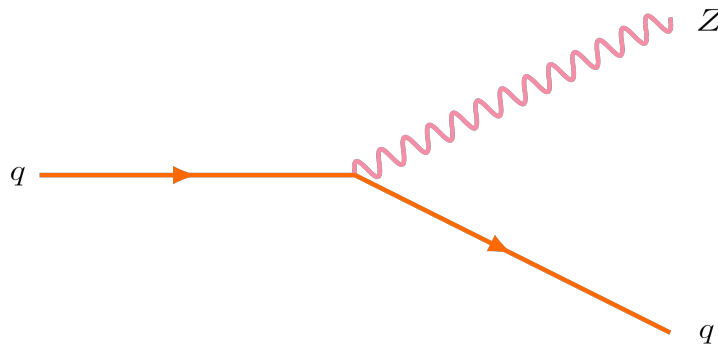


Figure 2.8: Emission of Z boson by a sufficiently energetic quark.

Another production path for Z bosons is the, at least since 2012 widely known, decay of the Higgs boson into two Z bosons one of which is in an excited state. As illustrated in figure 2.9, in the specific case for the Higgs observation both Z bosons decay leptonically, giving a good sensitivity over a wide mass range for the Higgs measurement. This ultimately led to its confirmed detection by the ATLAS Collaboration, as well as the CMS Collaboration [2, 3], also depicting the preferred spin and parity of the Higgs boson to be  $J^P = 0^+$  as predicted by theory. For this matter a deep understanding of the Z boson's decay and with that its reconstruction becomes a key point in research of Higgs physics. [23]

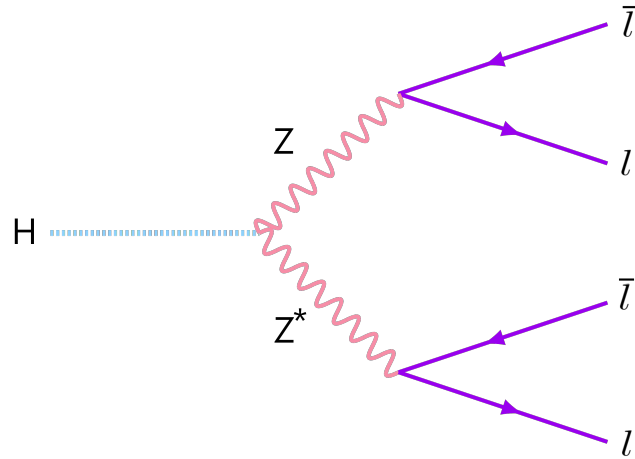


Figure 2.9: Higgs boson decay into two Z bosons leading to a four lepton final state.

### 2.3.2 Z boson decay

As already shown in the example of the annihilation production processes in figure 2.7 above, the Z boson is able to decay into all fermions in association of their anti-fermion, except for the too massive top-anti-top quark pair (2.2). This incorporates quarks as well as leptons, charged and neutral. By far the most common decay channel of the Z boson is into a quark-anti-quark pair with a branching ratio of around 70% followed by production of an undetectable neutrino pair in 20% of the decays, which therefore is also called *invisible* decay. Charged leptons, being produced in only 10% of the cases, can be detected and therefore reconstructed the easiest, relatively speaking. This makes their decay channel the most attractive one for this analysis, which is discussed in more detail in the corresponding section 5.2.

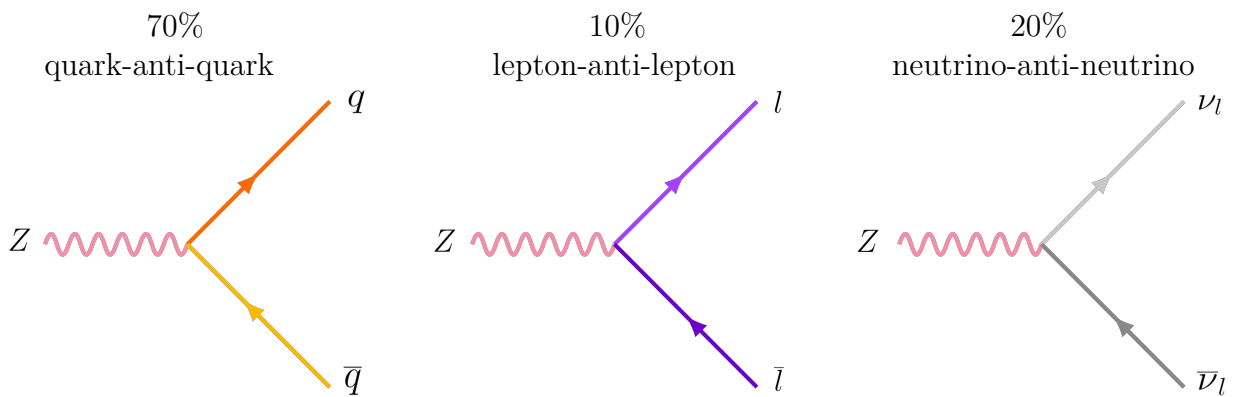


Figure 2.10: Z boson decay channels with respective branching ratios.

## 2.4 $t\bar{t}Z$ events

The associated production of  $t\bar{t}$ -pairs and a Z boson is an important background in not only  $t\bar{t}H$  events and Higgs research in general as stated in the previous section but also in searches for evidence of SUSY and other exotic processes. For the Standard Model itself the coupling of Z bosons and top quarks is of interest as well, since they are two of the heaviest particles and not yet very well constrained through experimental measurements. [24]

### 2.4.1 $t\bar{t}Z$ production

The production of  $t\bar{t}Z$  events in hadron colliders mainly takes place at lowest-order via the production channels depicted in figure 2.11, where for each path the Z boson is emitted by a quark. The differences between the channels are given by the stages of the decay's path at which the Z boson is radiated off. Either a quark from processes before the top quark pair is created, e.g. a sea-quark of the colliding protons emit the Z boson, or one of the top quarks does so itself. From this, according to [25], the production cross section of  $t\bar{t}Z$  events was measured to be

$$\sigma_{t\bar{t}Z}^{NNLO+NNLL(@\sqrt{s}=14TeV)} = 811_{-9.6\%}^{+11.0\%+2.4\%} fb .$$

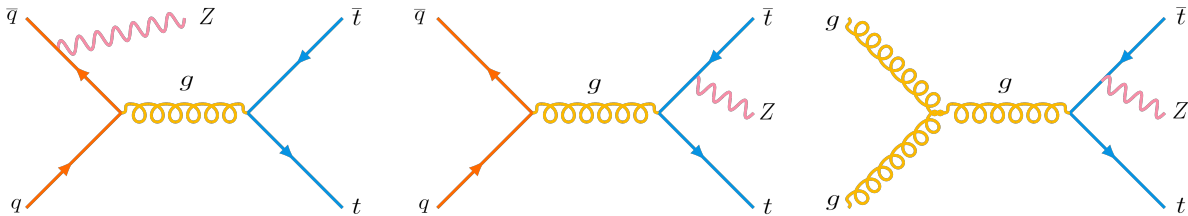


Figure 2.11: Main production channels for  $t\bar{t}Z$  events in hadron colliders.

Comparing this cross section to the one of solely a top quark pair by calculating the quotient of the two, one observes a factor of about 1200.

$$\frac{\sigma_{t\bar{t}}^{NNLO+NNLL(@\sqrt{s}=14TeV)}}{\sigma_{t\bar{t}Z}^{NNLO+NNLL(@\sqrt{s}=14TeV)}} \approx 1200$$

This means the simultaneous production of a top quark, an anti-top quark, and a Z boson is heavily suppressed in comparison to the  $t\bar{t}$  production. The main reason for this is the much smaller electroweak coupling of colour charged quarks in contrast to their preferred strong coupling via gluon interactions thus making the emittance of a Z boson by a quark relatively unlikely. [24]

### 2.4.2 $t\bar{t}Z$ decay

Given the decay channels from sections 2.2 and 2.3 of the top quark and the  $Z$  boson, respectively, figure 5.4 summarizes the probabilities of different decays of events of their associated production. Combining these multiplicatively gives the probability of the corresponding  $t\bar{t}Z$  decay path and points to the different final states. Here taus  $\tau$  are listed separately from electrons  $e$  and muons  $\mu$  because of their unstable nature, decaying either hadronically or leptonically further motivated and discussed in the event selection subsection 5.2.2. Yet, for this reason, from here on the abbreviation "l" for leptons only includes electrons  $e$  and muons  $\mu$  if not explicitly stated otherwise.

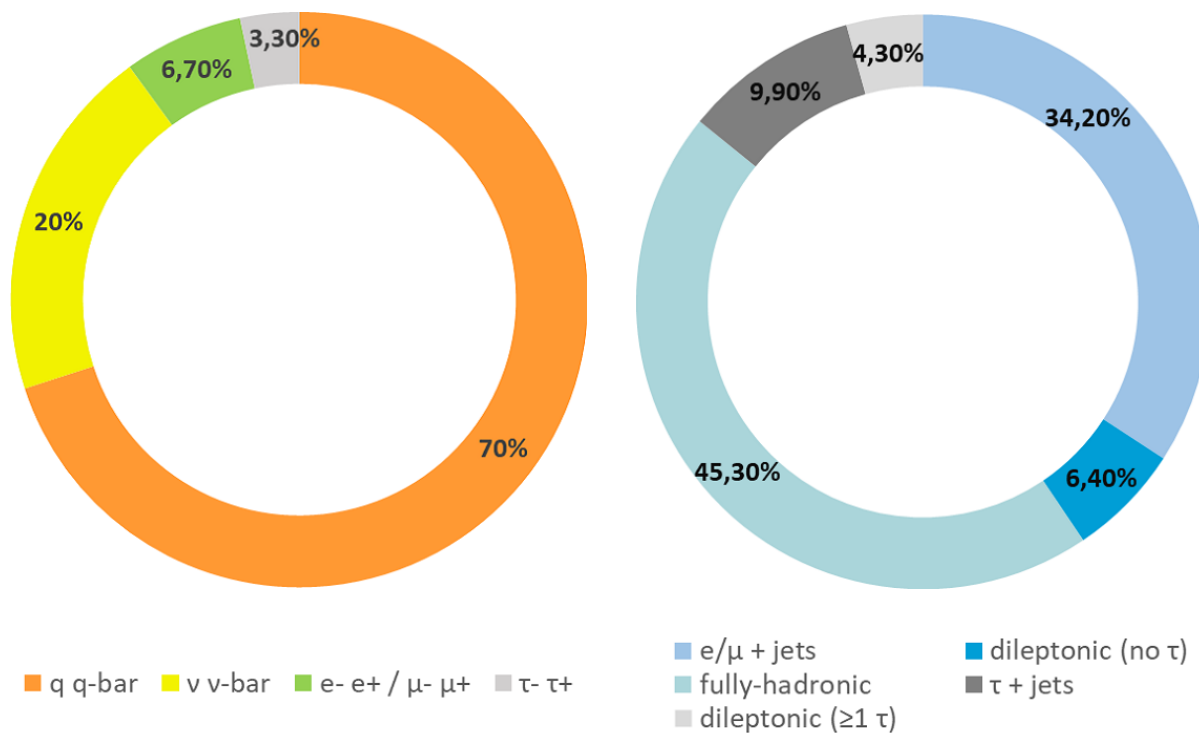


Figure 2.12: Total branching ratio of the decay of  $t\bar{t}Z$  events.



# 3 | Experimental setup

## 3.1 CERN

The acronym CERN today describes the European organization for nuclear research stemming from its founding council's name "*Conseil européen pour la recherche nucléaire*". Founded 1954 in Geneva, Switzerland, right at the French boarder, by twelve mainly European countries, it has grown into the largest particle physics laboratory worldwide with now in total 23 member states. Between the various particle accelerators and experiments, as seen in figure 3.1, some of the biggest leaps and discoveries in particle physics of the past half century have been accomplished on CERN's premiss.

This chapter focuses on the arguably most famous accelerator of CERN, the Large Hadron Collider, and the ATLAS experiment as one of the detectors connected to it as this analysis is modelled to contribute to this specific collaboration. [15, 24, 26]

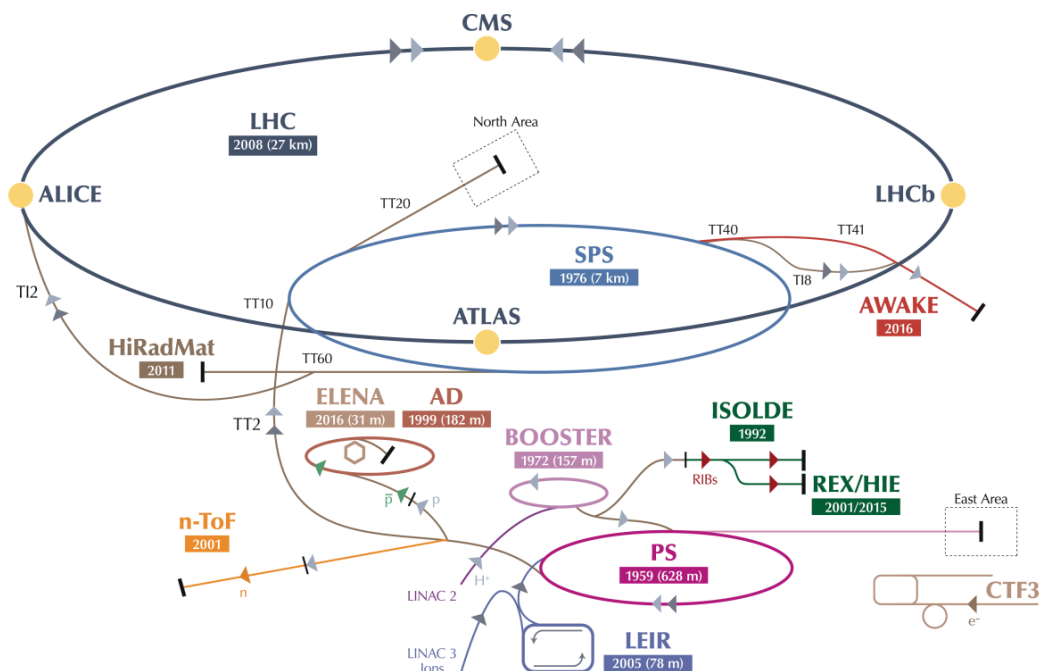


Figure 3.1: CERN Accelerator Complex [27].

## 3.2 The Large Hadron Collider

The **L**arge **H**adron **C**ollider or *LHC* is the largest as well as the most powerful accelerator of not only CERN but worldwide. With its circumference of 27 km it reached a center-of-mass energy  $\sqrt{s}$  of 14 TeV in proton-proton collisions in its most recent *Run-2* phase from 2016 to 2018. Currently shut down, the LHC as well as its four experiments are being upgraded for the next data collection phase, *Run-3*, scheduled for 2021 until 2023.

To reach its peak center-of-mass energy of about  $10^{14}$  proton bunches are accelerated close to the speed of light 100m under the earth's surface in two beam pipes in either direction around the accelerator loop. These then are crossed inside the detectors of the four experiments around the LHC; *ALICE*, *ATLAS*, *CMS* and *LHCb*. To accomplish all of these collision parameters, many different high performance components of the LHC have to function in perfect harmony making its start-up a challenging process taking around a quarter year. The beam pipes need to be brought to an ultra high vacuum to reduce drag, while the magnet system for keeping the protons on track must be cooled down to almost absolute zero and kept perfectly calibrated. These amongst many other tasks secure controlled data acquisition at the different experiment sites. One of those is the already mentioned ATLAS experiment which shall be described in the next section as it is the parent experiment of this analysis. [15, 26]

## 3.3 The ATLAS experiment

The *ATLAS* detector, **A** **T**oroidal **L**H**C** **A**pparatu**S** depicted in figure 3.2, is with a length of 44 m, a 25 m diameter and 7000 tons of weight the biggest particle detector worldwide. It is build to suit almost all purposes in particle physics making it especially helpful in the reconstruction of whole events meaning the collection of data on every kinematic aspect of a collision. Therefore the work done by the ATLAS Collaboration includes precise measurements of all kinds of Standard Model parameters as well as searches of physics beyond the Standard Model. [15]

### 3.3.1 Detector sub-systems

Different sections and parts of the detector are responsible for detecting specific signatures, properties or characteristics of particles. To give a quick overview on the make up of the ATLAS detector the following sections focus on the main groups of devices for studying  $t\bar{t}Z$  events. For detailed descriptions of the functionality and the performance of the individual parts of the ATLAS detector it is referred to [28] and [29].

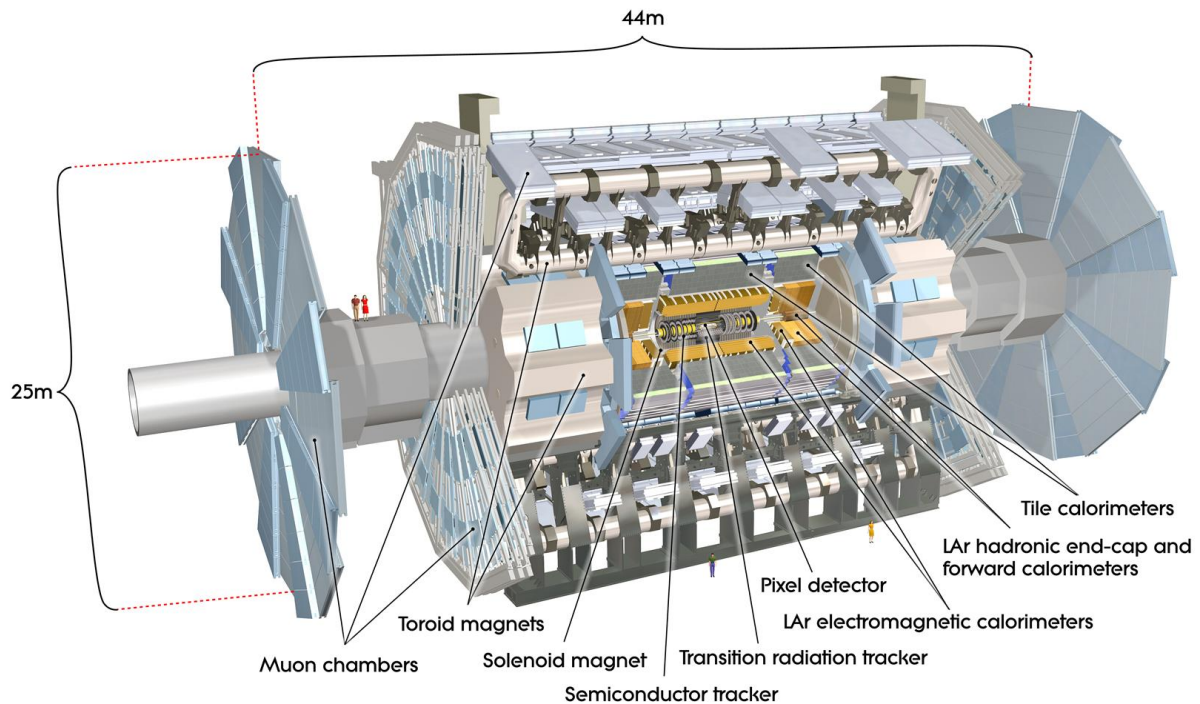


Figure 3.2: The ATLAS Detector [30].

### Magnet system

The basis for the tracking of all electrically charged particles sets the ATLAS detector's *magnet system*. It is made up of three large superconductive magnets, the central solenoid magnet, the barrel toroid and an end-cap toroid, and provides strong homogeneous and calibrated magnetic fields inside the detector volume for different detector sub-systems. This allows for calculations of the electric charge and the momentum of particles based on the Lorentz force formulated as

$$\vec{F}_{Lorentz} = q \cdot (\vec{v} \times \vec{B})$$

since the angular deflection of a particle's path is proportional to its electric charge's sign and magnitude as well as the mentioned momentum. Therefore, the trajectory of each particle has to be tracked in order to reconstruct the individual deflections and with that the other particle parameters. This is mainly done by the *inner detector*. [24]

### Inner detector

The inner detector (ID) is, as the name suggests, the closest detector system to the beam pipe and therefore to the primary vertices (section 5.1). It itself consists of three subsystems briefly presented in the following.

The most inner subsystem consists of an array of pixel detectors especially built for high radiation resistance. In preparation of LHC Run-2's high luminosity and even higher radiation

the *Insertable B-Layer* (IBL) system was added [31]. Now the whole subsystem provides a spacial resolution of  $10\mu\text{m}$  in  $r$ - $\Phi$ -direction and  $115\mu\text{m}$  in  $r$ - $z$ -direction [32].

The second ID subsystem is the *silicon strip tracker* (SCT), providing another layer of trajectory tracking on a slightly larger scale with a spacial resolution of 17 and  $580\mu\text{m}$  in  $r$ - $\Phi$ - and  $r$ - $z$ -direction, respectively.

For additional tracking on the outer most ID layer in an even bigger volume the *transition radiation tracker* (TRT [33]) is installed. Consisting of drift tubes filled with an mixture of 70%  $Xe$ , 27%  $CO_2$ , and 3%  $O_2$  the TRT resolves radiated off photons  $\gamma$ . Therefore, it is mainly providing further information on trajectories of electrons. [34]

## Calorimeters

To measure the energy of the particles tracked by the ID, two different calorimeters are put in place at the ATLAS detector. These are located around the tracking systems since the measurement of a particle's energy includes absorbing the particle. Depending on the particle type, this happens either in the *electromagnetic calorimeter* or in the *hadronic calorimeter* which both use the same principle. With alternating *absorbing* and *active* layers, the particles interact with the absorbing one depositing energy and creating a subsequent particle shower which is then recorded in its shape and with its intensity by the active layer.

The electromagnetic calorimeter (LArC) uses liquid argon (active) and lead plates (absorbing) to detected electromagnetically interacting particles, mainly electrons and photons, as the calorimeter's name suggests. The hadronic calorimeter (TileCal) for energy measurements of hadrons utilizes a combination of scintillating tiles (active) and iron plates (absorbing). Together with their corresponding end cap implementations they provide energy measurements in regions of absolute values pseudorapidities up to  $|\eta| < 4.9$ . [34, 35]

## Muon spectrometer

Muons do only minimally ionize the materials of the active layers in the before mentioned calorimeters as well as in the inner detector. For that reason the *muon spectrometer* provides additional measurements of their tracks and trigger information in areas with  $|\eta| < 2.7$ . It is equipped with muon-specific *Monitored Drift Tubes* (MDT) for tracking, *Cathode Strip Chambers* (CSC) for the calorimetry part and *Resistive Plate Chambers* (RPC) as well as *Thin Gap Chambers* (TGC) for event triggering. With that a spacial resolution of  $35\mu\text{m}$  in the  $r$ - $\Phi$ -direction is reached for muons. [34]

### 3.3.2 Trigger and data acquisition

As briefly mentioned in the subsection 3.3.1 before, the data taking has to be *triggered* by event specific properties recorded by a variety of the detector's subsystems at almost the exact same time. The reason for that lies in the huge design luminosity of  $\mathcal{L} = 10^{34}\text{cm}^{-2}\text{s}^{-1}$  of the LHC causing 40 million bunch crossings every second (40 MHz) with again multiple

collisions each adding up to about 1 GHz of events. The limit for writing those to memory being 200 Hz makes a pre-selection necessary, picking only events most interesting to research for subsequent storage while discarding the rest.

This pre-selection is managed on three different *trigger levels*, namely level-1, level-2 and an event filter, whereas the latter two were recently combined to form the high level trigger system *HLT*. This upgrade is in place since the LHC's "Long Shutdown 1" (LS1) to increase communication between the two and with that speeding up the selection process. The level-1 system bases decisions on hardware readouts of the different ATLAS subsystems (1 GHz  $\rightarrow$  75 kHz) while the HLT uses software to determine its decisions (75 kHz  $\rightarrow$  2 kHz  $\rightarrow$  200 Hz) reaching the threshold for data collection speeds. [15, 24, 36]

### 3.3.3 Coordinate system

In order to describe any position or trajectory of any event's particles inside the ATLAS detector a universal coordinate system was put in place. It is centred around the beam axis as the z-axis while the positive direction of the x-axis points towards the LHC's center and the positive y-direction points up, all together being orthogonal to one another. In addition to this cartesian coordinate system features of a cylindrical system are incorporated as well. On the one hand the azimuthal angle  $\Phi$  describes the orientation inside the x-y-plane around the z-axis and is defined in a range of  $\Phi \in [0, 2\pi]$ . The polar angle  $\theta$ , on the other hand, reflects the angular distance between the beam or z-axis and a given trajectory or vector.

$$\Phi = \arctan\left(\frac{p_y}{p_x}\right) \quad \text{and} \quad \theta = \arccos\left(\frac{\sqrt{p_x^2 + p_y^2}}{p_z}\right) = \arccos\left(\frac{p_T}{p_z}\right)$$

Besides those basic measures a couple of auxiliary variables have been established to more easily describe every possible event which will be briefly defined in the following. [37]

#### Pseudorapidity $\eta$

The pseudorapidity  $\eta$  presents an alternative for the not Lorentz invariant polar angle  $\theta$  inasmuch as that it projects angles from  $\theta = 0^\circ$  to  $\theta = 180^\circ$  onto  $\mathbb{R}_0$  where  $\eta = 0$  corresponds to a trajectory  $\theta = 90^\circ$  or orthogonal to the beam axis and  $\eta = +\infty$  and  $\eta = -\infty$  to  $\theta = 0^\circ$  and  $\theta = 180^\circ$ , respectively. The specific relationship between  $\eta$  and  $\theta$  is

$$\eta = -\ln\left[\tan\left(\frac{\theta}{2}\right)\right].$$

The pseudorapidity  $\eta$  equals the rapidity  $y$  in the limit of highly relativistic particles, which itself is otherwise hard to measure in hadron colliders where the rest frame of the detector rarely coincides with the center-of-mass frame of the colliding protons.

$$\eta \stackrel{rel. particle}{\simeq} y = \frac{1}{2} \ln\left(\frac{E - p_z}{E + p_z}\right) \quad [38]$$

### Distance variable $\Delta R$

The distance variable  $\Delta R$  enables us to calculate the separation of two objects inside the detector volume, thus close the trajectories are to each other. It describes a cone centred around one of the two objects on the base circumference of which the trajectory of the other particle ends. To calculate  $\Delta R$  the differences of the particle trajectories in both the azimuthal angle  $\Phi$  and the pseudorapidity  $\eta$  have to be known, forming the relation

$$\Delta R = \sqrt{(\Delta\eta)^2 + (\Delta\phi)^2} .$$

### Transverse momentum $p_T$

While momentum parallel to the direction of the beam axis is a remnant of the accelerators center-of-mass energy  $\sqrt{s}$ , orthogonal or transversal momentum parts with respect to the beam axis are solely due to hard scattering processes and give insight into the primary collision. The transverse momentum  $p_T$  of a particle therefore describes the momentum transferred through the collision from z-direction into the x-y-plane.

$$p_T = \sqrt{p_x^2 + p_y^2}$$

While considering relativistic particles the transverse momentum  $p_T$  is equivalent to a particles transverse energy  $E_T$ . But when the particles are getting more massive this does not hold any longer and instead follows

$$E_T = \sqrt{m^2 + p_T^2} .$$

### Missing transverse energy $E_T^{miss}$

If one considers transverse momentum or energy in the context of momentum and energy conservation all transverse momenta have to cancel out since before the collision both  $p_x$  and  $p_y$  of the whole system are zero. This constraint on the final state of all produced particles can be formulated as

$$\vec{p}_{T,tot} = \sum_i^{N_{tot}} (p_{x,i}, p_{y,i}) \stackrel{!}{=} \vec{0} .$$

Here it was summed over the total amount of all produced particles  $N_{tot}$ . However not every particle is or can be detected splitting  $N_{tot}$  into the detector *visible* and *invisible* particles

$$N_{tot} = N_{vis} + N_{invis} .$$

Therefore,

$$-\sum_i^{N_{vis}} (p_{x,i}, p_{y,i}) = \sum_j^{N_{invis}} (p_{x,j}, p_{y,j}) = \vec{p}_{T,miss}$$

describes the measurable combined transverse momentum of all invisible particles. Calculating the absolute value of  $\vec{p}_{T,miss}$  then gives the commonly used *missing transverse energy*  $E_T^{miss}$  to characterize events corresponding to the momenta of their invisible particles, which are neutrinos in most cases.

**Mean decay length  $L_{xy}$** 

The mean decay length  $L_{xy}$  results from the projection of the distance travelled by a particle from their primary vertex to the position of their decay onto the x-y-plane.  $L_{xy}$  is defined via

$$L_{xy} = \beta\gamma\tau \quad \text{with} \quad \beta = \frac{v}{c} \quad \text{and} \quad \gamma = \frac{1}{\sqrt{1-\beta^2}}$$

with  $\beta$  as the ratio between the particles velocity  $v$  and the speed of light  $c$ , the Lorentz factor  $\gamma$  and the particle's lifetime  $\tau$ . [39]

**Impact parameter  $d_0$** 

The impact parameter  $d_0$  portrays a projection of a particle's trajectory onto the x-y-plane beginning at the primary vertex and ending at the detection position. [39]



## 4 | Monte Carlo data simulation

In the field of high energy physics simulated particle-collision-data is crucial to be able to compare the theoretical predictions of a theory with the collected data from the detectors. In the presented case proton-proton collisions are simulated along with the environment of the ATLAS detector to obtain detailed information on the simulated final state with which for example signatures of specific events can be checked. Any agreement or deviation between both outcomes, simulated and experimentally measured, then suggests compatible or deviating theory aspects, respectively. In this chapter this simulation process is described in addition to more detailed information on the specific data set used.

### 4.1 Monte Carlo generation

Most simulations in particle physics use Monte Carlo methods to generate a huge amount of data to model the theoretically expected distributions in and of particle collisions inside the accelerator environment. Monte Carlo methods use pseudo-random numbers to model the different particle interactions according to the corresponding theory and lead to a detailed kinematic description of the final state given a certain initial state. These simulations not only include the initial hard processes between the colliding hadrons and their constituents themselves and then jump straight to the final state, but also cover the resulting parton showers, their hadronization and the subsequent decay paths of any hadron or other unstable particle involved in the event. Each of these steps is depicted in figure 4.1 and is discussed briefly in the following.

In the already mentioned hard process colliding protons at the energy level of the LHC are considered as composite particles,  $A$  and  $B$ , made up from smaller partons e.g.  $a$  and  $b$  according to the parton model [40]. Interactions of individual partons lead to the production of further particles  $c$  the production cross section of which is described by  $d\sigma_{a+b\rightarrow c}$ . If one considers the hadronic cross section in conjunction with the production of other collision remnants  $X$  the cross section combines to

$$d\sigma_{A+B\rightarrow c+X} = \sum_{a,b} \int_0^1 dx_a \int_0^1 dx_b f_A^a(x_a, Q^2) f_B^b(x_b, Q^2) d\sigma_{a+b\rightarrow c}$$

summing over all contributing Feynman diagrams. In this context  $f_Y^y(x_y, Q^2)$  is a parton

distribution function (PDF) describing the probability of a parton  $y$  with momentum fraction  $x_y$  within the parent proton  $Y$  at energy scale  $Q$ . These distributions must be measured and cannot be calculated from deep inelastic scattering. [36]

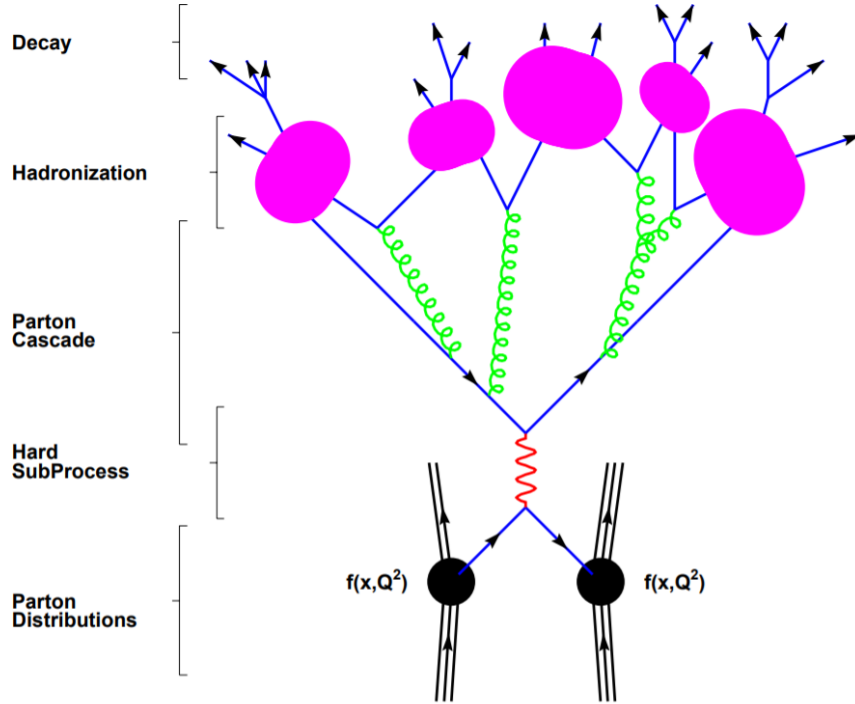


Figure 4.1: Simulation process of a proton-proton collision [41].

The resulting partons still carry colour charge allowing for the emission of gluons prior to the formation of color neutral hadrons, which is demanded by the strong force, described in section 2.1.1. These gluons lead to the creation of even more color charged particles as a consequence of their decay and, hence, are responsible for a cascade of partons.

Below a certain energy threshold this stops initializing the formation of hadrons in a process called *hadronization*. Since many of these hadrons are not stable enough to propagate through the whole detector, they decay to sufficiently stable color neutral particles producing the final state that can be measured in a detector or a simulation of one as in our case. [36]

## 4.2 Monte Carlo generators

Programs producing events using Monte Carlo methods are called *generators*. For different stages of the event generation process special generators are used. The ones responsible for producing the samples used in this analysis, listed in table 4.1, are presented in this section while their key features and purposes are briefly explained. For further information on each of these fall back on the provided references.

### aMC@NLO

For the initial hard scattering process and therefore the generation of the  $t\bar{t}Z$  events *MadGraph5's* aMC@NLO event generation tool [42] was used to generate them at *next-to-leading order*. In addition to that the MEN3ONLO parton distribution function set (PDF set) was used.

### Pythia

Currently in its eighths version second iteration Pythia 8.2 [43] is a general purpose event generator and is used for producing the parton showers after the hard scattering in our samples. This is done so with a A14N23LO tuning [44].

### EvtGen

The EvtGen generator [45] is used for especially heavy flavour decays in our samples, like for example the decays including top and bottom quarks.

## 4.3 Monte Carlo samples

While produced in the before described manner there are two levels of information kept in the process, *detector-level data* and *truth-level data*, which are also included in the used samples in this analysis listed in table 4.1. Each of these levels contains basic information on the events in general alongside with more specific data on the identified objects.

The latter object-specific data most importantly contains the *momentum four-vector*, also known as *Lorentz vector*, for each physics object, particle or jet, as well as the particle type and their electrical charge. Additionally, it includes information on the quality and isolation of a particle's detection for selections based on working points of selection efficiencies explained in [46]. For any object  $X$  the corresponding four dimensional momentum four-vector  $P_X$  is defined as

$$P_X = \begin{pmatrix} p_x \\ p_y \\ p_z \\ E \text{ or } m \end{pmatrix}_X \quad \text{or} \quad P_X = \begin{pmatrix} p_T \\ \eta \\ \Phi \\ E \text{ or } m \end{pmatrix}_X$$

depending on the used variables and convention. The two representations are equivalent and contain the same amount of information.

Meanwhile, the more general event information includes the run- and event-numbers necessary for keeping track of the alignment of both data sets, the amount of detected jets, as well as b-jets, the four-vector of the missing transverse energy  $P_{E_T^{miss}}$  and various different weights for the event itself based on specific generator characteristics or the event's decay branching ratios and therefore the event's overall likelihood.

Where and when, in the sense of the point in time and stage in decay paths the truth- and detector-levels are located, is explained in the next subsections.

| Z boson decay                 | campaign | sample   |
|-------------------------------|----------|--|
| $Z \rightarrow e^+ e^-$       | e/2018   | 410218.aMcAtNloPythia8EvtGen_MEN30NLO_A14N23LO__ttee.e5070_s3126_r10724_p3629.root     |
| $Z \rightarrow \mu^+ \mu^-$   | e/2018   | 410219.aMcAtNloPythia8EvtGen_MEN30NLO_A14N23LO__ttmumu.e5070_s3126_r10724_p3629.root   |
| $Z \rightarrow \tau^+ \tau^-$ | e/2018   | 410220.aMcAtNloPythia8EvtGen_MEN30NLO_A14N23LO__tttautau.e5070_s3126_r10724_p3629.root |

Table 4.1: List of used Monte Carlo samples.

To the production of these samples; they stem from the Monte Carlo production campaign corresponding to the 2018 data taking period and were produced *inclusively*. This latter point allows for the Z bosons' decay particles, especially leptons, to emit highly energetic photons  $\gamma$  by e.g. *Bremsstrahlung*, otherwise known as braking radiation, amongst other things. This process becomes important in section 6.4.4 later in this analysis as these photons  $\gamma$  are also detected in a similar fashion to charged leptons.

### 4.3.1 Detector-level data

*Detector-level data* displays events and their respective particles, as they can be detected in real world detectors only in the final state configuration. This includes not only all stable and semi-stable or "stable-enough" particles created on the decay paths of the primary vertex' particles, like leptons and already clustered hadrons in the form of jets, according to the description in section 5.1, but also those which arise from interactions of particles of any stage of the decay path with detector material or among one another.

When all these objects are defined, information on them, as described above in section 4.3, is saved looking like ordinarily collected data samples from an actual detector with momentum four-vector corresponding to the jets made out of hadrons and leptons of an event as well as charge and flavour information on them.

### 4.3.2 Truth-level data

*Truth-level data* contains information on the events and processes as they were generated using the different generators listed in 4.2. Regarding figure 4.1 this includes all information on the decay paths and the resulting decay particles up to the hadronization and again from there on to the final state, since the hadronization process cannot be easily described, as it is still not fully understood. Therefore, truth-level data includes the hard scattering process, the subsequent decays of the primary vertex particles, as well as them decaying further or emitting gluons, which again decay themselves. In addition to that, the decay processes of the hadrons resulting from hadronization is included in the information. In a sense this data level represents the work of an ideal detector collecting information on every sub-process of proton-proton collisions with perfect precision. Since this is not possible in the real world and our detectors only get to "see" the smeared detector-level data with its imperfections in the resulting detections, there can be major differences in the final state of the same event on the two different data levels, which are addressed in the following section.

### 4.3.3 Final state differences

Generally speaking, differences between the final states of truth- and detector-level data are, as described before, expected and the reason for the non-trivial nature of high energy physics research. Here the need for sophisticated reconstruction methods arises in order to gain insights into the fundamental processes taking place from right after the collisions with the "contaminated" data collected by our detectors.

Through a variety of phenomena these differences can not only include deviations of the counts of jets and high energy, close to the primary vertex, quarks, usually producing the former jets, but also, more importantly, changes in the number and flavour of leptons, which otherwise should be stable or semi-stable, in the electron's and the muon's case, respectively. As will be discussed in more detail in section 6.5, the results of this analysis are split into different bins primarily according to the amount of leptons in an event, as well as the numbers of electrons and muons within these constrains. Therefore, changes in the final state can not only skew the results of this study through so called *bin migration*, where events of a specific final state affect the performance results for another final state configuration, but also can be responsible for the Z reconstruction to become impossible using the in chapter 6 described method. To quantify the effects of these changes on the final results the matrix depicted in figure 4.2 displays the different migration paths with their respective count from a total of 784250 events.

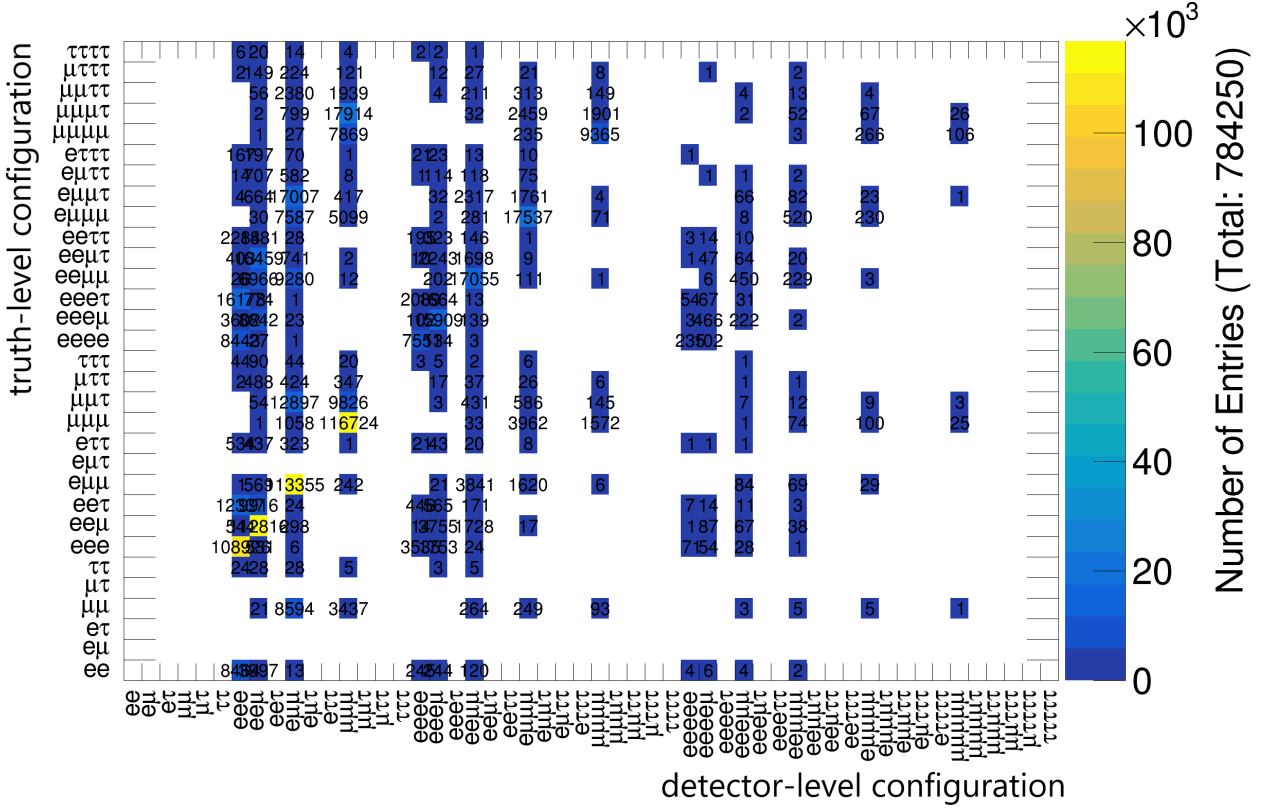


Figure 4.2: Bin migration matrix.

As the entries on the diagonal from the bottom left to the upper right corresponds to unchanged lepton configurations from truth- to detector-level data, the off-diagonal matrix elements represent different forms of bin migration and are more important for this study. While the majority of events remains in the same lepton configuration after the detector simulation took place, namely 66.20% for the total of events (3L: about 68% for each bin, 4L: between 55% and 67%), a substantial amount differs in the final state by mainly one lepton which is either missing or added, leading to a three-lepton-to-four-lepton migration or vice versa, or has been exchanged for the lepton of another flavour. For three lepton events this happens in roughly 31% of the cases, while this percentage is between 29% and 41% for four lepton events. Therefore more exotic changes occur in about 1% in three leptons events and in roughly 4% of four lepton events.

Additionally, it is to say, that some of these changes happening in the same event, while leading to the same final state, can not be separated from the unchanged events on the diagonal. Nevertheless this process is highly unlikely and should not have a huge effect on the resulting Z boson reconstruction efficiencies.

The effect of this bin migration matrix from figure 4.2 on the final results of this analysis is further discussed in the event selection chapter 5 in section 5.4.

## 5 | Object and event selections

To study the desired properties of  $t\bar{t}Z$  events, some combinations of decay channels mentioned in sections 2.2 and 2.3 are more suitable for this task than others. In this chapter, first, a baseline for the definitions of different physics objects is established. After that, in order to prepare the reader for the Z boson reconstruction chapter 6, the criteria and specific cuts for the final event selections are presented.

### 5.1 Object definitions

The very first step in reconstructing a hadron collision through measurements of a detector is to locate the origin of all particles produced from only one hard scattering interaction of two protons. Therefore, the coordinates of the point of collision, also called the *primary vertex* have to be found. Primary vertices are established by extrapolating different particle trajectories to check whether at least three intersect with each other. These have to in total correspond to particles whose summed up transverse momenta exceed 400 GeV and have their individual pseudorapidities fulfilling  $|\eta| < 2.5$  [47]. All primary vertices of one bunch crossing then make up the so called *pile up* in data acquisition. The subsequent event processing from that point has been described in the previous section 3.3.2.

After being assigned to a single primary vertex, tracks and signals can be further specified. To decide what kind of physics object is represented by these recorded signals, certain criteria have to be applied. These are laid upon the signal or measured values to give a threshold for their rejection or acceptance as a particle. Since we expect  $t\bar{t}Z$  event signals to include leptons and jets these are the two categories in need for classification constraints in order to assure reproducibility of the results of this analysis from data taken by real-world detectors. More specifically, we define thresholds for electrons and muons, as well as for jets and b-jets in particular. Tauons are ignored for reasons listed in section 5.2.2. [5]

|           | $e$  | $\mu$            |
|-----------|--|------------------|
| $ \eta $  | $< 2.47$<br>(except $1.37 <  \eta  < 1.57$ ) | $< 2.47$         |
| $p_T$     | $> 7$ GeV                                    | $> 7$ GeV        |
| quality   | MediumLH                                     | Medium           |
| isolation | FCTight                                      | FCTightTrackOnly |

Table 5.1: Electron and muon definitions according to [5].

|           | $jets$                       | $b-jets$                       |
|-----------|------------------------------|--------------------------------|
| $ \eta $  | $< 2.5$                      | $< 2.5$                        |
| $p_T$     | $> 25$ GeV                   | $> 25$ GeV                     |
| selection | collection:<br>AntiKt4EMTopo | b-tagging:<br>MV2c10 algorithm |

Table 5.2: Jet definitions according to [5].

The most basic constraints target the direction as well as the momentum of the measured particles. On one hand, the absolute value of particles' and jets' pseudorapidity  $|\eta|$  describes, as stated in section 3.3.3 on the ATLAS coordinate system, how close the respective trajectory lies to the beam axis. Here,  $|\eta| = 2.5$  corresponds to an angle of  $10^\circ$  between the beam and the trajectory while a pseudorapidity of  $|\eta| = \infty \hat{=} 0^\circ$  describes a parallel track to the beam axis and  $|\eta| = 0 \hat{=} 90^\circ$  corresponds to an orthogonal one. Since the ATLAS detector lacks the ability to detect particles with trajectories closer than  $10^\circ$  to the beam axis, these are excluded from this analysis as well. In addition to the 2.47 upper pseudorapidity limit for electrons, an exception for pseudorapidities of absolute values  $|\eta|$  bigger than 1.37, but smaller than 1.52, is set up. This corresponds to the *LAr crack* in the ATLAS detector hindering optimal electron tracking, promoting fake and non-prompt electrons. Simulated electrons with trajectories in this  $|\eta|$  area are excluded for the same reason given above. On the other hand, particles which are measured to have transverse momenta smaller than 7 GeV for leptons and 25 GeV for jets are left out of the analysis in order to follow the ATLAS recommendations. [35, 5]

Furthermore, there are a few different working points for quality and isolation of the detection of the electrons and muons itself. Required working points for particles are in the case of electrons **MediumLH** describing the detection quality and **FCTight** corresponding to its isolation. For muons in the same order these are **Medium** and **FCTightTrackOnly**. Explanations of the specific quality and isolation working points can be found in [48] and [5].

Jets are collected by the *anti- $k_T$*  collection algorithm `AntiKt4EMTopo` with distance parameter  $R$  set to 0.4 and `EMTopo` jet calibration [49]. For *b-tagging* the `MV2c10` algorithm is used as a standard recommendation made by the ATLAS collaboration [50].

## 5.2 Relevant decay channels for Z boson reconstruction

Specifically in the case of investigating Z boson reconstructions, some decay channels of  $t\bar{t}Z$  events are better suited than others for the task. While some leave a mere binary decision or even only a single possible pairing of particles to the Z boson's decay particles, for  $Z \rightarrow ll$  this decision is often more ambiguous. Other events make the reconstruction very difficult in the sense of very unpredictable signals in the final state. In the next subsections examples for these possibilities are given, which are separately further discussed. In the end detector-level cuts for the used data samples, resulting from the arguments given, are presented.

### 5.2.1 Exclusion of two lepton events

The reconstruction of events with less than three and especially with two leptons in the final state is very straight forward. Independent of whether the Z boson decays leptonically or not, either those two leptons do or do not originate from the Z boson. This decision is easily determined through rough kinematic measurements of the lepton pair in comparison to the Z boson's mass and their respective trajectories. Errors, as in incorrectly matched particles, occurring in this step of the event reconstruction are primarily due to fakes or misidentified particles and since improvement of fake and misidentification rejection is not the primary goal of this study we are not interested in these events, which potentially introduce a grand source of noise and flawed results. Moreover, the here implemented reconstruction method for the Z boson would not be able to reconstruct many of these likely to be misleading events successfully in the case of fakes or misidentification. In addition to that, the underlying parent analysis to this thesis, ATLAS-CONF-2020-028 [5], does not include two lepton events in the first place. For these reasons sub-three lepton events are excluded on detector-level.

### 5.2.2 Exclusion of events containing tauons

The short lifetime  $\tau_\tau$  of tauons  $\tau$  typically leads to short mean decay lengths  $L$  which again leads to them decaying inside of the detector volume, either hadronically (64%) into quarks or leptonically (36%) into a lepton and two neutrinos. These decays often produce ambiguous event signatures and both come with their own drawbacks. The disadvantages of including tauon featuring events will be elucidated in a general picture concerning the whole event, but also for the specific options of the tauon's appearances in the following paragraphs.

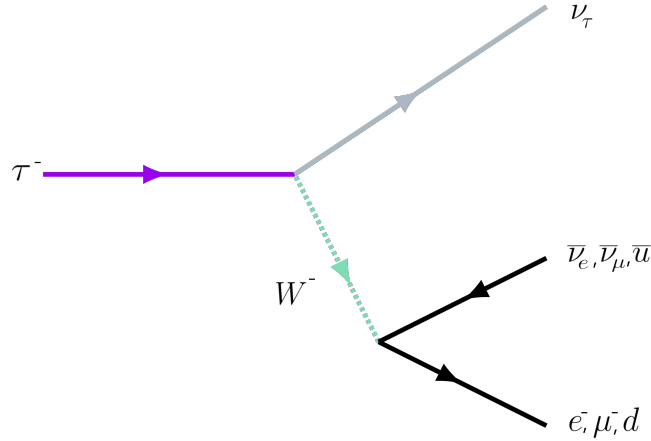


Figure 5.1: Decay of tauons via weak interaction into leptons or quarks.

Firstly, the hadronic tauon decay leads to an increase in the number of jets through strong interactions of the quarks while decreasing the amount of leptons detected in the final state. That often will lead to sub-three lepton final states which, while considering the subsection 5.2.1 above on the exclusion of two lepton events, makes for another disadvantage of  $\tau$ -including events in itself.

Secondly, the leptonic decay of tauons is not only partially incorporated into the study via the electron and muon cases resulting in similar final states, but also generates two additional neutrinos, namely a tauon neutrino  $\nu_\tau$  and a neutrino according to the generation of the charged lepton. This leads to higher transverse missing energy  $E_T^{miss}$  and, because of the plurality of neutrinos, to a loss of every kinematic knowledge to each of them individually.

In order to be able to correctly reconstruct the Z boson in the  $Z \rightarrow \tau^+\tau^-$  decay channel, besides the need for a di-leptonic decay of the tauon pair, the flavour of both decay leptons has to match (same flavour (SF) lepton pair). While the probability of that is only around 6.5%, all other outcomes, namely different flavour (DF) leptons (6.5%), a semi- (46%) or an all-hadronic  $\tau^+\tau^-$  decay (41%), will not allow a correct reconstruction given the criteria presented in chapter 6.

The decay of both W bosons to at least one tauon  $\tau$ , via  $W^+W^- \rightarrow \tau^\pm + X$  or  $W^+W^- \rightarrow \tau^+\tau^-$ , is the other possible source of them with a branching ratio of roughly 21% in context of all possible  $W^+W^-$  decays. Here, there is no need for specific flavours of leptons produced through the leptonic  $\tau$  decay in order to reconstruct the Z boson, but still the threshold of at least one electron  $e$  or muon  $\mu$  from the top quarks has to be met for events to sensibly contribute to this analysis. Considering all different possible channels with their respective branching ratios, only in about half of the cases (52%) of  $W^+W^- \rightarrow \geq 1 \tau$  decays this threshold is met.

Therefore,  $t\bar{t}Z$  events with decay paths containing at least one tauon  $\tau$  at some point are ideally excluded from this analysis as they come with sufficiently serious drawbacks. However, since this analysis should reflect the real-world application of the reconstruction method which is described in chapter 6, we only use detector-level data to exclude any event. This

should not be a huge problem for  $Z \rightarrow \tau^+\tau^-$  events since only 6.5% of these qualify for consideration in the first place. For events the  $\tau$  leptons of which originate from W bosons this is more complicated since 52% pass the thresholds that are put in place. The investigation and planned exclusion of these potential sources of error brings us to the introduction of *signal regions* in section 5.3.

### 5.3 Signal regions

To further clean the samples from events, not only tauon including ones but with in general especially misleading final states, as well as to separately investigate and compare events which suit the before presented general rules for consideration in this analysis, but still are of inherently distinct configurations among one another, so called *signal regions* are introduced. In this regard the signal regions are again adopted from the ATLAS-CONF-2020-028 analysis [5]. Split into regions targeting three and four lepton events, they differ in the amount of jets as well as in how many of them are tagged as b-jets at different specific working points and with which strategies. In addition to that, some further conditions on the leptons themselves are applied.

For the three three lepton or *trilepton* signal regions, displayed in table 5.3, either one or two jets, of in total three or four, with  $p_T > 25$  GeV are required to be b-tagged while being labelled according to whether *pseudo continuous b-tagging* (PCBT) was used or not. Moreover, one of them is designed for the differential measurement specifically, while the other two aid the inclusive measurement. The three leptons have to include at least one OSSF lepton pair fitting in a 10 GeV mass window around the Z boson while the combined mass of all possible OSSF pairs is required to surpass 10 GeV for a start. Other than that, the leptons have to have transverse momenta larger than 27, 20 and again 20 GeV when sorted in a descending order according to their  $p_T$ .

In the different four lepton or *tetralepton* cases from table 5.4 the signal regions are separated according to the b-jet amount of either one or two at different working points in addition of the information whether their opposite sign lepton pairs are of *different flavours* (DF) or *same flavours* (SF). The requirements on OSSF pairs are the same as for three lepton events while the individual leptons have to have a minimum transverse momentum of 27, 20, 10 and 7 GeV ordered with descending  $p_T$ 's. Of all registered jets at least two need to have transverse momenta larger than 25 GeV. In contrast to the three lepton signal regions, here, in the SF case, also a mass window of either bigger or smaller than 10 GeV for the *non-Z lepton pair* for electron pairs and muon pairs, respectively, as well as a missing transverse energy larger than 50 or 100 GeV.

The effects of these cuts and whether they improve the reconstruction of events in general are discussed in the next section.

| Variable                         | 3l-Z-1b4j-PCBT<br>inclusive   | 3l-Z-2b3j-PCBT<br>inclusive | 3l-Z-2b3j-diff<br>differential |
|----------------------------------|---|-----------------------------|--------------------------------|
| $N_l(l = e, \mu)$                | = 3   |                             |                                |
|                                  | $\geq 1$ OSSF lepton pair with $ m_{ll}^Z - m_Z  < 10$ GeV<br>for all OSSF combinations: $m_{\text{OSSF}} > 10$ GeV |                             |                                |
| $p_T(l_1, l_2, l_3)$             | $> 27, 20, 20$ GeV  |                             |                                |
| $N_{jets}(p_T > 25 \text{ GeV})$ | $\geq 4$  | $\geq 3$                    | $\geq 3$                       |
| $N_{b-jets}$                     | = 1 @ 60%   | $\geq 2$ @ 70%              | $\geq 2$ @ 85%                 |
|                                  | veto add. b-jets@70%  |                             |                                |

Table 5.3: Three lepton signal regions from [5].

| Variable  | 4l-DF-1b  | 4l-DF-2b        | 4l-SF-1b                           | 4l-SF-2b                           |
|---|---|-----------------|------------------------------------|------------------------------------|
| $N_l(l = e, \mu)$                                 | = 4   |                 |                                    |                                    |
|   | $\geq 1$ OSSF lepton pair with $ m_{ll}^Z - m_Z  < 10$ GeV<br>for all OSSF combinations: $m_{\text{OSSF}} > 10$ GeV |                 |                                    |                                    |
| $p_T(l_1, l_2, l_3)$                              | $> 27, 20, 10, 7$ GeV   |                 |                                    |                                    |
| $ll^{\text{non-Z}}$                               | $e^\pm \mu^\mp$   | $e^\pm \mu^\mp$ | $e^\pm e^\mp$ or $\mu^\pm \mu^\mp$ | $e^\pm e^\mp$ or $\mu^\pm \mu^\mp$ |
| $ m_{ll}^{\text{non-Z}} - m_Z  (e^\pm e^\mp)$     | -   | -               | $> 10$ GeV                         | $> 10$ GeV                         |
| $E_T^{\text{miss}} (e^\pm e^\mp)$                 | -   | -               | $> 50$ GeV                         | -                                  |
| $ m_{ll}^{\text{non-Z}} - m_Z  (\mu^\pm \mu^\mp)$ | -   | -               | $< 10$ GeV                         | $< 10$ GeV                         |
| $E_T^{\text{miss}} (\mu^\pm \mu^\mp)$             | -   | -               | $> 100$ GeV                        | $> 50$ GeV                         |
| $N_{jets}(p_T > 25 \text{ GeV})$                  | $\geq 2$  | $\geq 2$        | $\geq 2$                           | $\geq 2$                           |
| $N_{b-jets} @ 85\%$                               | = 1   | $\geq 2$        | = 1                                | $\geq 2$                           |

Table 5.4: Four lepton signal regions from [5].

## 5.4 Final event selection

After the sample's detector-level final states are cleaned by taking the precautions described in the two previous sections 5.2 and 5.3, the considered events should have very clean final states, ideally containing only few  $W^+W^- \rightarrow \geq 1 \tau$  and  $Z \rightarrow \tau^-\tau^+$  events, as well as represent less exotic decay channels in combination with fewer interactions between the decay particles themselves and with the detector material. One way to check this is by re-considering the bin migration matrix from the Monte Carlo sample section 4.3 in figure 4.2. When only taking events into account which meet all criteria necessary for consideration on detector-level one obtains the "cleaned up" bin migration matrix in figure 5.2.

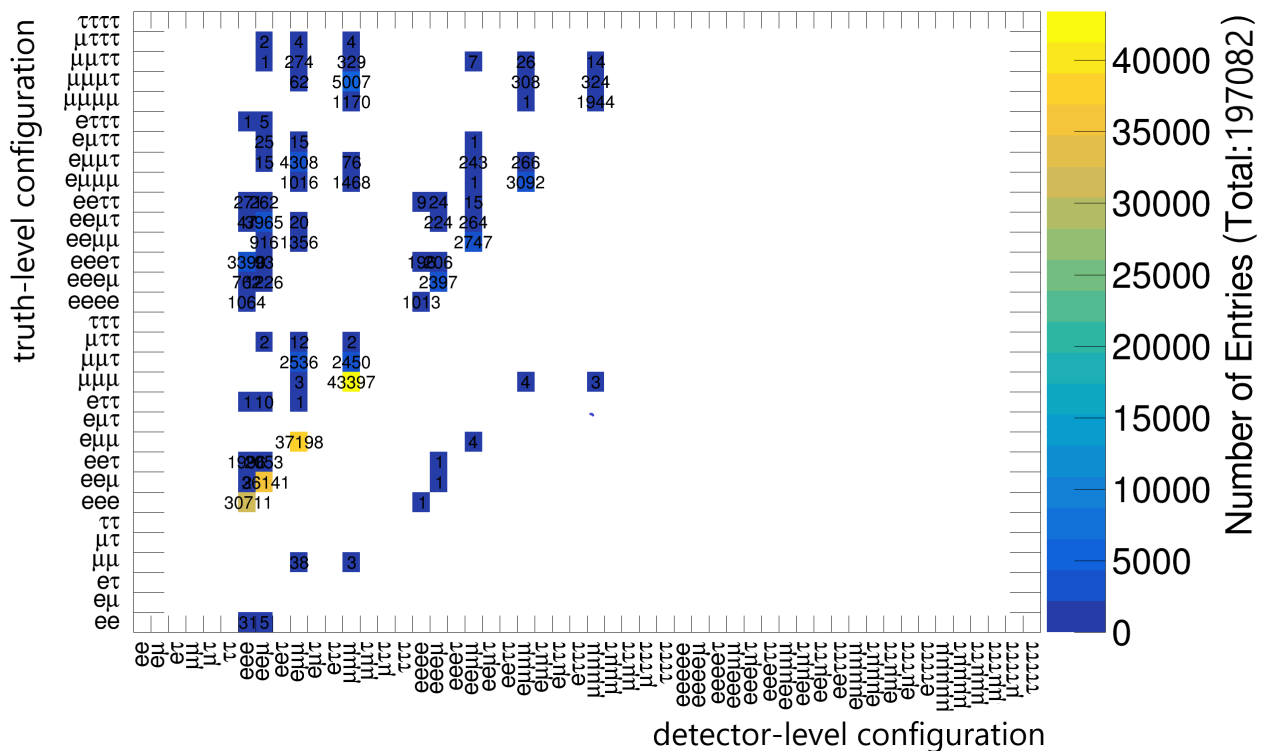


Figure 5.2: Bin migration matrix after decay channel selection and signal regions.

While there are far less non-diagonal elements in this iteration of the bin migration matrix, especially less exotic ones far from the diagonal, the number of entries in bins on the diagonal also decreased drastically. Nevertheless, the percentage of entries on the diagonal in comparison to the total number of matrix entries has gone up from 66.20% to 75.42%, indicating cleaner final states overall. Additionally, when investigating the exclusion of events including tausons on truth-level one notices that only 2% of  $Z \rightarrow \tau^-\tau^+$  events and 20% of  $W^+W^- \rightarrow \geq 1 \tau$  events pass the kinematic thresholds and signal region restrictions put in place. This means that  $Z \rightarrow \tau^-\tau^+$  are almost entirely excluded by the signal regions presented in section 5.3 above, as well as the majority of events with W bosons decaying to

tauons. However, whether these passing events in the latter case are still reconstructible can not be said from these numbers alone.

To confirm reconstructability of the detected final states for each detector-level bin's entries, one can check whether any of the possible  $Z$  boson decay channels of each bin could be reproduced from the actual underlying truth-level event. For example in the case of a detector-level  $ee\mu$  configuration, instances where there were two electrons in the first place allow for a chance of successful reconstruction on detector-level by giving the possibility for a  $Z \rightarrow e^+e^-$  decay on truth-level. Events for which this criteria is not met, information on the underlying particle configuration on truth-level is lost and the event becomes unrecoverable. The most contributions of definitively unrecoverable events to any bin, with around 60 in total, have the otherwise in reconstruction unambiguous configurations of  $ee\mu$  and  $e\mu\mu$ , while all others have none or almost none. This yields percentages of unrecoverable events in the  $ee\mu$  and  $e\mu\mu$  channel of about 0.5%, meaning that these few unrecoverable events have almost certainly only a negligible influence on the results presented in this analysis, which validates the effectiveness of the signal regions and allows to proceed with including the  $Z \rightarrow \tau^-\tau^+$  sample into the analysis without having to adjust heavily for unrecoverable events, keeping this analysis comparable to analyses using recorded data from the ATLAS detector.

#### 5.4.1 Summary of selected decay channels

In conclusion of this decay channel selection, all in this analysis considered  $t\bar{t}Z$  detector-level decay channels are summarized in figure 5.3 with the condition that while any  $W$  boson decays hadronically, the other one does not do so.

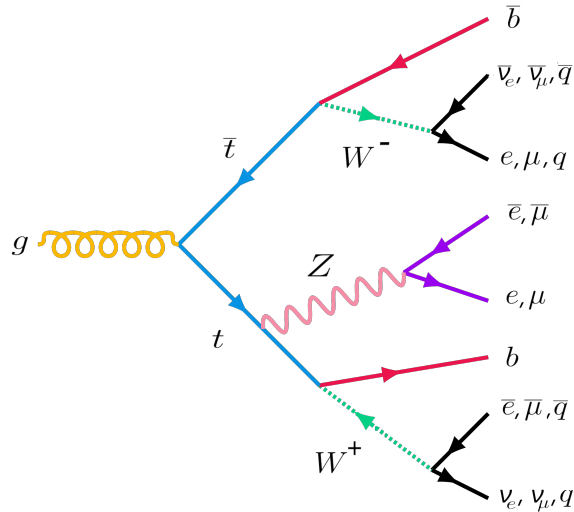


Figure 5.3: Selected  $t\bar{t}Z$  decay channels.

This leaves us with events of three or four leptons (electrons  $e$  and muons  $\mu$ ) in the, therefore, relatively clean final state, making investigations into the  $t$ - $Z$ -coupling easier or even

possible in the first place. Calculating the total proportion of events left with their according branching ratios  $\Gamma$  from figure 5.4 via

$$\Gamma(t\bar{t} \rightarrow e^\pm/\mu^\pm + jets) \cdot \Gamma(Z \rightarrow e^+e^-/\mu^+\mu^-) = 0.34 \cdot 0.07 \approx 2.4\% \text{ for 3L events and}$$

$$\Gamma(t\bar{t} \rightarrow e^+e^-/\mu^+\mu^-) \cdot \Gamma(Z \rightarrow e^+e^-/\mu^+\mu^-) = 0.07 \cdot 0.07 \approx 0.5\% \text{ for 4L events}$$

approximately 3% of all  $t\bar{t}Z$  events are being considered in this analysis.

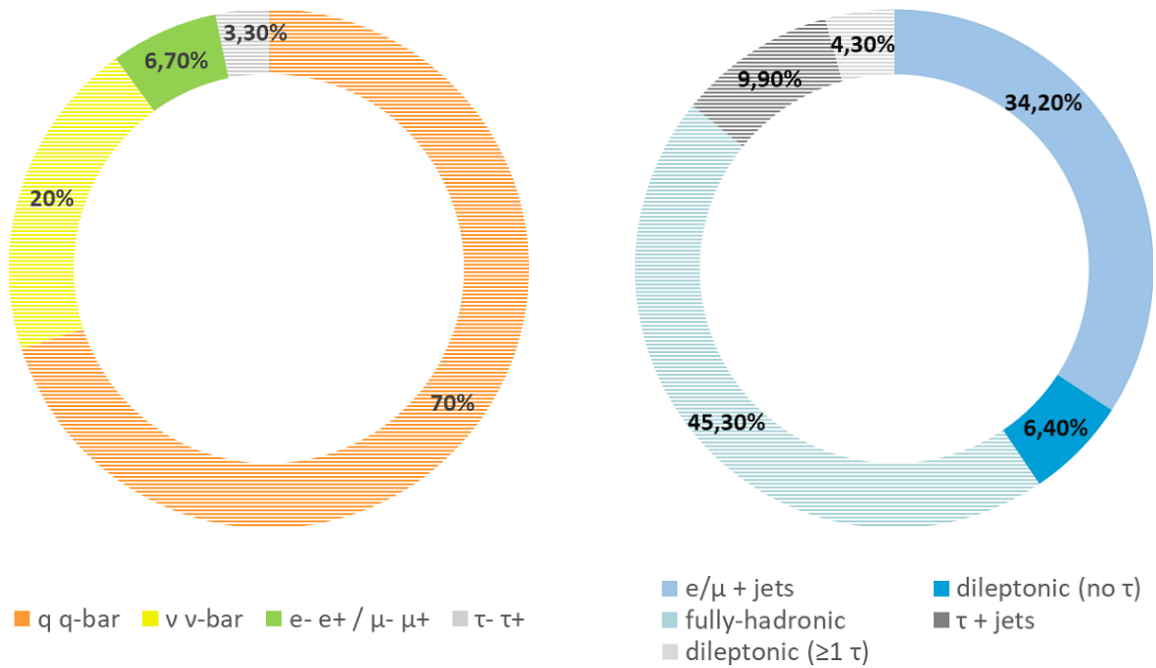


Figure 5.4: Branching ratios of the selected  $t\bar{t}Z$  decay channels.



## 6 | Z boson reconstruction

In order to examine  $t\bar{t}Z$  events in general, be it the kinematics or different couplings, one has to identify the many signals registered from the various detector sub-systems as originating from an in association produced top-anti-top quark pair, Z boson combination in the first place. If this process is not working sufficiently efficient, meaning events are taken for  $t\bar{t}Z$  events even though they are not, the results of the respective study are skewed. Hence, this thesis focuses on investigating the performance of the current Z boson reconstruction method as well as on trying to improve its efficiency.

This chapter starts by giving a quick insight into the status quo of Z boson reconstruction in the ATLAS  $t\bar{t}Z$  Group's latest ATLAS-CONF-2020-028 analysis [5] and then presents specifically a reference histogram based method, with its key features and resulting efficiencies, to increase the reconstruction efficiency.

### 6.1 Motivation and status quo

The parent analysis to this thesis, ATLAS-CONF-2020-028 [5] by the ATLAS Collaboration, is measuring the inclusive and differential production cross sections of  $t\bar{t}Z$  events at  $\sqrt{s} = 13$  TeV with the ATLAS detector focusing on final states with either three or four isolated leptons, and therefore leptonically decaying Z bosons, in the final state. For both the inclusive as well as the differential measurements an initially correctly reconstructed  $t\bar{t}Z$  event is crucial. Any contribution from events with kinematics not actually representing  $t\bar{t}Z$  processes contaminates the overall results and makes it more difficult to extract the fundamental couplings and production cross sections.

Currently the Z boson is reconstructed solely by selecting the first encountered instance of an opposite-sign-same-flavour (OSSF) lepton pair that fits inside a 10 GeV mass window around the Z boson mass of  $m_Z = 91.1876$  GeV. By doing so, they achieve Z boson reconstruction efficiencies of up to 99.80% and 96.66% in the best performing and as low as 96.36% and 90.87% in the worst performing bin for three and four lepton events, respectively. These are also displayed in figure 6.1 for three lepton events and figure 6.2 for four lepton events with the corresponding errors in the table on the right-hand side. Information on the uncertainties displayed there are given in section 6.5.2.

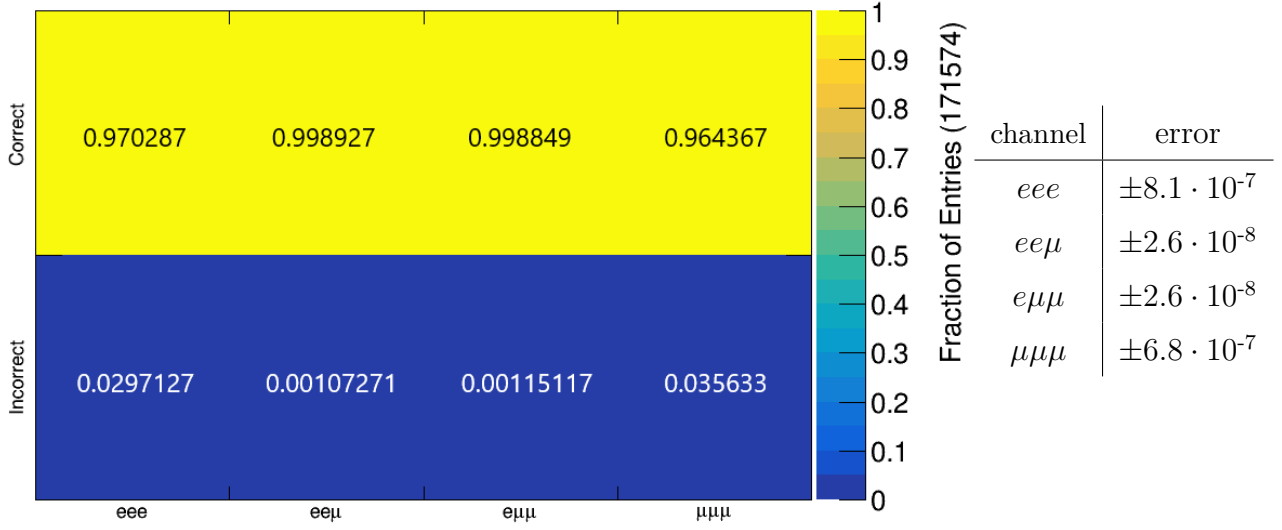


Figure 6.1: Initial three lepton event efficiencies of the Z boson reconstruction.

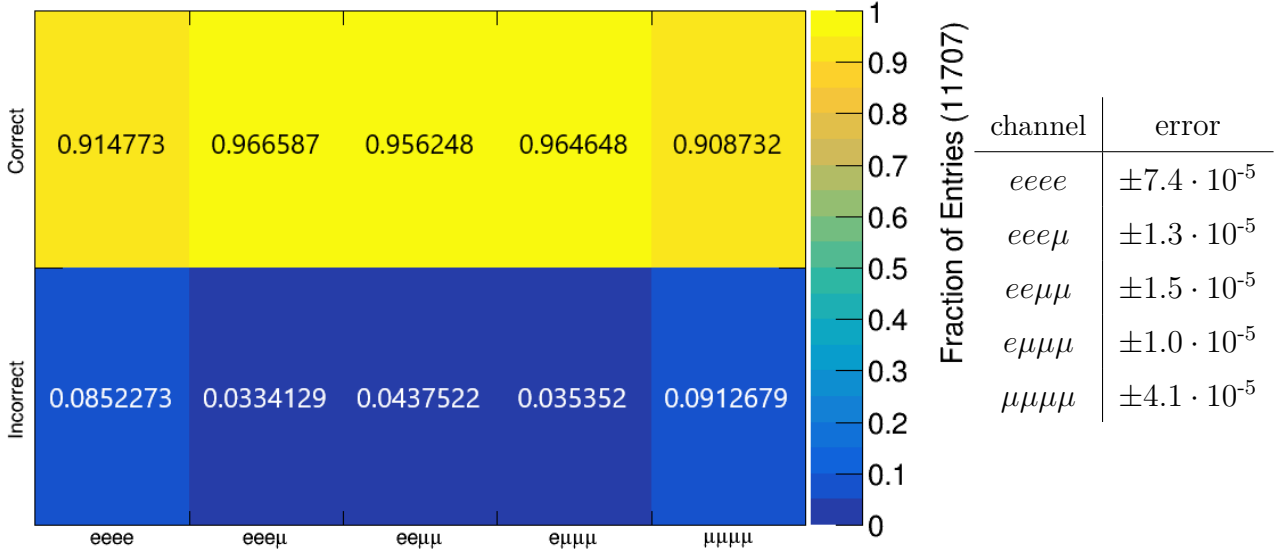


Figure 6.2: Initial four lepton event efficiencies of the Z boson reconstruction.

This current method, despite efficiencies beyond 90% for every configuration bin, leaves some room for improvement in a couple of regards. Especially in the *all-same-flavour* channels of both three and four lepton events these efficiencies drop. A less rigid Z boson acceptance threshold in combination with a recursive selection method for the lepton pair, amongst

other things, could improve the efficiencies. These hypotheses, alongside some other ideas, are discussed and tested in the following sections. The subsequent findings and results of that testing are then presented at the end in section 6.6.

## 6.2 Method of reconstruction

For this study a so called *truth-matching method* in combination with the implementation of *reference histograms* was selected to be investigated for aptitude and performance in the reconstruction of leptonically decaying Z bosons. To prepare the reader for upcoming descriptions of the testing in combination with the results, the basic concept of the said method is briefly introduced first.

### 6.2.1 Truth-matching

*Truth matching* describes the process of *matching* the particles of *truth-level data* to *detector-level data* particles, both specified in subsections 4.3.2 and 4.3.1, respectively. This pairing is done according to specific particle and event properties contained on both data levels in a similar fashion. In this way, properties which only marginally change through the detector simulation can be exploited to match the different representations of particles to one another and can subsequently lead to the identification of the detector-level particles' origin, as well as to insights on how other particle properties are affected by the detector simulation.

Besides obvious choices for distinguishing pairings between the two data levels, like charge and flavour, which have to be the same for any identical particle on both levels, most commonly directional information on the particles is used, i.e. their trajectory. This is possible since hard scattering processes after the initial collision, with, for example, detector material, deflecting particles very significantly off their tracks, are relatively rare. Therefore, the  $\Delta R$  variable is used in this analysis to assign leptons to their same-sign-same-flavour (SSSF) counterparts on the other data level. For all possible SSSF lepton pairs between truth- and detector-level particles  $\Delta R$  values are built and subsequent pairing assignments are made by minimizing the sum

$$\min \left( \sum_{i,j \text{ with } i \neq j}^{N_{SSSF}} \Delta R(i, j) \right)$$

over the number of SSSF lepton pairs  $N_{SSSF}$ . Thereby, we match the decay leptons of the Z boson, identified in the truth-level data, to the particle fitting best for the reconstruction of the entire event to be able to further investigate its properties on detector-level.

### 6.2.2 Reference histograms

Insights gained through matching truth-level data particles to their detector-level description are stored in so called *reference histograms* in order to use them on data sets while not using any truth-level information in order to simulate a detector measurement. These reference histograms contain the count of entries in previously chosen value intervals of a specific variable filled with the properties of the detector-level particle of *successfully* matched *Z* boson decay particle pairs. Thereby, more common variable values of the leptons by truth-matching found to be *Z* boson decay particles, get a higher count or more entries in their corresponding bin. The selection of these variables, as well as the chosen interval for each, are discussed in section 6.3.

These distributions are then scaled so that the bin with the most entries is assigned a value of 1 which corresponds to dividing the entries of every bin by the number of entries of most filled or populated one. With that, each bin obtained a *probability-like* value in order to determine for an arbitrary lepton or lepton pair whether it is likely to be originating from a *Z* boson decay or not.

Moreover, one is able to combine different reference histograms corresponding to distinct variables into one. Therefore, in this analysis we call reference histograms *X*-dimensional if they include information on distributions of *X* variables. Including the dimension of counted entries or the corresponding ratio of them to the maximally filled bin, these then are  $(X + 1)$ -dimensional histograms.

### 6.2.3 Implementation

In order to actually use these reference histogram distributions for deciding which opposite-sign-same-flavour lepton pair to pick to represent the *Z* boson's decay particles, they are implemented into the respective algorithm through *interpolation*. This describes the process of taking the different discrete centers of the associated bins as holding the respective probability-like value assigned by the reference histogram and fitting a continuous distribution to them. The selection algorithm then assigns a probability value or so called *weight* to each possible pairing based on the value the interpolation yields and picks the most likely one. In that manner, very little differences in the pairings likelihoods are resolved and lead to the choice of the statistically most probable *Z* boson decay particle pair.

## 6.3 Variable selection

The variables selected to be used in this method mainly need to fulfil one requirement. To identify the decay particles of a *Z* boson they especially have to discriminate against leptons coming from *Z* boson decays in order to highlight them among all other leptons or lepton pairings. In other terms they have to separate signal and background from each other. In this section, the variables that were tested on truth-level data for their discriminating power are

presented in conjunction with truth-level testing plots which display whether they are suited for reference histograms or not. For the legends of every plot in this section the abbreviations of "d1" and "d2" mean *decay particle 1* and *decay particle 2*, respectively. Additionally, for W bosons "t" and "tb" indicate their origin of either the top quark  $t$  or the anti-top quark  $\bar{t}$ .

### 6.3.1 $m_{\ell\ell}$ and $\Delta m_Z$

Reconstructing a particle by picking an according amount of physics objects, the combined Lorentz vector of which closely resembles their alleged parent particle, based on the conservation of energy, mass and momentum, is one very good way of finding the corresponding decay particles of any relatively massive particle. With, in our case, two OSSF leptons as the desired particle combination in three or four lepton final state settings, which generally produce kinematically clean final states, finding a pair that approximately fits the mass of the Z boson well is, therefore, bound to be very discriminative against other decay particle combinations.

For this search itself we start with the four-vectors,  $P_{\ell_1}$  and  $P_{\ell_2}$ , of an arbitrary pair of leptons,  $\ell_1$  and  $\ell_2$ , and build the variable of the mass of the combined Lorentz vectors  $m_{\ell\ell}$  via

$$m_{\ell\ell} = \sqrt{(P_{\ell_1} + P_{\ell_2})^2} = \sqrt{E_{\ell\ell}^2 - \|\mathbf{p}_{\ell\ell}\|^2}$$

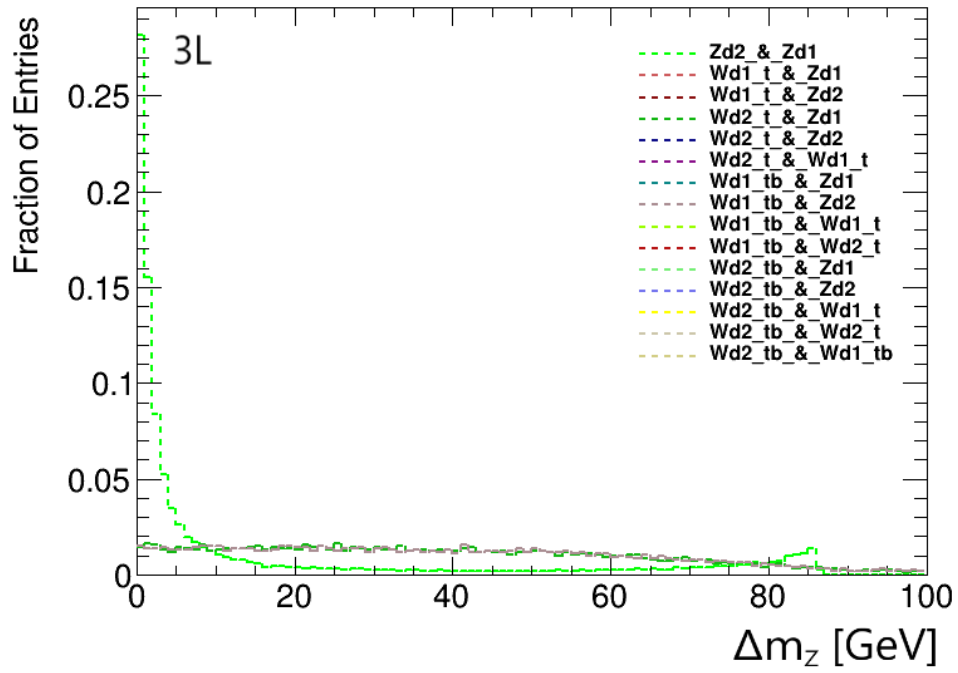
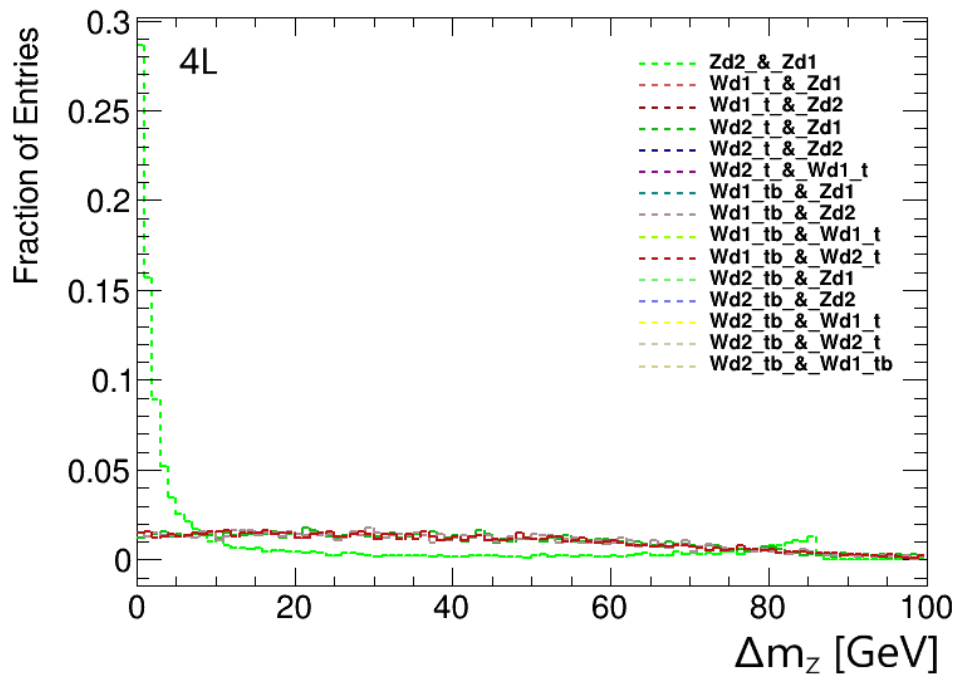
to obtain the approximate mass of a possible parent particle. For easier handling in the Z boson reconstruction of  $m_{\ell\ell}$  it is compared with the Z boson mass  $m_Z = 91.1876$  GeV to find the difference between those two,  $\Delta m_Z$ . This gives us a variable for an instant insight on how closely the tested lepton pair depicts a Z boson or rather the Z boson's mass with

$$\Delta m_Z = m_{\ell\ell} - m_Z = m_{\ell\ell} - 91.1876 \text{ GeV}.$$

Tests with truth-level data produced the plots shown in figures 6.3 and 6.4 to investigate the actual suitability for Z boson reconstruction. Within those one clearly sees a strong peak of entries close to zero, corresponding to masses of Z boson decay lepton combinations, indeed very closely resembling the actual Z boson mass. The mass differences of the background, namely other possible OSSF pairings, are spread across the whole x-axis, leading to a very strong separation.

This strong discriminative power was to be expected, as the currently implemented method also makes use of this variable successfully. Because of that, great performance the  $\Delta m_Z$  variable will be a key component in all multi dimensional reference histograms, supported by further variables which this analysis tries to find in order to achieve even better efficiencies than figures 6.1 and 6.2 show.

In addition to that, one can note very similar results for three and four lepton events. This is taken as an indicator for the need of only one reference histogram for both, three and four lepton events, for each matching method.

Figure 6.3:  $\Delta m_Z$  truth-level testing for three lepton events.Figure 6.4:  $\Delta m_Z$  truth-level testing for four lepton events.

### 6.3.2 $\Delta R(\ell, \ell)$

As a second variable the  $\Delta R$  value of all OSSF lepton pairs  $\Delta R(\ell, \ell)$  is tested. While in the truth-matching process this variable was used to correctly assign the corresponding representations of a single particle in truth- and detector-level data to one another, now  $\Delta R(\ell, \ell)$  is to be understood as an indicator for specific boosts of the parent particle, in our case the *Z* boson, inside the detector in either direction of the *z*- or beam-direction. The stronger this boost is, the closer subsequent decay particles should be to one another, spatially speaking, since the momentum of the parent particle has to be conserved.

Given figures 6.5 and 6.6, a shift in the shape of the distribution towards smaller  $\Delta R(\ell, \ell)$  values can be observed. This indicates that there is a tendency of the trajectories of the *Z* boson's decay particles,  $\ell_{Z,1}$  and  $\ell_{Z,2}$ , to be spatially closer together than those of a randomly chosen OSSF pairing. However, there is a very large overlap of clearly more than 50% area-wise. This means while the said tendency exists, often this tendency will not be true or misleading for any given event.

That is why it can be expected that reference histograms solely based on  $\Delta R(\ell, \ell)$  will perform poorly in comparison with the original method. Nevertheless, it remains to be seen if other methods can be supported in their performance with  $\Delta R(\ell, \ell)$  information.

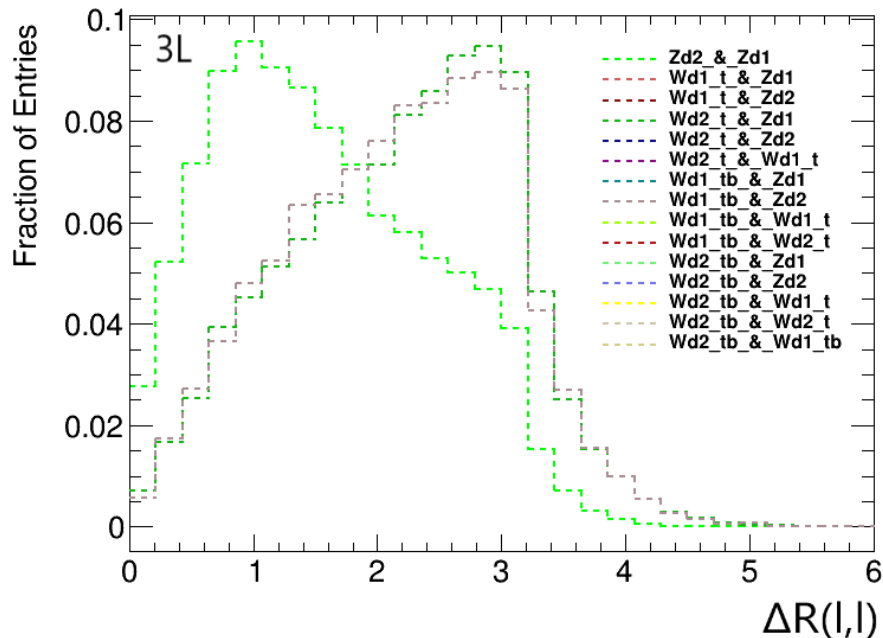


Figure 6.5:  $\Delta R(\ell, \ell)$  truth-level testing for three lepton events.

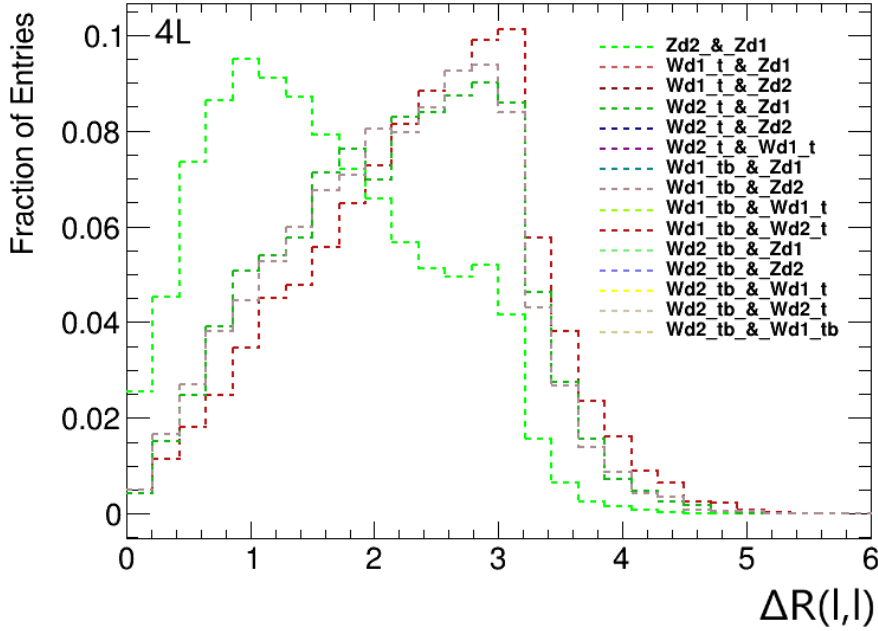


Figure 6.6:  $\Delta R(\ell, \ell)$  truth-level testing for four lepton events.

### 6.3.3 $E_T^{miss}$

While all other variables use properties of single particle or a combination of such, the selection and testing of the  $E_T^{miss}$  variable is more aimed at gaining insight into the general kinematics of events leading to a correct reconstruction of the Z boson through truth-matching in comparison to those causing an incorrect reconstruction. In order to investigate this, the missing transverse energy of events reconstructed correctly, which are, therefore, also considered in the building of reference histograms, as well as of incorrectly reconstructed events are compared in figure 6.7.

There it can be seen, that the magnitude of the missing transverse energy has hardly any effect on the efficiency of truth-matching particles to one another, since the shapes of both distributions for the correctly (green) and for the incorrectly (red) reconstructed Z bosons are almost identical.

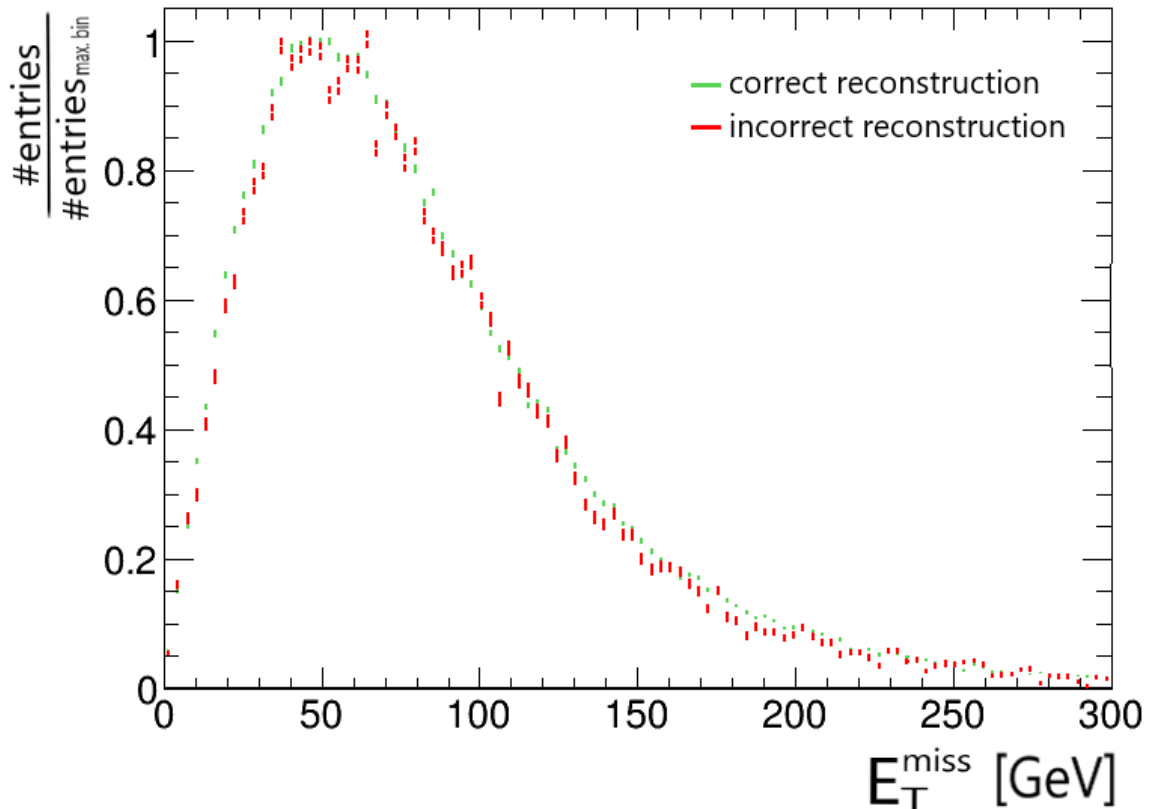


Figure 6.7:  $E_T^{miss}$  of correctly and incorrectly reconstructed events.

### 6.3.4 $\Delta R(\ell, E_T^{miss})$

Also utilizing the missing transverse energy, but focused on its directional information rather than its magnitude by building the  $\Delta R$  value between its calculated trajectory and the tracks of the final state charged leptons, does the variable  $\Delta R(\ell, E_T^{miss})$ . Since the  $E_T^{miss}$  trajectory corresponds to the one of the neutrinos which are produced subsequently to the collision of any event,  $\Delta R(\ell, E_T^{miss})$  could be useful, if Z boson decay particles tend to have trajectories especially close to or far from the  $E_T^{miss}$ 's one.

In figures 6.8 and 6.9 one can see, equally for three and four lepton events, that indeed Z boson decay particles,  $\ell_{Z,1}$  and  $\ell_{Z,2}$ , have a tendency to be aligned to the  $E_T^{miss}$ 's direction with a greater parallel part than other leptons. Nevertheless, this separation of the distributions' shapes is even smaller than for the  $\Delta R(\ell, \ell)$  variable with a very substantial overlap. Therefore, the same arguments apply for  $\Delta R(\ell, E_T^{miss})$  that have been listed for  $\Delta R(\ell, \ell)$ . Whether this small distribution shape shift leads to an improvement of another reference histogram method in contrast to one solely depending on the discriminative power of the  $\Delta R(\ell, E_T^{miss})$  variable is left to be seen in the efficiency section 6.6.

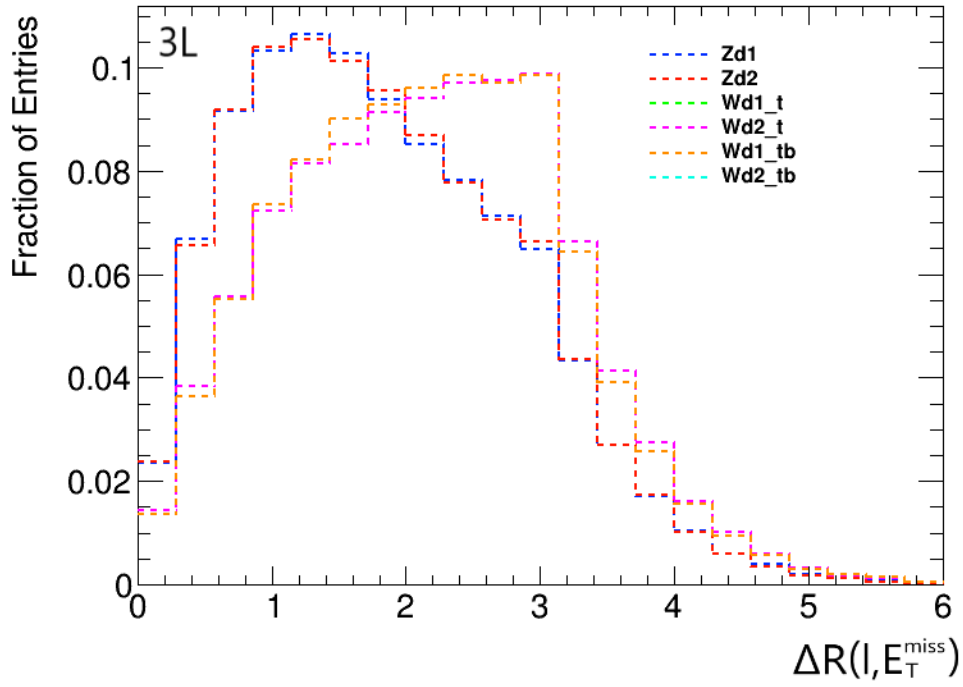


Figure 6.8:  $\Delta R(\ell, E_T^{miss})$  truth-level testing for three lepton events.

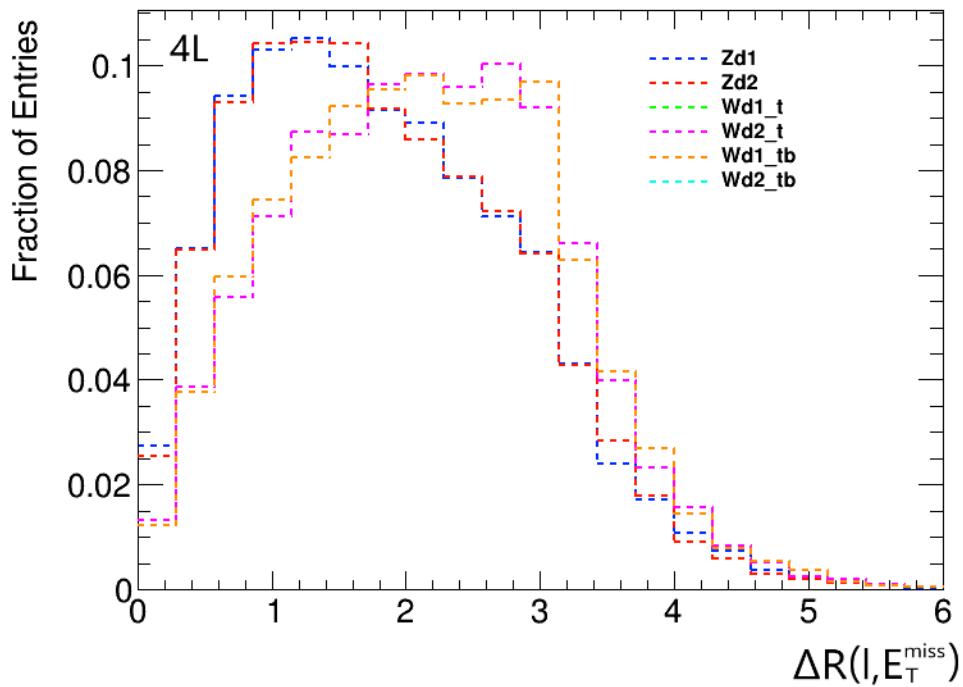


Figure 6.9:  $\Delta R(\ell, E_T^{miss})$  truth-level testing for four lepton events.

### 6.3.5 $\Delta R(Z_{\ell\ell}, E_T^{miss})$

Another variable built with the Lorentz vector of the missing transverse energy is  $\Delta R(Z_{\ell\ell}, E_T^{miss})$ . It does not compare the directions of leptons individually, but the combined ones of OSSF pairings to the  $E_T^{miss}$ 's calculated trajectory. By adding up the leptons' Lorentz vectors the according one of a Z boson candidate  $Z_{\ell\ell}$ ,  $P_{Z_{\ell\ell}}$ , is formed.

However, plotting  $\Delta R(Z_{\ell\ell}, E_T^{miss})$  in figures 6.10 and 6.11 reveals no separation of the actual Z boson decay lepton pairing from the ones of one Z decay lepton with the fitting OSSF lepton from one of the W boson decays. Therefore, the  $\Delta R(Z_{\ell\ell}, E_T^{miss})$  variable will not be suited for employment in the reference histograms.

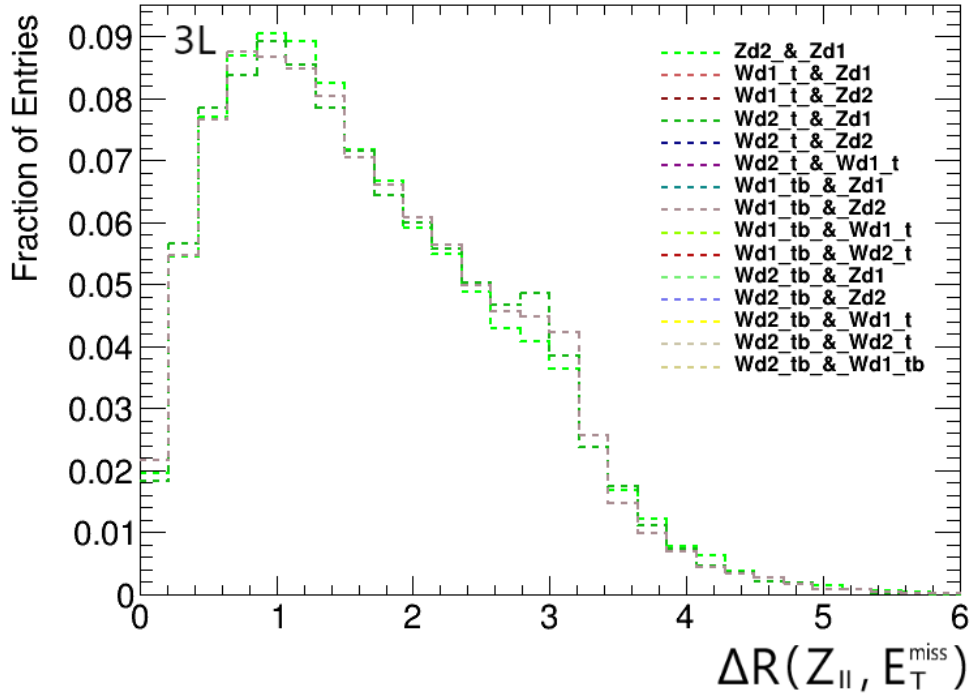


Figure 6.10:  $\Delta R(Z_{\ell\ell}, E_T^{miss})$  truth-level testing for three lepton events.

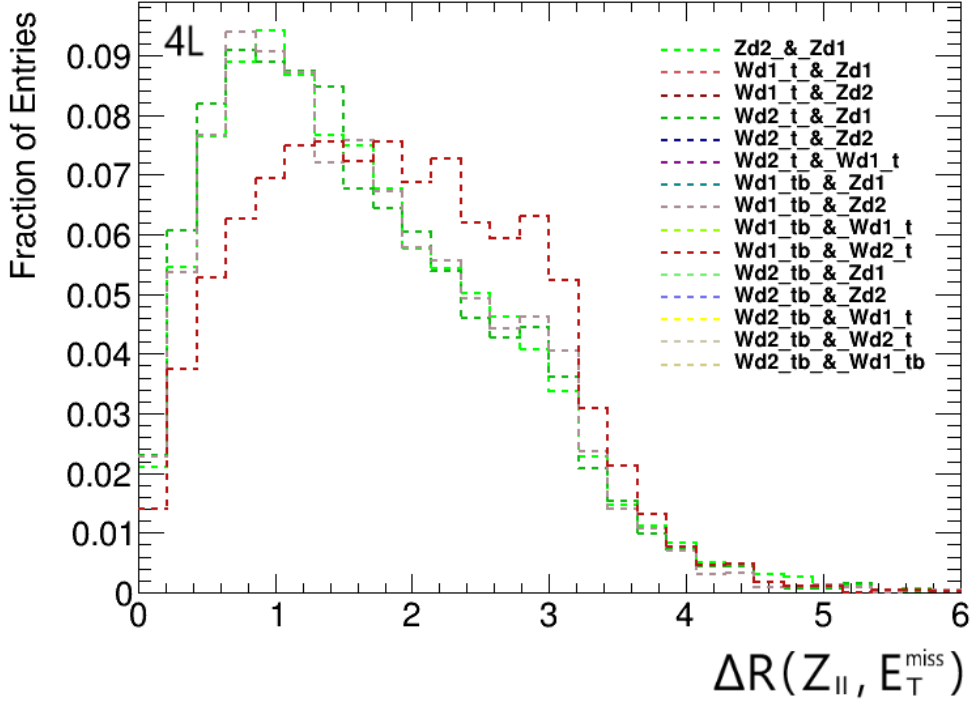


Figure 6.11:  $\Delta R(Z_{\parallel}, E_T^{\text{miss}})$  truth-level testing for four lepton events.

### 6.3.6 $p_T$ -correlation

The variable " $p_T$ -correlation" refers to the quotient of two particles' transverse momenta is hidden. This is done by always choosing the arrangement of the  $p_T$ 's of particles 1 and 2, namely  $p_{T,1}$  and  $p_{T,2}$ , into numerator and denominator so that the bigger one takes the place of the numerator. This leads to the quotient's absolute value being greater than 1. To put it in other terms, we chose

$$\frac{p_{T,1}}{p_{T,2}} \text{ for } p_{T,1} > p_{T,2} \quad \text{and} \quad -\frac{p_{T,2}}{p_{T,1}} \text{ for } p_{T,1} < p_{T,2} ,$$

where the sign of the second quotient was flipped in order to look at both entries separately. As can be seen in figures 6.12 and 6.13, there is almost no difference in the distributions of the Z boson decay particles being combined versus the combination of any randomly chosen OSSF lepton pair. This means, the correlation of the transverse momenta is not suited for the use in reference histograms, neither in three lepton events nor in events with leptons, leading to the variables exclusion from building reference histograms.

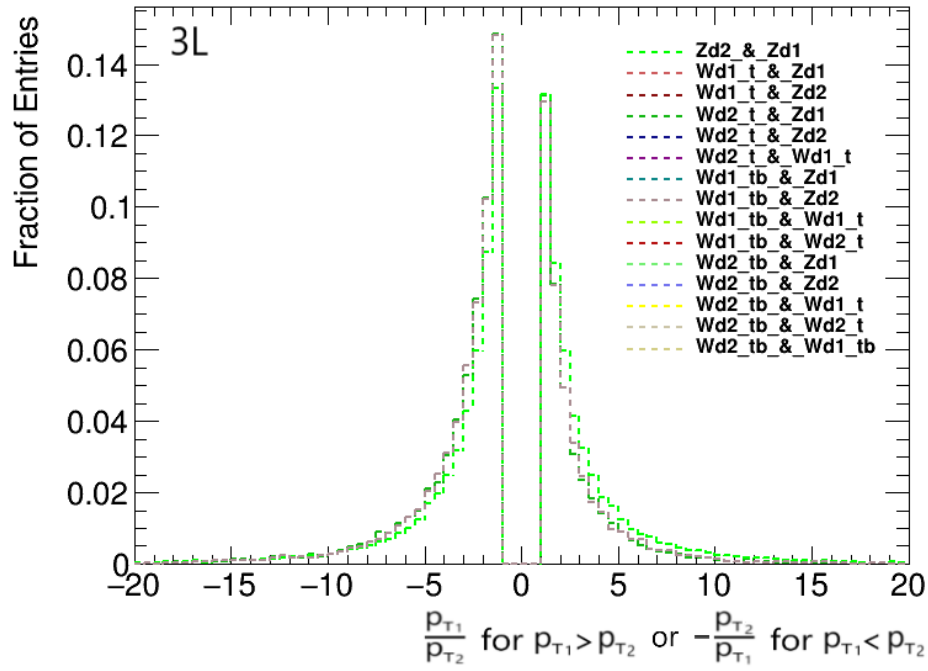


Figure 6.12:  $\frac{p_{T\ell_1}}{p_{T\ell_2}}$  truth-level testing for three lepton events.

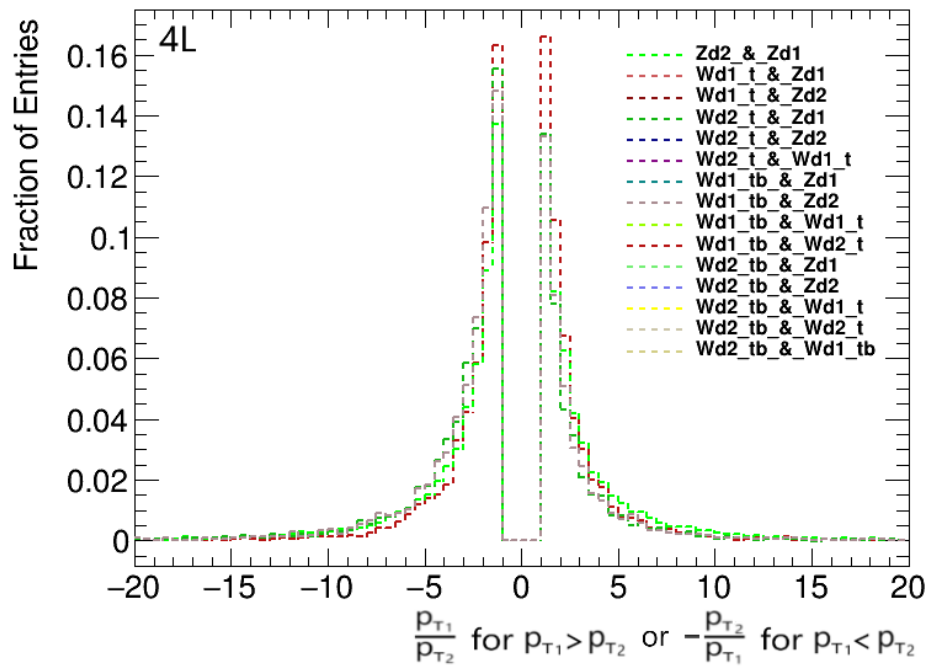


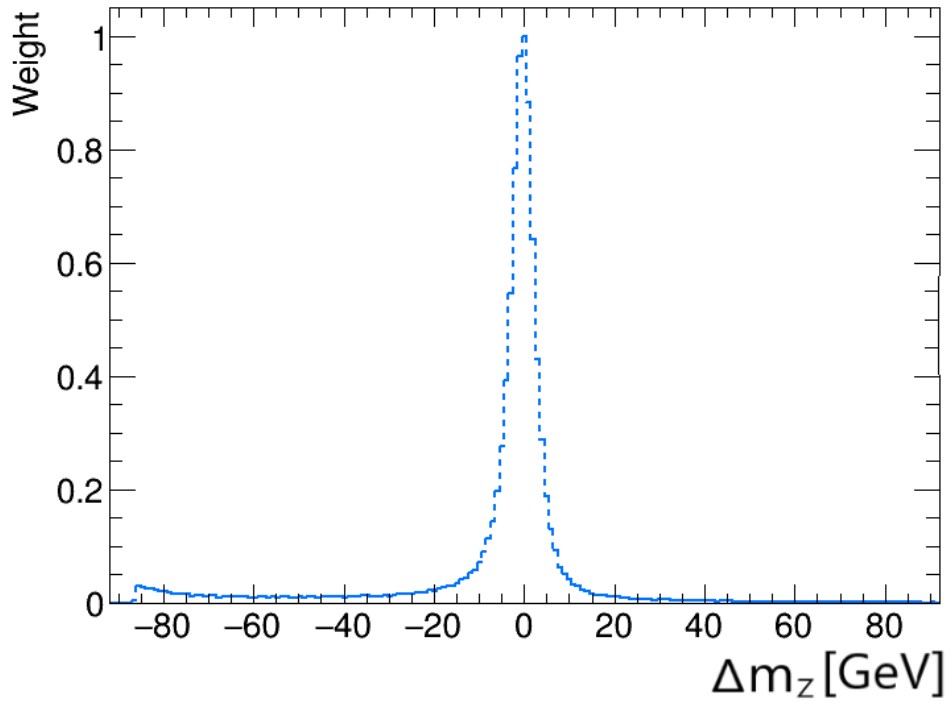
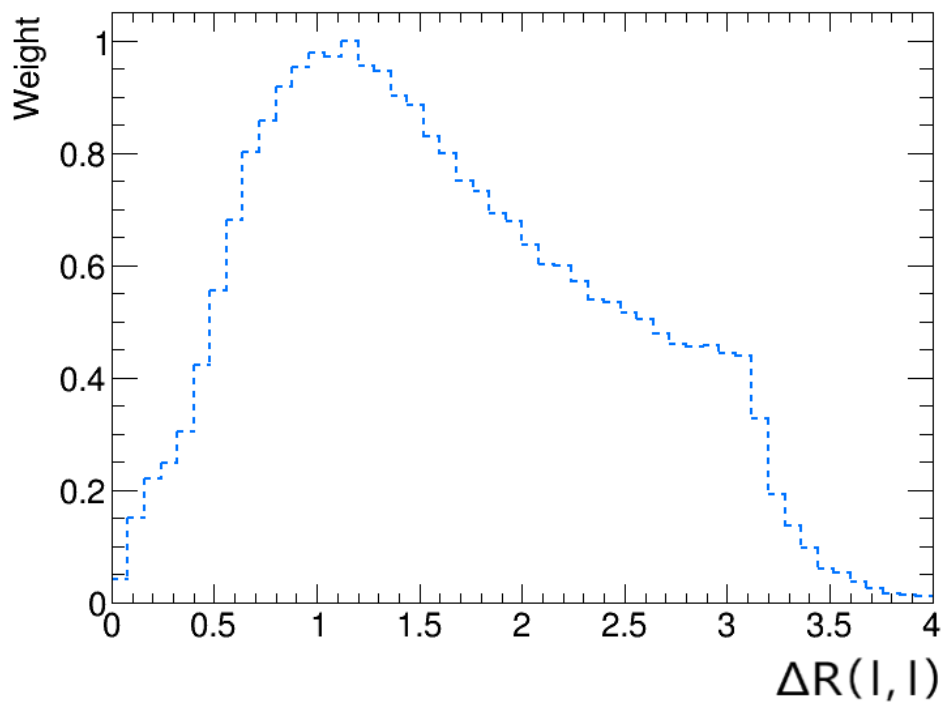
Figure 6.13:  $\frac{p_{T\ell_1}}{p_{T\ell_2}}$  truth-level testing for four lepton events.

## 6.4 Reference histograms

From these variables presented in the previous section 6.3, the ones verified to at least slightly discriminate against Z boson decay leptons are taken to build reference histograms in this section. First, they are presented and used individually for 1D reference histograms, to later combine them as was mentioned before into higher dimensional histogram methods. Therefore, the truth-matched detector-level decay leptons of the Z bosons are counted for each variable interval bin, the resulting quantities of which are displayed on an additional axis. This entry number then is set into relation with the entries of the maximally filled bin to gain a probability-indicating y-axis value. Moreover, it is to mention that, since three and four lepton events showed no fundamental differences in their distributions of the variables derived from the detector-level data, matched lepton pairs from both, three and four lepton signal regions, are combined into one single reference histogram that is implemented into the algorithm.

### 6.4.1 1D reference histograms

Starting with building references for the individual variables proven to have discriminative power according to the selection of Z boson leptons we obtain histograms for  $\Delta m_Z$ ,  $\Delta R(\ell, \ell)$  and  $\Delta R(\ell, E_T^{miss})$ . In the reference histograms for all three of these variables the different values are spread across the x-axis while the relative amount of entries of the according bin is displayed on the y-axis.

Figure 6.14: D ( $\Delta m_Z$ ) reference histogram.Figure 6.15: 1D  $\Delta R(l, l)$  reference histogram.

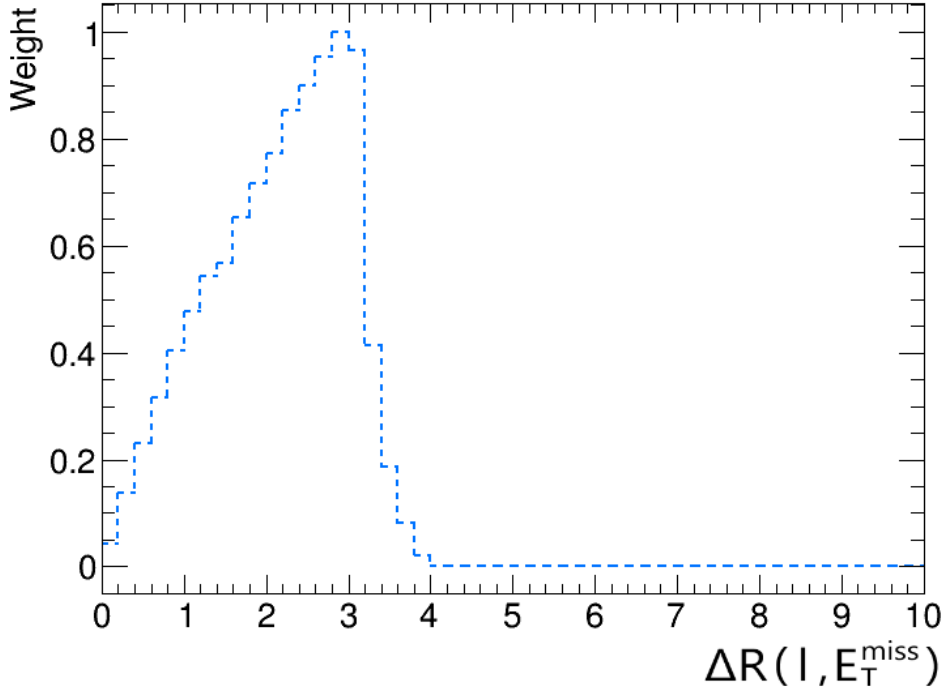


Figure 6.16: 1D  $\Delta R(\ell, E_T^{miss})$  reference histogram.

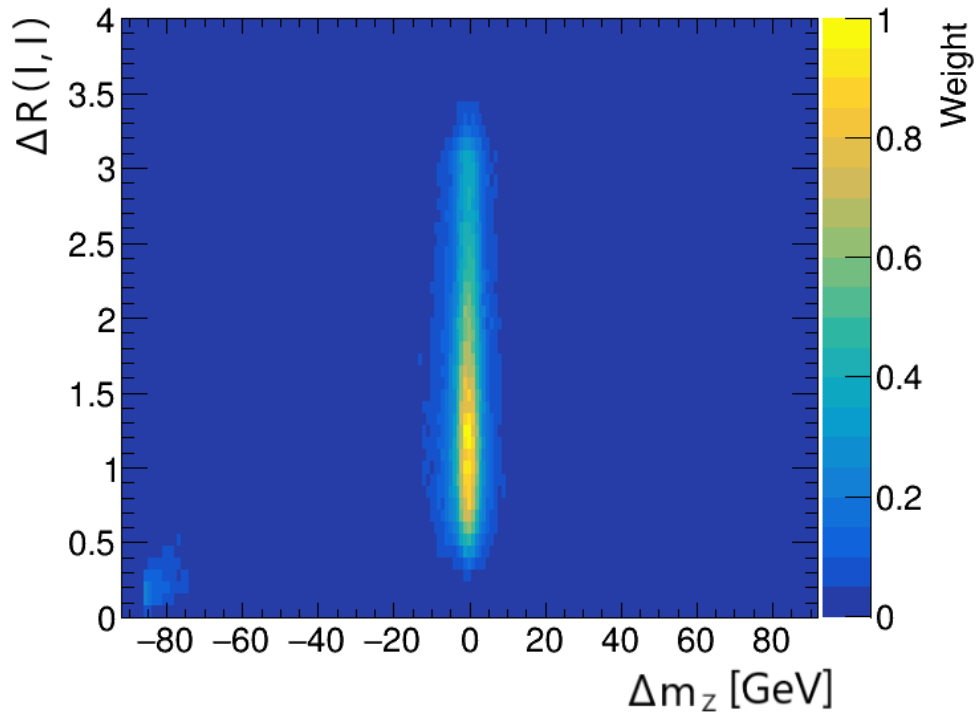
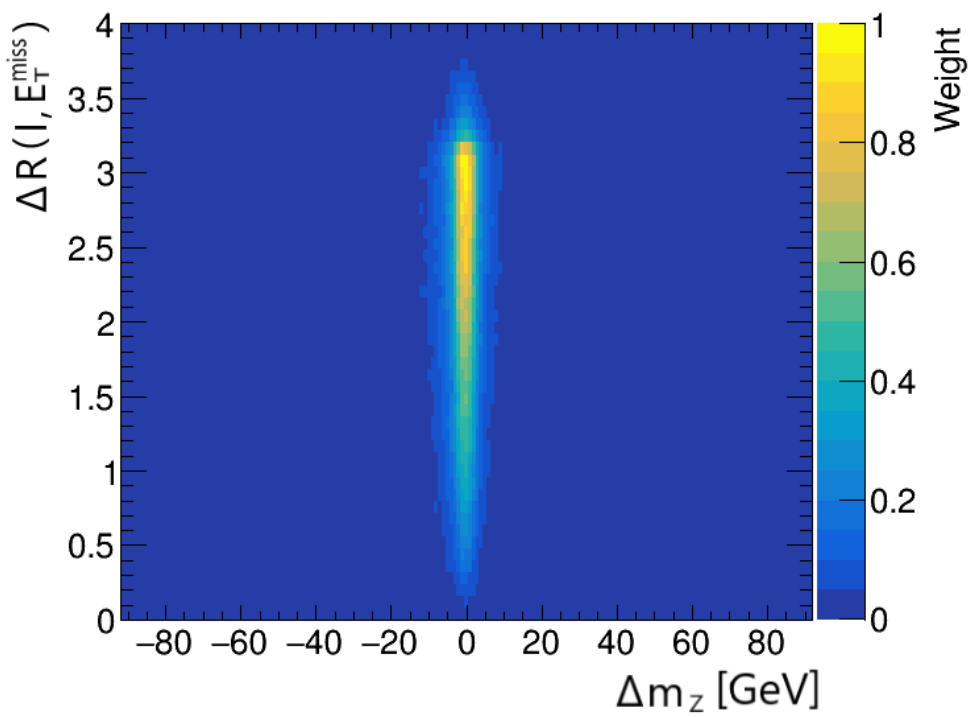
The reference histogram of the  $\Delta m_Z$  variable in figure 6.14 shows a sharp peak at  $\Delta m_Z$  values of zero with a, in comparison, very small bump corresponding to  $m_{\ell\ell}$  values of almost zero or rather  $\Delta m_Z \approx -m_Z$ . The width of the main peak of around 20 GeV from  $\Delta m_Z \approx -10$  GeV to  $\Delta m_Z \approx +10$  GeV corresponds accurately to the mass window requirement from tables 5.3 and 5.4.

For reference histograms 6.15 and 6.16 we see very broad distributions over the whole  $\Delta R$  spectrum with peaks at  $\Delta R(\ell, \ell) \approx 1$  and  $\Delta R(\ell, E_T^{miss}) \approx 3$ , respectively.

### 6.4.2 2D reference histograms

The 1D reference versions are now combined into 2D reference histograms by adding up entries for bins, which are assigned a specific interval of one variable while another variable is also within a certain range. The different value intervals of both variables occupy either the x- or the y-axis while their entries are counted via color-coding the associated bins according to their respective frequency in relation to the most occupied bin.

As indicated before, the  $\Delta m_Z$  variable will be part of every reference histogram that is presented in the following what, therefore, leaves the two combination options of variables into a two dimensional reference histogram, the 2D  $(\Delta m_Z, \Delta R(\ell, \ell))$ -reference histogram on the one hand and the 2D  $(\Delta m_Z, \Delta R(\ell, E_T^{miss}))$ -reference histogram on the other hand.

Figure 6.17: 2D  $(\Delta m_Z, \Delta R(\ell, \ell))$  reference histogram.Figure 6.18: 2D  $(\Delta m_Z, \Delta R(\ell, E_T^{\text{miss}}))$  reference histogram.

For the 2D reference histograms in figures 6.17 and 6.18, all entries mainly cluster in one area or "island" of value combinations in the center of both plots. These are shaped according to the sharp  $\Delta m_Z$  peak from figure 6.14 in x-direction while the broader  $\Delta R$  distributions, 6.15 and 6.16, stretch the clusters in y-direction. In addition to the main cluster, a small bump from the  $\Delta m_Z$  reference histogram's entries close to the value of  $-m_Z$  is slightly visible in the 2D  $(\Delta m_Z, \Delta R(\ell, \ell))$  reference histogram.

### 6.4.3 3D reference histograms

While on this 2-dimensional piece of paper the visualisation of 2D reference histograms had been possible through indicating the third dimension of entries with color, for a 3D reference histogram this is not easily possible given its actual four dimensions. However, this is only affecting our ability to display them here but not a computer's ability to work with the information stored in the corresponding data. One can imagine the 3D reference histogram to consist of the depiction of a 2D one with the 1D histogram of the remaining variable stuck to it into the paper plane as an extension into a third dimension.

With that said, given our in total three against Z boson decay leptons discriminating variables, we obtain the 3D  $(\Delta m_Z, \Delta R(\ell, \ell), \Delta R(\ell, E_T^{miss}))$ -reference histogram as the only possible option.

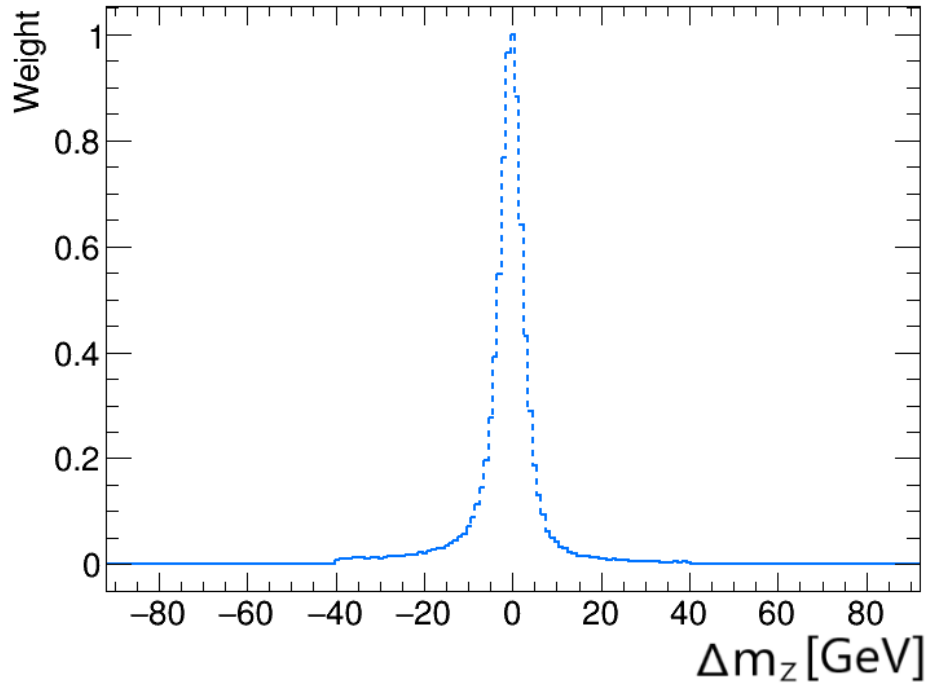
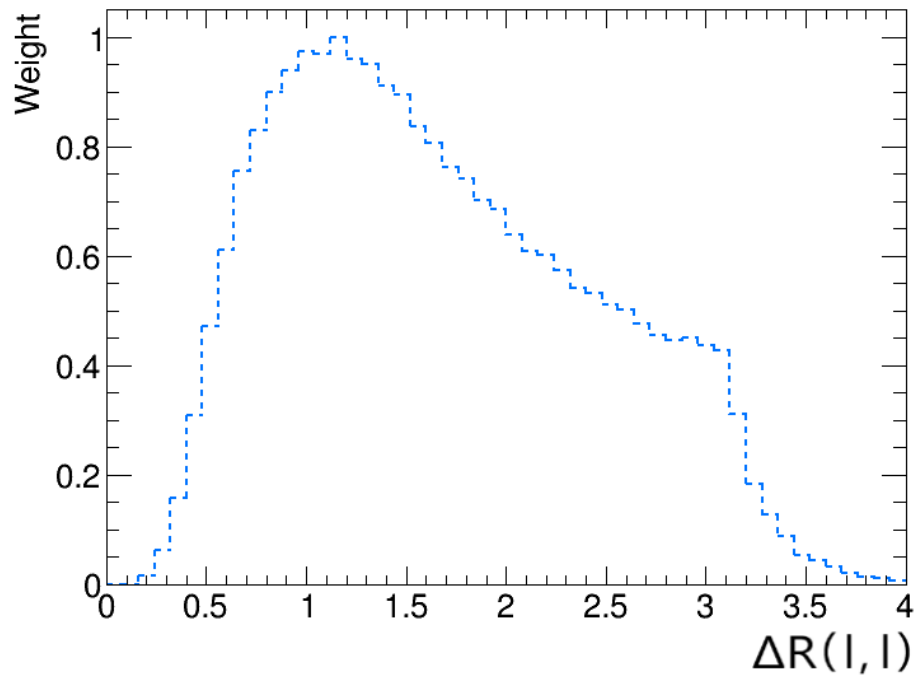
### 6.4.4 Masking

Like indicated in section 4.3, the samples used for this analysis were produced inclusively, meaning the leptonic decay particles of the Z boson occasionally emit high energy photons  $\gamma$ . The effect of that can be spotted easily on a couple of the reference histograms presented before, namely the 1D  $(\Delta m_Z)$  histogram in figure 6.14 and the one for the 2D  $(\Delta m_Z, \Delta R(\ell, \ell))$  method in figure 6.17. With the photon's proper mass of  $m_\gamma = 0$  they are very poorly suited for the reconstruction of the mass of the Z boson once chosen by truth-matching. This happens since their trajectory still resembles the one from the actual leptonic decay particle's trajectories quite closely. To now exclude these contributions of photons, because they are known to not represent processes of events or particles this analysis is designed to include, data-cutting *masks* are put on top of the reference histograms. By that, constraints are put in place for filling the reference histograms, which exclude events containing photon processes of the Z boson's decay particles by requiring the reconstructed mass of the chosen pairs  $m_{\ell\ell}$ , as well as the their  $\Delta R$  value of both particles  $\Delta R(\ell, \ell)$  to fulfil

$$|\Delta m_Z| = |m_{\ell\ell} - m_Z| < 40\text{GeV} \quad \text{and} \quad \Delta R(\ell, \ell) < 4 ,$$

respectively. Thereby the photon contributions are ruled out for every reference histogram leaving us with these following ones, ready for their implementation.

## Masked 1D reference histograms

Figure 6.19: Masked1D ( $\Delta m_Z$ ) reference histogram.Figure 6.20: Masked 1D  $\Delta R(l, l)$  reference histogram.

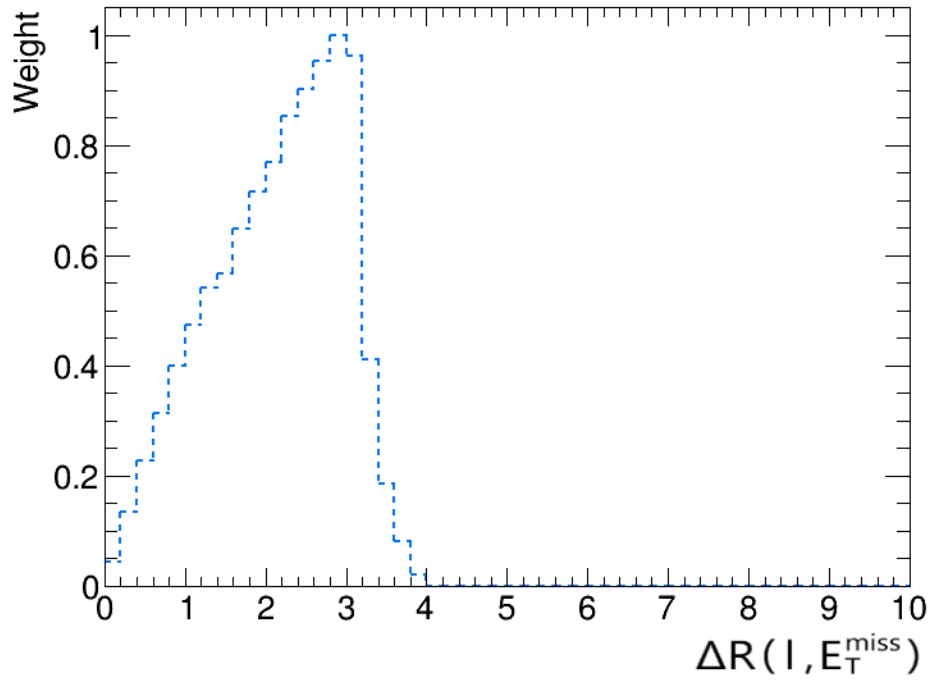
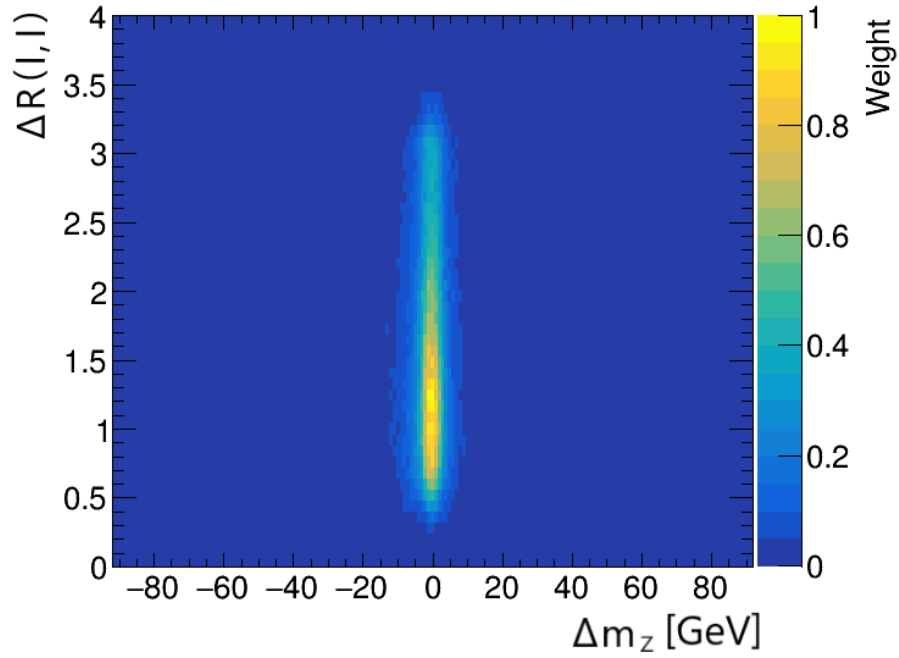
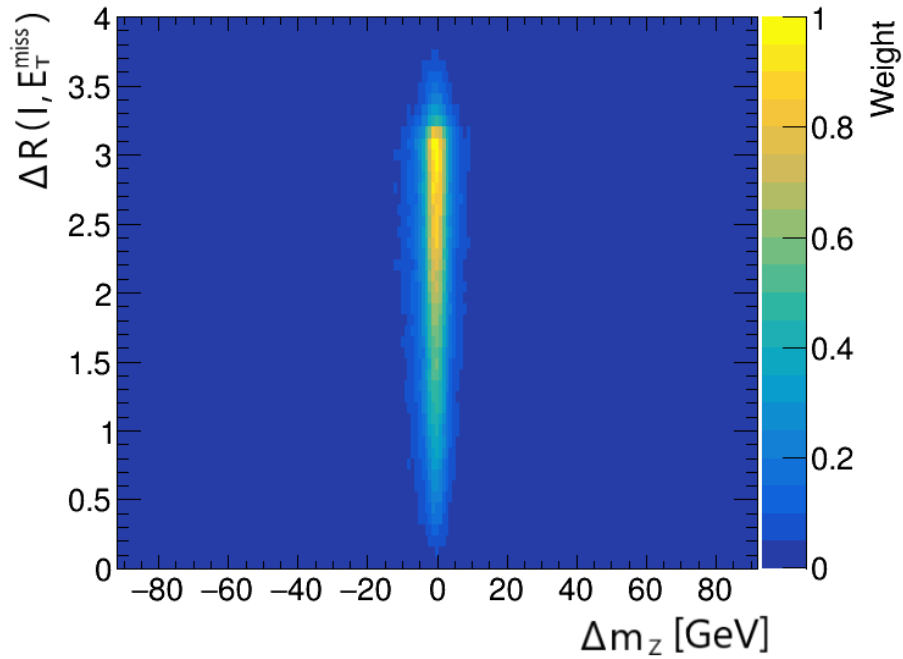


Figure 6.21: Masked 1D  $\Delta R(\ell, E_T^{\text{miss}})$  reference histogram.

While the shapes of the distributions of  $\Delta R(\ell, \ell)$  and  $\Delta R(\ell, E_T^{\text{miss}})$  in the reference histograms in figures 6.20 and 6.21, respectively, stayed almost unchanged, the masked  $\Delta m_Z$  distribution in the reference histogram in figure 6.19 got flattened out at values of  $|\Delta m_Z| \geq 40$  GeV. Therefore, the previously visible small photon induced peak at  $\Delta m_Z \approx -m_Z$  disappeared.

## Masked 2D reference histograms

Figure 6.22: Masked 2D ( $\Delta m_z, \Delta R(\ell, \ell)$ ) reference histogram.Figure 6.23: Masked 2D ( $\Delta m_z, \Delta R(\ell, E_T^{\text{miss}})$ ) reference histogram.

For the masking of the 2D reference histograms the same is to say as before for the 1D reference histograms. While the main clusters of entries in the reference histograms in figures 6.22 and 6.23 stayed identical to their unmasked versions in figures 6.17 and 6.18, respectively, the slightly visible cluster in the bottom left corner of the 2D  $(\Delta m_Z, \Delta R(\ell, \ell))$  reference histogram at very small values for both the  $\Delta m_Z$  and the  $\Delta R(\ell, \ell)$  variable disappeared.

### Masked 3D reference histograms

Of course these changes are also applied on the 3D reference histogram in order for this technique to benefit its efficiencies as well. Therefore, any cluster around very small values for  $\Delta m_Z$  and the  $\Delta R(\ell, \ell)$  will have disappeared in any three dimensional visual depiction.

## 6.5 Evaluation method

The final performance and efficiency evaluation is done for different decay channels separately, as was already shown in figures 6.1 and 6.2 for the efficiencies of the originally implemented Z boson reconstruction method. Given an established pairing between leptons from truth- and detector-level data as well as the reconstructed Z boson obtained by using the masked reference histograms from section 6.4.4 as described in the sections prior to this one, there are still two different ways to evaluate the performance of this process which are briefly introduced and discussed in the following sections.

### 6.5.1 Truth- vs. detector-level evaluation

As already stated in section 4.3.3, the final states can be different for truth- and detector-level data since the detector environment itself can have an impact on them. Decay particles interacting with detector material, among each other or getting their state in any other way changed, results in them not being detected or even existent subsequently. This can also happen to the, otherwise, stable electrons and semi-stable muons traversing the detector to its outer boundaries, therefore, with mean decay lengths  $L$  greater than the ATLAS detector's radius or length. With our binning of the final resulting efficiencies being dependent on the amount, as well as on the configuration of the leptons in the final state, the question of which data level to choose for making this decision arises.

While using detector-level data will almost certainly lead to higher reconstruction efficiencies, since they represent what the detector is ultimately able to detect, and therefore to reconstruct, truth-level data represents the processes which are actually underlying the observed final states and which are responsible for all kinematics. One could argue that when using truth-level data the applied reconstruction algorithm has no chance of correctly finding the Z boson's decay particles when the lepton configuration of an event changes in a particular way, but then again, this is the case for collisions being recorded by real particle detectors and not simulated by Monte Carlo methods. Therefore, when considering, not the disadvantage of the simulated detector but actual particle detectors like ATLAS, where there are no truth information on any event, this argument could be turned around.

This case for truth-level evaluation can be strengthened by looking at the specific example of a three lepton event where the *Z* boson decays via  $Z \rightarrow e^+e^-$  while only one of the *W* bosons decays leptonically via  $W^\pm \rightarrow \mu^+\nu_\mu/\mu^-\bar{\nu}_\mu$ . No matter if there is a muon or an anti-muon in the final state originating from the *W* bosons, there is only one possible *Z* boson to be reconstructed. The detector-level efficiency evaluation would, therefore, yield a 100% efficiency rate for its correct reconstructions, which by itself is unrealistic for any detector. Considering that, when using truth-level data some events could end up in configuration which are not possible to be reconstructed or misleading whenever one of the electrons, in our specific example of  $ee\mu$  events, somehow ends up exchanged for a muon, this draws a more realistic picture of real-world particle physics. This is not to say, that suddenly the efficiency is expected to drop very much since the  $(e^+e^-\mu^\pm)$ -configuration is still a very clean one. The evaluation via truth-level data in this analysis would simply paint a more realistic picture of the *Z* boson reconstruction.

Therefore, truth-level evaluation according to *truth-level data* of the events examined in this analysis is chosen for every efficiency plot in this thesis, including the already in figures 6.1 and 6.2 shown ones for the original ATLAS-CONF-2020-028 [5] method.

## 6.5.2 Uncertainties

Settled for the approach of truth-level evaluation, there are still uncertainties to the obtained efficiencies presented in the following sections that need to be addressed. The errors displayed next to the plots are calculated for each lepton configuration from the efficiencies  $\epsilon_{correct}$  and  $\epsilon_{incorrect}$ , for the fraction of correctly and incorrectly reconstructed *Z* bosons, respectively. The respective errors  $E$  are obtained via

$$\pm E = \pm \left( \frac{\epsilon_{correct} \cdot \epsilon_{incorrect}}{\#events} \right) = \pm \left( \frac{\epsilon_{correct} \cdot (1 - \epsilon_{correct})}{\#events} \right)$$

with  $\epsilon_{incorrect} = 1 - \epsilon_{correct}$ , since the efficiencies of correct and incorrect reconstructions have to add up to 1 or 100%, and the amount of entries in the bin of the specific configuration  $\#events$ . While rounding percentages to the second decimal place, corresponding to the fourth decimal place in the numbers displayed in the efficiency plots, for three lepton events given efficiencies can be taken as accurate as the error is always smaller. However, for four lepton events this leads to an error in the last displayed digit of up to 1 corresponding to an error of  $\pm E = \pm 0.0001 = \pm 0.01\%$ .

## 6.6 Reconstruction efficiencies

For each of the efficiency plots in this section there will be a brief description of features that stand out first, separately for the different 1D, 2D and 3D reference methods, and secondly a short comparison is drawn between the initial method and the performance of the respective variable. A more in-detail description and comparisons of the best performing methods of each *X*-dimensional strategy is given in section 6.6.4 at the end of this chapter.

### 6.6.1 1D reference histogram efficiencies

#### 1D $\Delta m_Z$ method efficiencies

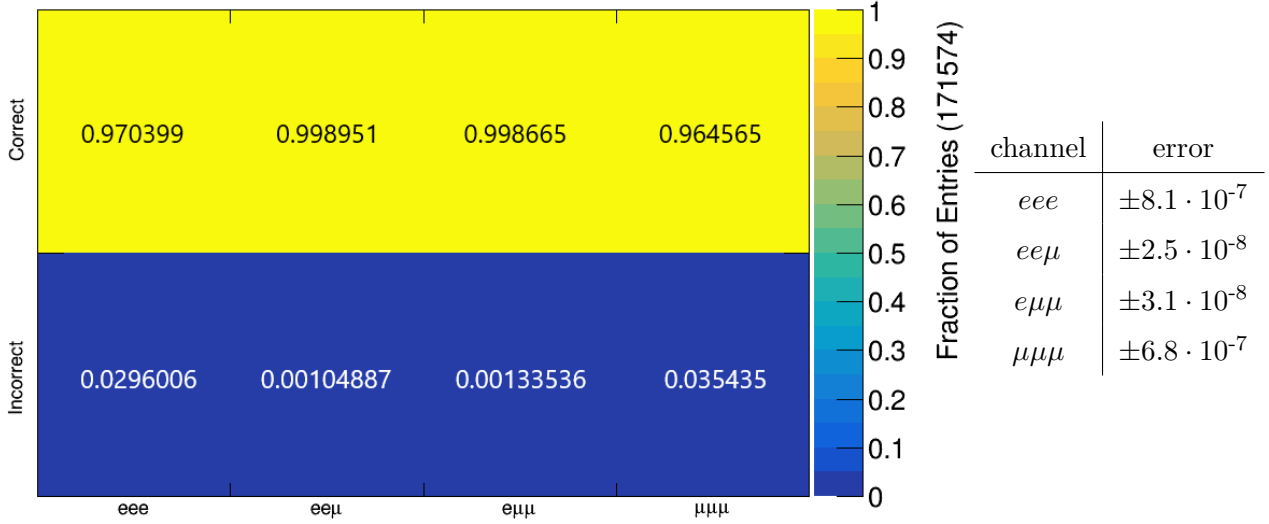


Figure 6.24: Z boson reconstruction efficiencies of the 1D ( $\Delta m_Z$ ) reference histogram for three lepton events.

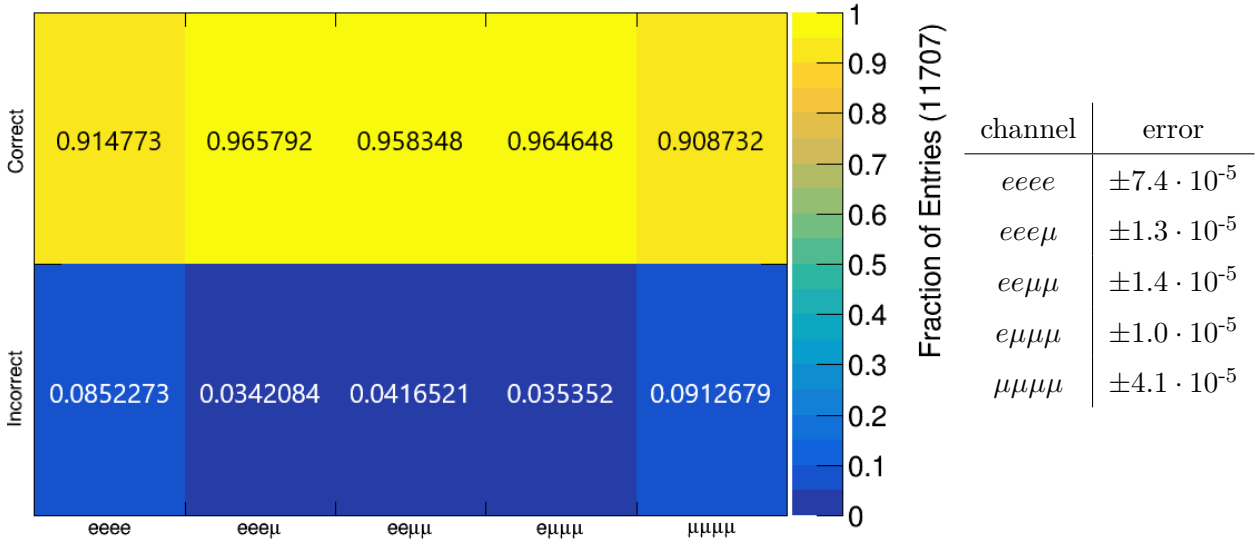


Figure 6.25: Z boson reconstruction efficiencies of the 1D ( $\Delta m_Z$ ) reference histogram for four lepton events.

As can be seen in figures 6.24 and 6.25, the method of a one dimensional  $\Delta m_Z$  reference plot yields a higher efficiency than the original method in four regions, while being less efficient in two. The remaining three final state configuration regions are of the exact same efficiency for both methods. An additional interpretation of this observation is given in section 6.6.4. This proves the  $\Delta m_Z$  to be a very good variable for the Z boson decay particle search and endorses the decision to include it into every multi-dimensional reference histogram.

### 1D $\Delta R(\ell, \ell)$ method efficiencies

While the performance of the 1D ( $\Delta R(\ell, \ell)$ ) method in the  $ee\mu$  and  $e\mu\mu$  bins is still high due to the unambiguity of the reconstruction in these decay channels, although performing worse than with the original method, the efficiencies in the remaining lepton configuration channels drops significantly. This was to be expected as the truth-testing plots for this variable in figures 6.5 and 6.6 suggested only a very weak discrimination of Z boson decay leptons. With higher combinatoric effects in the four lepton channels the performance decreases more significantly there, reaching a worse than 50% performance efficiency in the four lepton all-same-flavour ones.

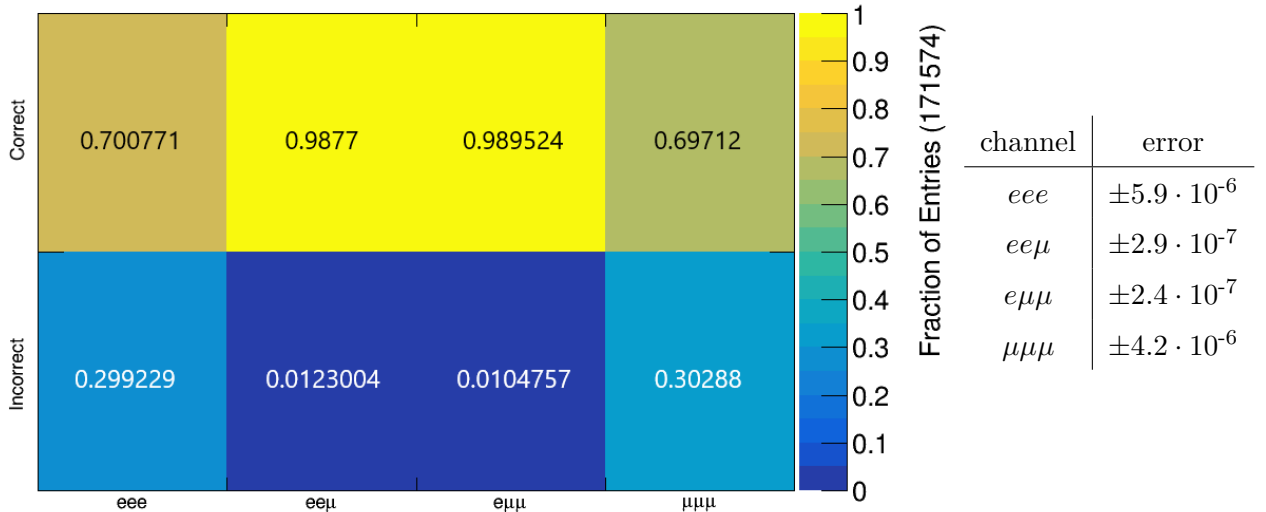


Figure 6.26: Z boson reconstruction efficiencies of the 1D ( $\Delta R(\ell, \ell)$ ) reference histogram for three lepton events.

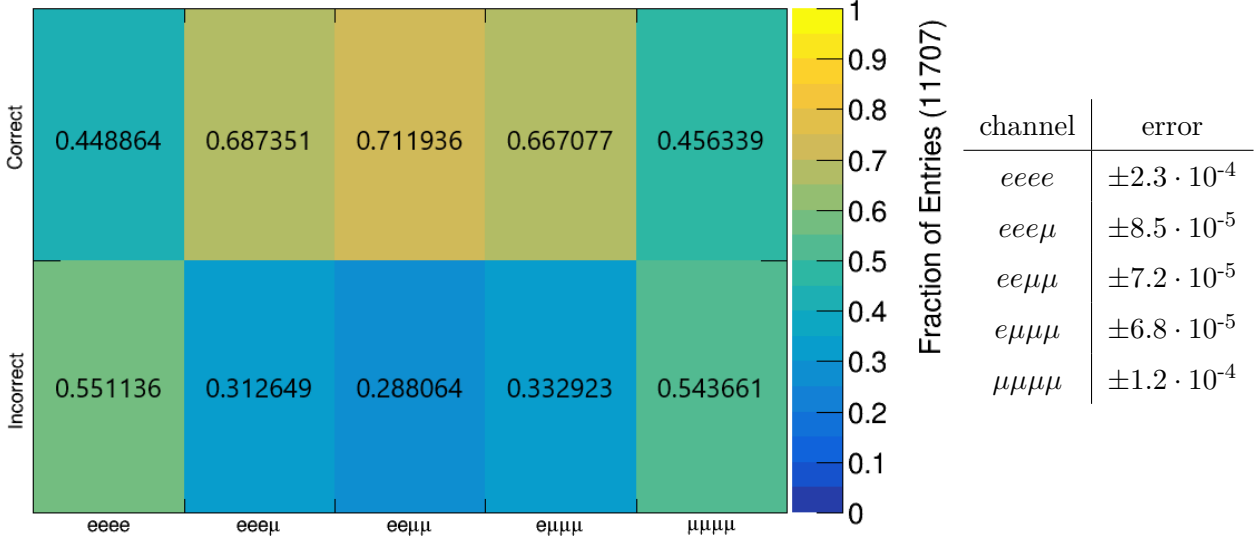


Figure 6.27: Z boson reconstruction efficiencies of the 1D ( $\Delta R(\ell, \ell)$ ) reference histogram for four lepton events.

### 1D $\Delta R(\ell, E_T^{miss})$ method efficiencies

With its discriminative power predicted to be weaker than the one of the previously discussed 1D ( $\Delta R(\ell, \ell)$ ) method, the 1D ( $\Delta R(\ell, E_T^{miss})$ ) reference histogram method was bound to perform poorly which is validated by the efficiency plots in figures 6.28 and 6.29. Making matters even worse for this variable's performance is the clear difference in shape, visible when comparing the corresponding reference histogram in figure 6.16 with the initial truth-level testing plots for the variable in figures 6.8 and 6.9. One notes that the  $\Delta R$ -distribution of the correctly matched detector-level Z boson decay particles and the detector-level  $E_T^{miss}$  value resembles more closely the shape of the distribution of the truth-level W boson decay leptons than the ones of the actual Z boson decay leptons. This could be caused by the imperfections in the missing transverse energy of the detector-level data triggered themselves by different interactions of the decay particles of any single event.

The effects on the performance of any reference histogram which includes the  $\Delta R(\ell, E_T^{miss})$ , namely the 2D- and the 3D- reference histograms, could, therefore, not only be negligible but also negative.

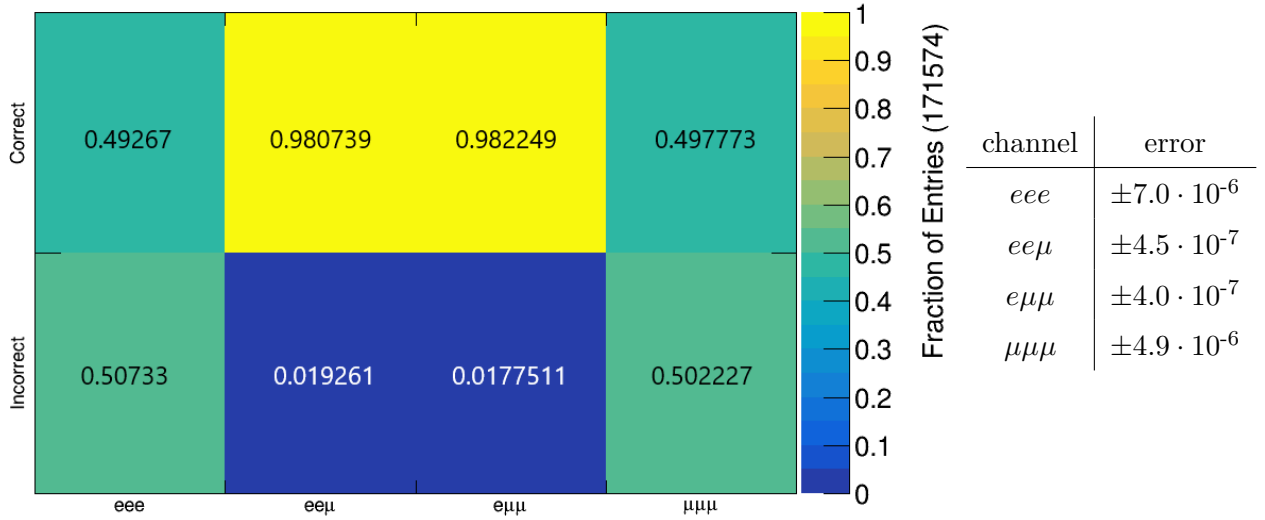


Figure 6.28: Z boson reconstruction efficiencies of the 1D ( $\Delta R(\ell, E_T^{miss})$ ) reference histogram for three lepton events.

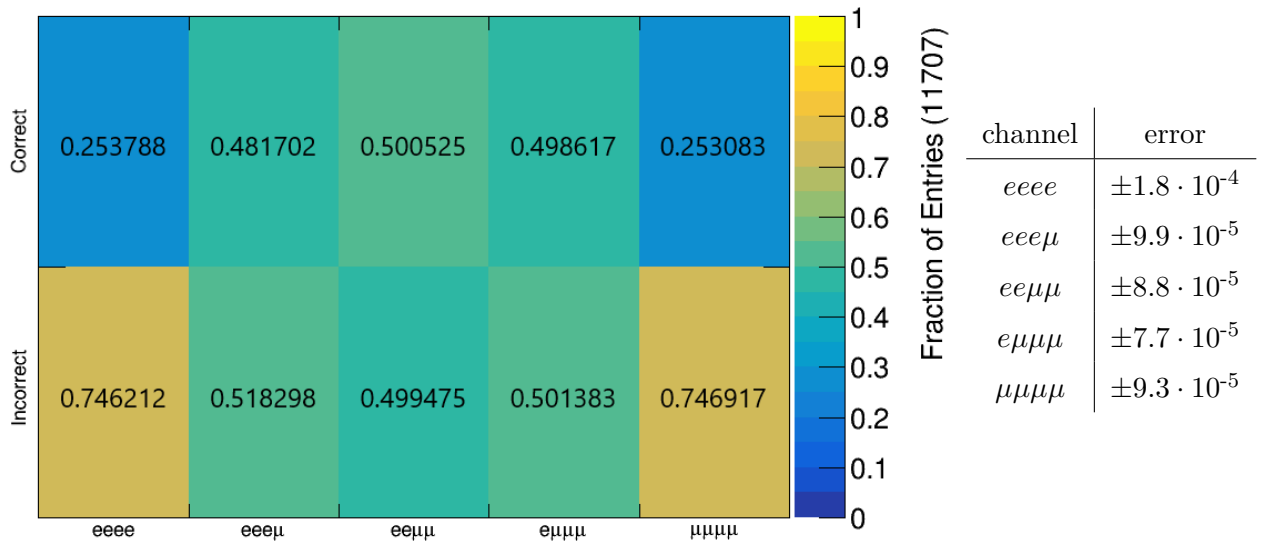


Figure 6.29: Z boson reconstruction efficiencies of the 1D ( $\Delta R(\ell, E_T^{miss})$ ) reference histogram for four lepton events.

## 6.6.2 2D reference histogram efficiencies

### 2D $\Delta m_Z, \Delta R(\ell, \ell)$ method efficiencies

Combining the two best performing 1D methods into a single one, the 2D ( $\Delta m_Z, \Delta R(\ell, \ell)$ ) reference histogram method satisfies the expectations this combination brings with it. With improved efficiencies in every bin for both three and four lepton events in comparison to the method originally used in [5], it becomes the first candidate to be employed instead of this already implemented method. A closer look into the performance of this variable follows in section 6.6.4.

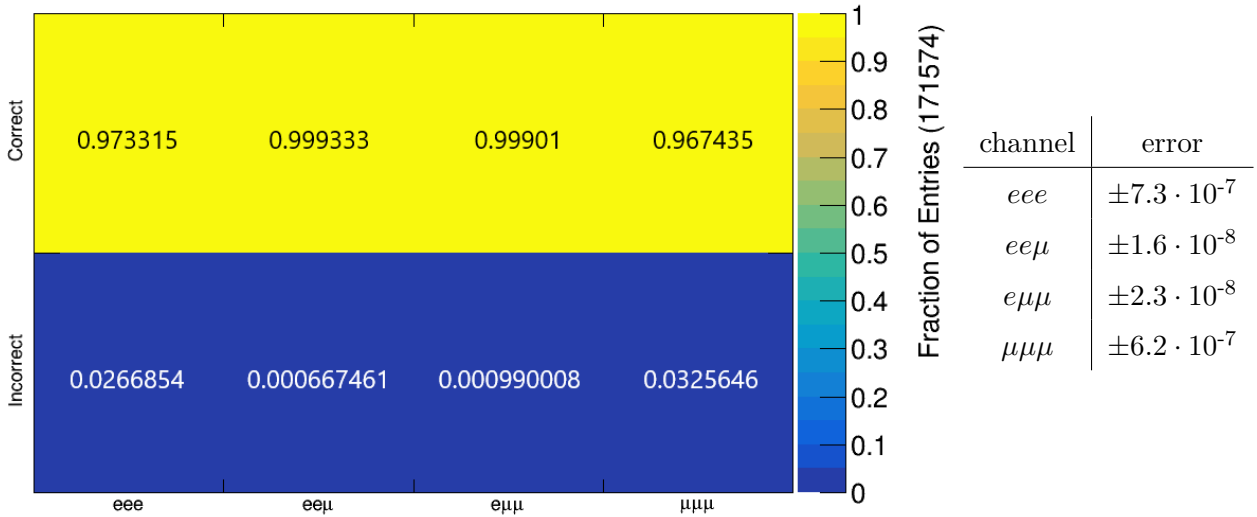


Figure 6.30:  $Z$  boson reconstruction efficiencies of the 2D ( $\Delta m_Z, \Delta R(\ell, \ell)$ ) reference histogram for three lepton events.

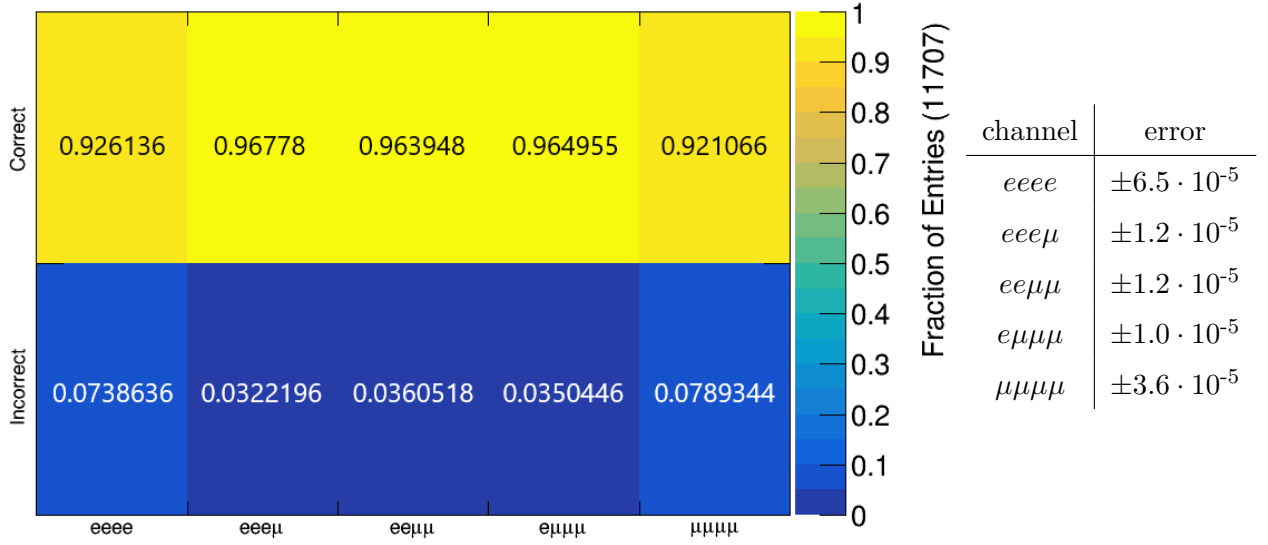


Figure 6.31: Z boson reconstruction efficiencies of the 2D  $(\Delta m_Z, \Delta R(\ell, \ell))$  reference histogram for four lepton events.

### 2D $\Delta m_Z, \Delta R(\ell, E_T^{miss})$ method efficiencies

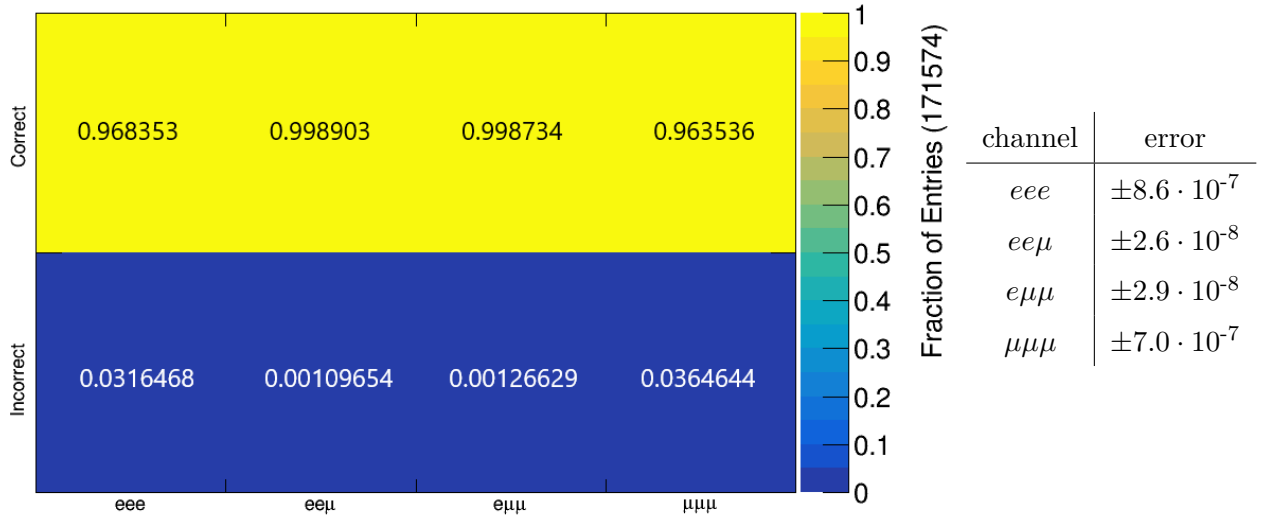


Figure 6.32: Z boson reconstruction efficiencies of the 2D  $(\Delta m_Z, \Delta R(\ell, E_T^{miss}))$  reference histogram for three lepton events.

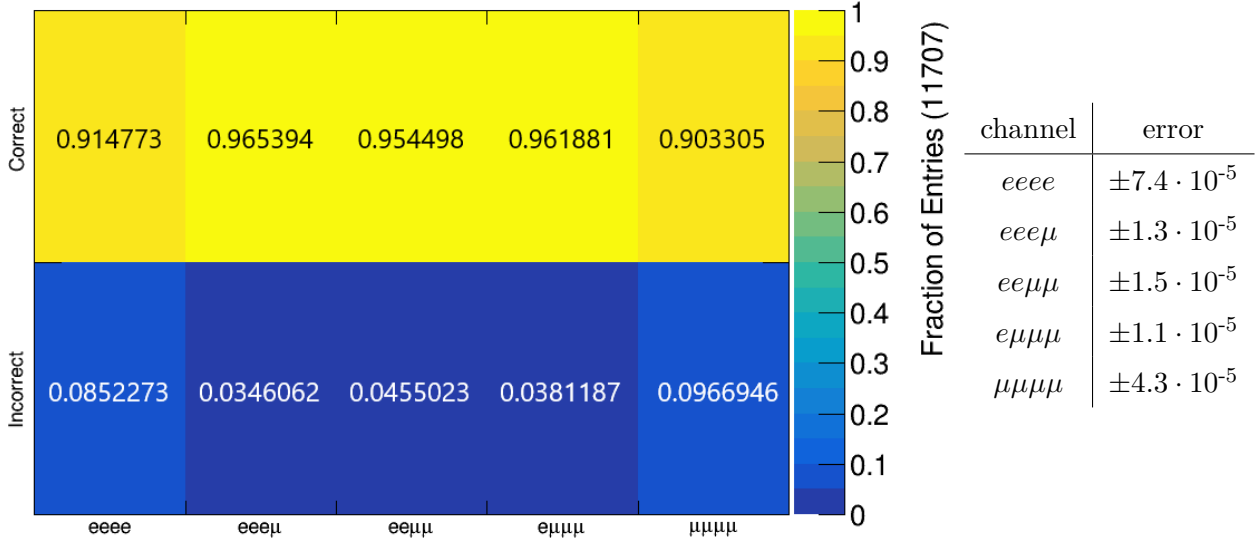


Figure 6.33:  $Z$  boson reconstruction efficiencies of the 2D  $(\Delta m_Z, \Delta R(\ell, E_T^{miss}))$  reference histogram for four lepton events.

As speculated in section A.2 on the 1D reference histogram performance of the  $\Delta R(\ell, E_T^{miss})$  variable and validated by the efficiency plots in figures 6.32 and 6.33, the 2D  $(\Delta m_Z, \Delta R(\ell, E_T^{miss}))$  reference histogram method is inferior to the initial method for every lepton configuration except the  $eeee$  one, the efficiency of which is exactly the same as for the original method. This overall decrease in efficiency of the 2D  $(\Delta m_Z, \Delta R(\ell, E_T^{miss}))$  reference histogram method in comparison to, not only the original efficiency but also to the 1D  $(\Delta m_Z)$  reference histogram method, strongly suggests that the 3D method's performance will drop as well through the introduction of the  $\Delta R(\ell, E_T^{miss})$  variable into the 2D  $(\Delta m_Z, \Delta R(\ell, \ell))$  method, in comparison to the method of the latter one on its own.

### 6.6.3 3D reference histogram efficiencies

#### 3D $\Delta m_Z, \Delta R(\ell, \ell), \Delta R(\ell, E_T^{miss})$ method efficiencies

Seen in the context of the poor performances of reference histograms which include the  $\Delta R(\ell, E_T^{miss})$  variable, the 3D  $(\Delta m_Z, \Delta R(\ell, \ell), \Delta R(\ell, E_T^{miss}))$  reference histogram method's performance, depicted in figures 6.34 and 6.35, falls short of the efficiencies reached by the 2D  $(\Delta m_Z, \Delta R(\ell, E_T^{miss}))$  method due to the negative influence of the  $\Delta R(\ell, E_T^{miss})$  variable. However, its performance still is, in comparison to the initial method, superior for seven out of the nine  $t\bar{t}Z$  decay paths analysed in this study, with the  $eee\mu$  and the  $e\mu\mu\mu$  configurations being the exceptions.

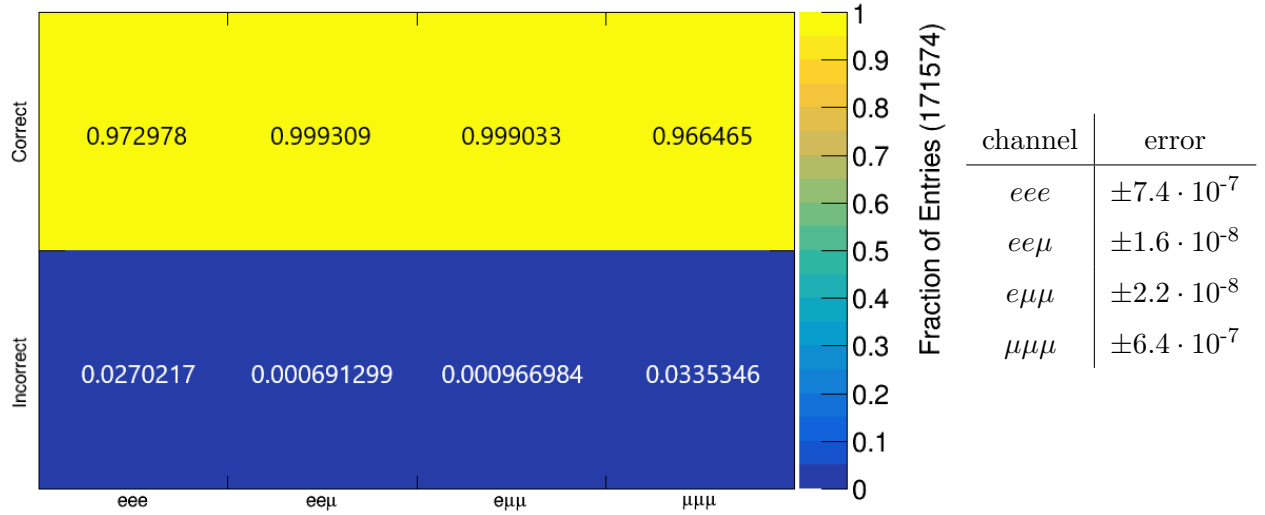


Figure 6.34: Z boson reconstruction efficiencies of the 3D ( $\Delta m_Z, \Delta R(\ell, \ell), \Delta R(\ell, E_T^{miss})$ ) reference histogram for three lepton events.

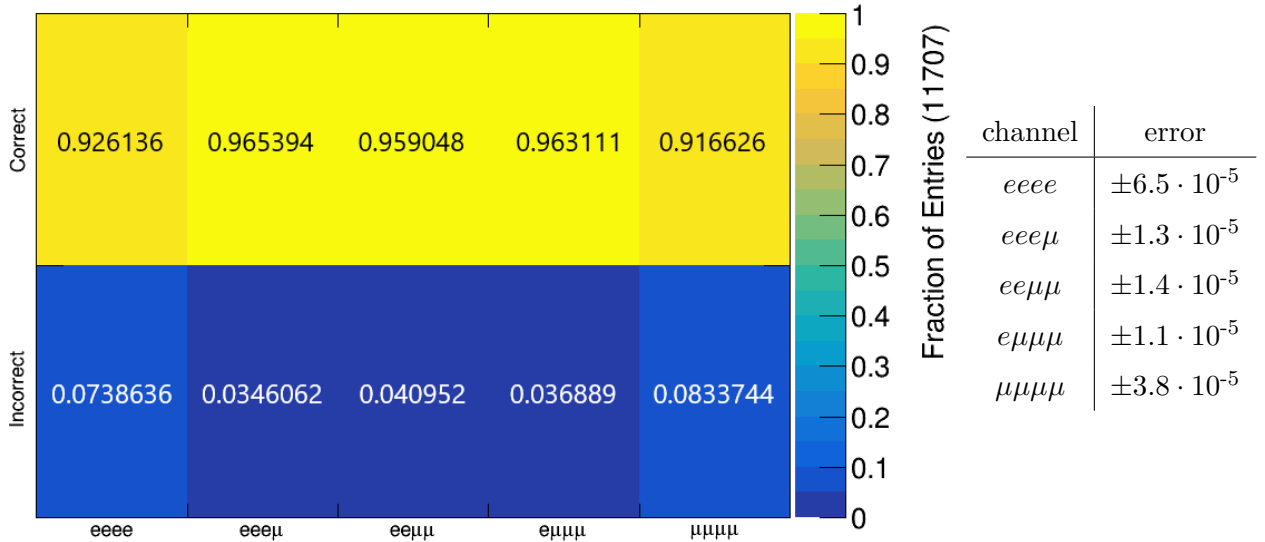


Figure 6.35: Z boson reconstruction efficiencies of the 3D ( $\Delta m_Z, \Delta R(\ell, \ell), \Delta R(\ell, E_T^{miss})$ ) reference histogram for four lepton events.

### 6.6.4 Method comparison and efficiency summary

Given the data from the efficiency plots in section 6.6 so far, we have seen that the overall best performing method of the tested ones was the 2D ( $\Delta m_Z, \Delta R(\ell, \ell)$ ) reference histogram method. To put its performance more detailed into perspective with the currently employed method in the ATLAS-CONF-2020-028 [5] analysis, the efficiencies for each bin of both methods are listed side by side in table 6.1 with the respective change in efficiency from the initial to the new one next to them, which will be commented on later in this section.

For an insight in the performance of the different individual signal region, the efficiencies of each one for every final state lepton configuration is presented in corresponding tables. Additionally, for the 2D ( $\Delta m_Z, \Delta R(\ell, \ell)$ ) method a comparison is drawn between the efficiencies obtained through employment of the three lepton signal regions from table 5.3, like in all results shown at this point, and those resulting from the use of older ones, without the use of PCBT, defined in the appendix in table A.1.

After that, the efficiencies, again with the most recent set of three lepton signal regions, of the 1D ( $\Delta m_Z$ ) method and the 3D ( $\Delta m_Z, \Delta R(\ell, \ell), \Delta R(\ell, E_T^{miss})$ ) method, as the best performing implementations of 1D and 3D histograms, respectively, are revisited to summarize some key take-aways.

| signal region | initial method's efficiency | 2D ( $\Delta m_Z, \Delta R(\ell, \ell)$ ) method's efficiency | efficiency change |
|---------------|-----------------------------|---|-------------------|
| 3L            | $eee$                       | 97.03%  | ↗ 0.30%           |
|               | $eem$                       | 99.89%  | ↗ 0.04%           |
|               | $e\mu\mu$                   | 99.88%  | ↗ 0.02%           |
|               | $\mu\mu\mu$                 | 96.44%  | ↗ 0.30%           |
| 4L            | $eeee$                      | 91.48%  | ↗ 1.13%           |
|               | $eeem$                      | 96.66%  | ↗ 0.12%           |
|               | $eem\mu$                    | 95.62%  | ↗ 0.77%           |
|               | $e\mu\mu\mu$                | 96.46%  | ↗ 0.04%           |
|               | $\mu\mu\mu\mu$              | 90.87%  | ↗ 1.24%           |

Table 6.1: Comparison between the initial and the new 2D ( $\Delta m_Z, \Delta R(\ell, \ell)$ ) method for Z boson reconstruction.

The overall best performing 2D  $(\Delta m_Z, \Delta R(\ell, \ell))$  reference histogram method is superior to the previous implemented calculating method in every lepton configuration bin tested as has been visualized in table 6.1. With that said, the more combinations a bin offers for distinct Z boson candidates to be reconstructed, and therefore the higher the combinatoric effect of a lepton configuration is, the greater the absolute improvement of the correct Z boson reconstruction by the new method will be, seems to be a valid statement.

For three lepton events, where there are generally less possibilities for OSSF pairs for the Z boson candidate to be chosen from, the 2D  $(\Delta m_Z, \Delta R(\ell, \ell))$  reference histogram method has only very subtle, but still positive effects on the reconstruction efficiency percentages. Especially in the bins of actually unambiguous choice in case truth- and detector-level final states match, namely the  $ee\mu$  and the  $e\mu\mu$  bins, the absolute improvements of only five and two hundreds of a percent, respectively, are very small. In the all-same-flavour channels, with their two different Z boson reconstruction choices, the absolute efficiency improvements are greater with 0.30% for both configurations,  $eee$  and  $ee\mu$ . Considering that the efficiencies were already beyond 99% for the mixed configuration channels and beyond 95% for the all-same-flavour ones in the initial reconstruction method, even these seemingly minuscule increases are not negligible when looked at from the perspective of incorrectly reconstructed Z bosons. Percentages to the relative improvement of these can be found in table 6.2. Here, the all-same-flavour efficiency improvements closed the gaps in both bins between the initial reconstruction efficiency and a perfectly accurate method by a bit more than 8% and 10%. For the mixed-flavour lepton configurations this efficiency gap to perfect reconstruction was shortened by 16% in the case of  $e\mu\mu$  final states and even 36% for  $ee\mu$  configurations.

| signal region | relative improvement for incorrect reconstructions | $\left(1 - \frac{(\epsilon_{incorrect})_{initial}}{(\epsilon_{incorrect})_{2D(\Delta m_Z, \Delta R(\ell, \ell))}}\right)$ |
|---------------|--|---|
| 3L            | $eee$  | ↘ 10.10%  |
|               | $ee\mu$  | ↘ 36.36%  |
|               | $e\mu\mu$  | ↘ 16.67%  |
|               | $\mu\mu\mu$  | ↘ 8.20%   |
| 4L            | $eeee$   | ↘ 13.26%  |
|               | $eee\mu$   | ↘ 3.59%   |
|               | $ee\mu\mu$   | ↘ 17.58%  |
|               | $e\mu\mu\mu$                                       | ↘ 1.13%   |
|               | $\mu\mu\mu\mu$                                     | ↘ 13.58%  |

Table 6.2: Comparison between the initial and the new1D  $(\Delta m_Z)$  method for Z boson reconstruction.

In the four lepton final state regions the all-same-flavour channels experienced the greatest change in absolute values as well. Already at efficiencies beyond 90%,  $eeee$  and  $\mu\mu\mu\mu$  configurations gained 1.13% and 1.24% in  $Z$  boson reconstruction efficiency, respectively. Calculating again the percentage of the relative decrease in the number of incorrectly reconstructed  $Z$  bosons, these gains in absolute efficiency correspond to a 13% decrease for both all-same-flavour configurations in that regard. Close to that in absolute terms, and even ahead in relative terms, is the maximally flavour-mixed  $ee\mu\mu$  final states channel with an absolute increase of 0.77% corresponding to a 17.5% reduction of the entries of incorrect reconstruction. The smallest improvement in both ways is experienced by the two remaining configuration channels. These are the  $eee\mu$  channel with an absolute percentage increase of 0.12% and the  $e\mu\mu\mu$  channel with a 0.04% one, which correspond to about 3.5% and 1.1% of the events with incorrectly reconstructed  $Z$  bosons to be now reconstructed correctly.

In order to gain an even deeper insight into what kinds of events tend to be incorrectly reconstructed for each lepton configuration, one can look at the individual signal regions' performances, depicted in tables 6.3 and 6.4 for three and four lepton events, respectively, while still considering the 2D  $(\Delta m_Z, \Delta R(\ell, \ell))$  method. The individual signal region performances of all other methods can be found in the appendix in section A.2.

For the trilepton signal regions peaks in performances for the different configurations are distributed very uniformly across them, with each performing best for at least one.

In the four lepton regions the effect of the differences in truth- and detector-level data becomes clear. Lepton combinations which normally should not be included in the respective signal region in the first place based on their truth-level state are included on detector-level anyhow, based on the effects the bin migration matrix in figure 5.2 depicts. However, since all of these occurrences besides the  $4l$ - $DF$ - $1b$ 's efficiency for  $eeee$  configurations are above 90% this indicates that even in these cases the method is fairly robust with some of them performing with 100% efficiency even in these cases. Nevertheless, these whole integer values of 100% are probably also due to the small amount of events passing the signal regions and event cuts despite drastic changes between truth- and detector-level final states.

| signal region | $3l$ - $Z$ - $1b4j$ -PCBT<br>efficiency | $3l$ - $Z$ - $2b3j$ -PCBT<br>efficiency | $3l$ - $Z$ - $2b3j$ -diff<br>efficiency |
|---------------|---|---|---|
| 3L            | $eee$                                   | 97.39%                                  | 97.20%                                  |
|               | $ee\mu$                                 | 99.90%                                  | 99.96%                                  |
|               | $e\mu\mu$                               | 99.89%                                  | 99.92%                                  |
|               | $\mu\mu\mu$                             | 96.64%                                  | 96.78%                                  |

Table 6.3: Efficiencies of the 2D  $(\Delta m_Z, \Delta R(\ell, \ell))$  method for correct  $Z$  boson reconstruction in different three lepton signal regions.

| signal region | $4l$ -DF-1b<br>efficiency | $4l$ -DF-2b<br>efficiency | $4l$ -SF-1b<br>efficiency | $4l$ -SF-2b<br>efficiency |        |
|---------------|---------------------------|---------------------------|---------------------------|---------------------------|--------|
| 4L            | $eeee$                    | 84.62%                    | 100%                      | 93.53%                    | 91.24% |
|               | $ee\mu$                   | 97.73%                    | 95.00%                    | 96.74%                    | 97.58% |
|               | $e\mu\mu$                 | 100%                      | 100%                      | 96.29%                    | 96.84% |
|               | $e\mu\mu\mu$              | 93.15%                    | 92.59%                    | 96.83%                    | 97.29% |
|               | $\mu\mu\mu\mu$            | 91.49%                    | 92.86%                    | 92.87%                    | 91.31% |

Table 6.4: Efficiencies of the 2D ( $\Delta m_Z, \Delta R(\ell, \ell)$ ) method for correct Z boson reconstruction in different four lepton signal regions.

To put the performances of especially the three lepton signal regions further into perspective, older "inclusive" signal regions used in previous iterations of the ATLAS-CONF-2020-028 [5] analysis were implemented in this analysis as well, according to their definitions in table A.1. This was done in order to investigate the effect that this switch had on the three lepton reconstruction efficiencies, from the old the old trilepton regions not using pseudo-continuous b-tagging to the current ones that do. These in combination with the differential  $3l$ -Z-2b3j-diff signal region yield the efficiencies depicted in figure 6.36.

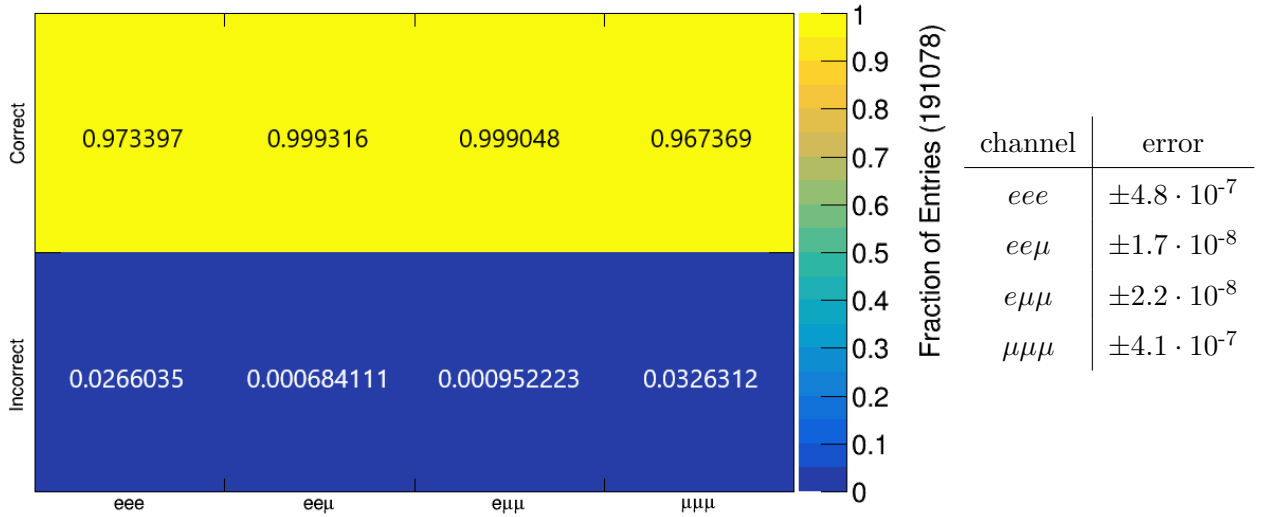


Figure 6.36: Z boson reconstruction efficiencies of the 2D ( $\Delta m_Z, \Delta R(\ell, \ell)$ ) method for three lepton events while old three lepton signal regions apply.

| signal region |             | 2D ( $\Delta m_Z, \Delta R(\ell, \ell)$ )<br>method's efficiency<br>with old SRs | 2D ( $\Delta m_Z, \Delta R(\ell, \ell)$ )<br>method's efficiency<br>with new SRs | efficiency<br>change |
|---------------|-------------|--|--|----------------------|
| 3L            | $eee$       | 97.34%   | 97.33%   | ↘ 0.01%              |
|               | $ee\mu$     | 99.93%   | 99.93%   | ↗ 0.00%              |
|               | $e\mu\mu$   | 99.88%   | 99.90%   | ↘ 0.00%              |
|               | $\mu\mu\mu$ | 96.74%   | 96.74%   | ↗ 0.00%              |

Table 6.5: Comparison between the 2D ( $\Delta m_Z, \Delta R(\ell, \ell)$ ) method's efficiency for Z boson reconstruction with new and old three lepton signal regions.

This exchange of signal regions caused not a lot of change in the efficiencies, at least given the 2D ( $\Delta m_Z, \Delta R(\ell, \ell)$ ) method is employed as listed in table 6.5. With changes of less than 0.01% in absolute terms for every lepton configuration, twice in favour of either signal region set, the overall efficiency is virtually identical while the newer set uses 3 signal regions versus four in the older one.

The individual performances of the older three lepton signal regions listed in table 6.6, therefore, display an equally balanced picture of performances. Lepton-configuration-wise the best performing signal region is always on the side of the old ones, nevertheless, comparisons between distinct signal regions are not quite meaningful since they cover different ranges of events. The equal overall performance is an example for that.

| signal region |             | $3l-Z-2b3j$<br>efficiency | $3l-Z-1b4j$<br>efficiency | $3l-Z-2b4j$<br>efficiency |
|---------------|-------------|---------------------------|---------------------------|---------------------------|
| 3L            | $eee$       | 97.15%                    | 97.31%                    | 97.40%                    |
|               | $ee\mu$     | 99.97%                    | 99.91%                    | 99.94%                    |
|               | $e\mu\mu$   | 99.81%                    | 99.90%                    | 99.93%                    |
|               | $\mu\mu\mu$ | 96.69%                    | 96.62%                    | 96.81%                    |

Table 6.6: Efficiencies of the 2D ( $\Delta m_Z, \Delta R(\ell, \ell)$ ) method for correct Z boson reconstruction in the old three lepton signal regions.

### Best performing 1D and 3D methods

With the 2D ( $\Delta m_Z, \Delta R(\ell, \ell)$ ) method as the suggested replacement method for the ATLAS-CONF-2020-028 analysis [5], it can still be interesting to examine the best performing 1D reference histogram method and the single 3D method, namely the 1D ( $\Delta m_Z$ ) method and the 3D ( $\Delta m_Z, \Delta R(\ell, \ell), \Delta R(\ell, E_T^{miss})$ ) method, respectively, more closely for the understanding of the reference histogram method in general.

Starting with the 1D ( $\Delta m_Z$ ) method it can be seen in table 6.7 that four out of nine possible lepton configurations experienced an increase in reconstruction efficiency while only two drop in that same regard. The overall net-gain, therefore, in absolute efficiency is positive. This observation is very important in the context of comparing the initially used method of simply calculating a weight based on the event's own information and the presented reference histogram approach based on truth-matching. The slight improvement of efficiencies for a couple of lepton configurations, therefore, shows that the newly implemented Z boson reconstruction method is not inferior compared to the originally used method, but also has a slight advantage over it in some cases.

| signal region | initial method's efficiency | 1D ( $\Delta m_Z$ ) method's efficiency | efficiency change |
|---------------|-----------------------------|---|-------------------|
| 3L            | $eee$                       | 97.03%                                  | ↗ 0.01%           |
|               | $ee\mu$                     | 99.89%                                  | ↗ 0.01%           |
|               | $e\mu\mu$                   | 99.88%                                  | ↘ 0.01%           |
|               | $\mu\mu\mu$                 | 96.44%                                  | ↗ 0.02%           |
| 4L            | $eeee$                      | 91.48%                                  | → 0.00%           |
|               | $eee\mu$                    | 96.66%                                  | ↘ 0.08%           |
|               | $ee\mu\mu$                  | 95.62%                                  | ↗ 0.21%           |
|               | $e\mu\mu\mu$                | 96.46%                                  | → 0.00%           |
|               | $\mu\mu\mu\mu$              | 90.87%                                  | → 0.00%           |

Table 6.7: Comparison between the initial and the new 1D ( $\Delta m_Z$ ) method for Z boson reconstruction.

| signal region | initial method's efficiency | 3D ( $\Delta m_Z, \Delta R(\ell, \ell), \Delta R(\ell, E_T^{miss})$ ) method's efficiency | efficiency |
|---------------|-----------------------------|---|------------|
| 3L            | $eee$                       | 97.03%  | ↗ 0.27%    |
|               | $ee\mu$                     | 99.89%  | ↗ 0.04%    |
|               | $e\mu\mu$                   | 99.88%  | ↗ 0.02%    |
|               | $\mu\mu\mu$                 | 96.44%  | ↗ 0.21%    |
| 4L            | $eeee$                      | 91.48%  | ↗ 0.13%    |
|               | $eee\mu$                    | 96.66%  | ↘ 0.12%    |
|               | $ee\mu\mu$                  | 95.62%  | ↗ 0.28%    |
|               | $e\mu\mu\mu$                | 96.46%  | ↘ 0.15%    |
|               | $\mu\mu\mu\mu$              | 90.87%  | ↗ 0.79%    |

Table 6.8: Comparison between the initial and the new 1D ( $\Delta m_Z$ ) method for Z boson reconstruction.

The case of the 3D ( $\Delta m_Z, \Delta R(\ell, \ell), \Delta R(\ell, E_T^{miss})$ ) reference histogram is interesting for reasons focusing on the potential of this reference based method. While performing better in most final lepton state configurations than the original method, it is still outperformed by the 2D ( $\Delta m_Z, \Delta R(\ell, \ell)$ ) method in every tested lepton configuration bin. However, this is almost certainly due to the  $\Delta R(\ell, E_T^{miss})$  variable which is ill-suited for Z boson reconstruction and not due to the introduced extra dimension in general.

Since the reference histograms only help with assigning weights to leptons or lepton pairings, which will always lead to one single suggestion in form of an OSSF lepton pair in the case of the reconstruction of leptonically decaying Z bosons, the sample size does not have to be increased for additional histogram dimensions in order to keep high enough statistics. Potentially, this would only lead to the consideration of more relevant aspects of the event, assuming enough successful signal discriminating variables are found. Furthermore, one would have to cross check whether the employment of new variables hinders the efficiency of the other ones. If for example Z boson leptons can either fit in the bins of maximal weight of one variable or in that of another, but not into both at the same time, the consequence could be a relatively low weight in total. Whether this kind of over-defining or -restricting takes place for simultaneously investigated variables, which do not have obvious drawbacks like that, can not be said with certainty at this point. Otherwise there should technically be no disadvantages from additional dimensions in the used reference histograms while using Z boson decay particle discriminating variables.

## 7 | Conclusion

In  $t\bar{t}Z$  analyses the reconstruction of events with three or four leptons in the final state is often made more difficult through different possibilities given for the assignment of the leptons to the leptonically decaying  $Z$  boson. In order to improve the reconstruction efficiency of these respective  $Z$  bosons despite the combinatoric effects, especially for the ATLAS  $t\bar{t}Z$  group's ATLAS-CONF-2020-028 analysis [5] focused on tri- and tetraleptonic final states, a truth-matching based reference histogram method was investigated and tested in this analysis. Here, Monte Carlo simulation samples of  $t\bar{t}Z$  events with leptonically decaying  $Z$  bosons have been used, which were scaled to an integrated luminosity of  $66 \text{ fb}^{-1}$  corresponding to the 2018 ATLAS data taking during LHC Run-2 at center-of-mass energy of  $\sqrt{s} = 13 \text{ TeV}$ . First, a set of variables has been tested for their individual discriminative power against  $Z$  boson decay leptons, needed for the separation of signal and background particles in the  $t\bar{t}Z$  events. Subsequently, reference histograms of one, two and three dimensions have been built from the promising variable candidates, presumably suited for the selection of solely leptons originating from a  $Z$  boson decay, namely  $\Delta m_Z$ ,  $\Delta R(\ell, \ell)$  and  $\Delta R(\ell, E_T^{miss})$ . The data to fill these has been taken from detector-level leptons matched before to the truth-level  $Z$  boson decay particles for which their trajectory was the closest, calculated via  $\Delta R$  values. Thereafter, the detector-level properties of the chosen leptons have been used to calculate the values of the different variables, the resulting distributions of which have been transferred into the reference histograms. Implemented via an interpolation based approach using these newly build reference histograms to assign weights to candidate OSSF pairs for the  $Z$  boson reconstruction, the subsequent reference histogram driven pairing selections, thereafter, have been compared with truth-level data once more to evaluate the performance of the respective method. These efficiencies, then, have been compared among one another, as well as to the efficiency of the method originally implemented in the ATLAS-CONF-2020-028 [5] analysis. In the end this has pointed to the 2D  $(\Delta m_Z, \Delta R(\ell, \ell))$  method for being the best performing one which has manifested in efficiency improvements for every three and four lepton final state configuration compared to the original method, illustrated in figure 6.1. The efficiencies of reference histogram methods including the  $\Delta R(\ell, E_T^{miss})$  distributions of the detector-level  $Z$  boson decay leptons turned out to actually harmed by that inclusion. With the 2D  $(\Delta m_Z, \Delta R(\ell, \ell))$  method in use, the greatest efficiency gains in terms of absolute percentage have been obtained in the all-same-flavour four lepton configuration channels,  $eeee$  and  $\mu\mu\mu\mu$  with 1.13% and 1.24%, respectively. Meanwhile, the greatest relative improvement, in the context of a comparison between the numbers of incorrectly reconstructed

events with the original and the new 2D  $(\Delta m_Z, \Delta R(\ell, \ell))$  method, has been achieved in three lepton events for  $ee\mu$  configurations with 36.36% and in four lepton events for  $ee\mu\mu$  configurations with 17.58% (table 6.2).

Given these results there are a couple of additions suggested for future analysis to look into. First, directly referring to the reference histogram method and assuming further for Z boson reconstruction well suited variables can and will be found, there is strong reason to believe that the 2D  $(\Delta m_Z, \Delta R(\ell, \ell))$  reference histogram method complemented with one or even more of these variables which discriminate against leptons stemming from Z boson decays, performs better. Since its combination with the  $\Delta R(\ell, E_T^{miss})$  variable, forming the 3D  $(\Delta m_Z, \Delta R(\ell, \ell), \Delta R(\ell, E_T^{miss}))$  method, decreased the overall performance of the resulting method because of the performance-harming  $\Delta R(\ell, E_T^{miss})$  influence, this is not to be expected for a well suited variable.

An addition to the 2D  $(\Delta m_Z, \Delta R(\ell, \ell))$  reference histogram method as it is could be a combined implementation with the leptonic-side top quark reconstruction method for three lepton events. Producing a recommendation for a lepton to be used in the reconstruction of the single leptonically decaying W boson from one of the top quarks, this information could be utilized in order to suppress the chance of the respective lepton to be chosen by the reference histogram method for the Z boson reconstruction and vice versa. Furthermore, the application of multivariate methods for the Z boson reconstruction could be researched as an additional option to be used in conjunction with a reference histogram based reconstruction strategy or on its own.

However, with this analysis proving the presented 2D  $(\Delta m_Z, \Delta R(\ell, \ell))$  reference histogram method to be superior to the currently employed strategy for the reconstruction of leptonically decaying Z bosons, a strong incentive for implementing it into any next iteration of the ATLAS-CONF-2020-028 analysis [5] is given.

# A | Appendix

## A.1 Previously used three lepton signal regions

Before the employment of three lepton regions supported by pseudo-continuous b-tagging in the ATLAS-CONF-2020-028 analysis [5], summarized in tables 5.3, the ones described in table A.1 were used in combination with the non-PCBT, differential signal region which is still in use now.

All three of these signal regions are designed for inclusive measurements and demand exactly three leptons of the first and second fermion generations, which have to include at least one OSSF lepton pair of a combined mass within a 10 GeV mass window around the Z boson mass  $m_Z$ . Furthermore, ordered by their transverse momenta, they have to exceed 27, 20 and 20 GeV, respectively, while the mass of any additional OSSF lepton pair has to be greater than 10 GeV. The amount of detected jets and b-jets differentiates the signal regions among each other. Either exactly three jets, one of which is b-tagged at an 85% working point, or more 4 jets are required. In the case of more than 4 jets, the signal regions' requirements are split up into exactly one or more than two to be tagged as originating from a b quark at an 85% working point as well.

| Variable                         | $3l\text{-}Z\text{-}2b3j$<br>inclusive  | $3l\text{-}Z\text{-}1b4j$<br>inclusive | $3l\text{-}Z\text{-}2b4j$<br>inclusive |
|----------------------------------|---|--|--|
| $N_l(l = e, \mu)$                | = 3   |  |  |
|                                  | $\geq 1$ OSSF lepton pair with $ m_{ll}^Z - m_Z  < 10$ GeV<br>for all OSSF combinations: $m_{\text{OSSF}} > 10$ GeV |  |  |
| $p_T(l_1, l_2, l_3)$             | > 27, 20, 20 GeV  |  |  |
| $N_{jets}(p_T > 25 \text{ GeV})$ | = 3   | $\geq 4$                               | $\geq 4$                               |
| $N_{b\text{-}jets}$              | = 1 @ 85%   | = 1 @ 85%                              | $\geq 2$ @ 85%                         |

Table A.1: Previously used three lepton signal regions.

## A.2 Signal region specific efficiencies for superior reconstruction methods

In this appendix section the efficiencies of the individual signal regions from tables 5.3 and 5.4 for each method that was tested but not further discussed due to superior performance in comparison to the 2D  $(\Delta m_Z, \Delta R(\ell, \ell))$  reference histogram method.

### Initial method signal region efficiencies

| signal region |                | $3l-Z-1b4j$ -PCBT<br>efficiency | $3l-Z-2b3j$ -PCBT<br>efficiency | $3l-Z-2b3j$ -diff<br>efficiency |
|---------------|----------------|---------------------------------|---------------------------------|---------------------------------|
| 3L            | $eee$          | 97.15%                          | 96.86%                          | 97.06%                          |
|               | $e\epsilon\mu$ | 99.87%                          | 99.92%                          | 99.91%                          |
|               | $e\mu\mu$      | 99.87%                          | 99.91%                          | 99.89%                          |
|               | $\mu\mu\mu$    | 96.29%                          | 96.50%                          | 96.48%                          |

Table A.2: Efficiencies of the initial method for correct Z boson reconstruction in different three lepton signal regions.

| signal region |                   | $4l-DF-1b$<br>efficiency | $4l-DF-2b$<br>efficiency | $4l-SF-1b$<br>efficiency | $4l-SF-2b$<br>efficiency |
|---------------|-------------------|--------------------------|--------------------------|--------------------------|--------------------------|
| 4L            | $eeee$            | 84.62%                   | 100%                     | 93.41%                   | 90.32%                   |
|               | $ee\epsilon\mu$   | 95.46%                   | 95.00%                   | 96.58%                   | 97.37%                   |
|               | $e\epsilon\mu\mu$ | 95.65%                   | 86.67%                   | 95.55%                   | 96.68%                   |
|               | $e\mu\mu\mu$      | 90.41%                   | 100%                     | 97.03%                   | 97.46%                   |
|               | $\mu\mu\mu\mu$    | 85.11%                   | 92.86%                   | 91.36%                   | 89.94%                   |

Table A.3: Efficiencies of the initial method for correct Z boson reconstruction in different four lepton signal regions.

1D  $\Delta m_Z$  method signal region efficiencies

| signal region | $3l-Z-1b4j$ -PCBT<br>efficiency | $3l-Z-2b3j$ -PCBT<br>efficiency | $3l-Z-2b3j$ -diff<br>efficiency |        |
|---------------|---------------------------------|---------------------------------|---------------------------------|--------|
| 3L            | $eee$                           | 97.13%                          | 96.89%                          | 97.09% |
|               | $ee\mu$                         | 99.87%                          | 99.93%                          | 99.91% |
|               | $e\mu\mu$                       | 99.86%                          | 99.90%                          | 99.88% |
|               | $\mu\mu\mu$                     | 96.24%                          | 96.55%                          | 96.50% |

Table A.4: Efficiencies of the 1D ( $\Delta m_Z$ ) method for correct Z boson reconstruction in different three lepton signal regions.

| signal region | $4l-DF-1b$<br>efficiency | $4l-DF-2b$<br>efficiency | $4l-SF-1b$<br>efficiency | $4l-SF-2b$<br>efficiency |        |
|---------------|--------------------------|--------------------------|--------------------------|--------------------------|--------|
| 4L            | $eeee$                   | 84.62%                   | 100%                     | 93.16%                   | 90.20% |
|               | $ee\mu\mu$               | 95.45%                   | 95.00%                   | 96.37%                   | 97.40% |
|               | $e\mu\mu\mu$             | 95.65%                   | 86.67%                   | 95.78%                   | 96.74% |
|               | $e\mu\mu\mu$             | 90.41%                   | 100%                     | 96.95%                   | 97.55% |
|               | $\mu\mu\mu\mu$           | 87.23%                   | 92.86%                   | 91.17%                   | 90.20% |

Table A.5: Efficiencies of the 1D ( $\Delta m_Z$ ) method for correct Z boson reconstruction in different four lepton signal regions.

1D  $\Delta R(\ell, \ell)$  method signal region efficiencies

| signal region |             | $3l\text{-}Z\text{-}1b4j\text{-PCBT}$<br>efficiency | $3l\text{-}Z\text{-}2b3j\text{-PCBT}$<br>efficiency | $3l\text{-}Z\text{-}2b3j\text{-diff}$<br>efficiency |
|---------------|-------------|---|---|---|
| 3L            | $eee$       | 70.31%  | 70.01%  | 69.95%  |
|               | $eem$       | 98.62%  | 98.93%  | 98.85%  |
|               | $e\mu\mu$   | 98.93%  | 99.09%  | 98.99%  |
|               | $\mu\mu\mu$ | 69.54%  | 70.00%  | 69.57%  |

Table A.6: Efficiencies of the 1D ( $\Delta R(\ell, \ell)$ ) method for correct Z boson reconstruction in different three lepton signal regions.

| signal region |                | $4l\text{-}DF\text{-}1b$<br>efficiency | $4l\text{-}DF\text{-}2b$<br>efficiency | $4l\text{-}SF\text{-}1b$<br>efficiency | $4l\text{-}SF\text{-}2b$<br>efficiency |
|---------------|----------------|--|--|--|--|
| 4L            | $eeee$         | 38.46%                                 | 28.57%                                 | 43.83%                                 | 46.62%                                 |
|               | $eeem$         | 54.55%                                 | 55.00%                                 | 68.98%                                 | 69.08%                                 |
|               | $eem\mu$       | 50.00%                                 | 66.67%                                 | 72.17%                                 | 70.21%                                 |
|               | $e\mu\mu\mu$   | 52.05%                                 | 51.85%                                 | 67.81%                                 | 66.48%                                 |
|               | $\mu\mu\mu\mu$ | 44.68%                                 | 35.71%                                 | 47.09%                                 | 45.36%                                 |

Table A.7: Efficiencies of the 1D ( $\Delta R(\ell, \ell)$ ) method for correct Z boson reconstruction in different four lepton signal regions.

1D  $\Delta R(\ell, E_T^{miss})$  method signal region efficiencies

| signal region | $3l\text{-}Z\text{-}1b4j\text{-}PCBT$<br>efficiency | $3l\text{-}Z\text{-}2b3j\text{-}PCBT$<br>efficiency | $3l\text{-}Z\text{-}2b3j\text{-}diff$<br>efficiency |        |
|---------------|---|---|---|--------|
| 3L            | $eee$   | 49.29%  | 49.41%  | 49.54% |
|               | $ee\mu$   | 98.06%  | 98.20%  | 98.19% |
|               | $e\mu\mu$   | 98.19%  | 98.42%  | 98.29% |
|               | $\mu\mu\mu$   | 50.29%  | 49.33%  | 49.54% |

Table A.8: Efficiencies of the 1D ( $\Delta R(\ell, E_T^{miss})$ ) method for correct Z boson reconstruction in different three lepton signal regions.

| signal region | $4l\text{-}DF\text{-}1b$<br>efficiency | $4l\text{-}DF\text{-}2b$<br>efficiency | $4l\text{-}SF\text{-}1b$<br>efficiency | $4l\text{-}SF\text{-}2b$<br>efficiency |        |
|---------------|--|--|--|--|--------|
| 4L            | $eeee$                                 | 15.38%                                 | 28.57%                                 | 25.52%                                 | 23.89% |
|               | $ee\mu\mu$                             | 18.18%                                 | 45.00%                                 | 48.58%                                 | 49.22% |
|               | $e\mu\mu\mu$                           | 26.09%                                 | 33.33%                                 | 50.39%                                 | 50.01% |
|               | $e\mu\mu\mu$                           | 28.77%                                 | 33.33%                                 | 50.75%                                 | 51.25% |
|               | $\mu\mu\mu\mu$                         | 17.02%                                 | 7.14%                                  | 25.90%                                 | 24.90% |

Table A.9: Efficiencies of the 1D ( $\Delta R(\ell, E_T^{miss})$ ) method for correct Z boson reconstruction in different four lepton signal regions.

**2D  $\Delta m_Z, \Delta R(\ell, E_T^{miss})$  method signal region efficiencies**

| signal region | $3l\text{-}Z\text{-}1b4j\text{-PCBT}$<br>efficiency | $3l\text{-}Z\text{-}2b3j\text{-PCBT}$<br>efficiency | $3l\text{-}Z\text{-}2b3j\text{-diff}$<br>efficiency |        |
|---------------|---|---|---|--------|
| 3L            | $eee$   | 96.73%  | 96.85%  | 96.91% |
|               | $eem$   | 99.84%  | 99.94%  | 99.91% |
|               | $e\mu\mu$   | 99.86%  | 99.90%  | 99.88% |
|               | $\mu\mu\mu$   | 96.31%  | 96.36%  | 96.34% |

Table A.10: Efficiencies of the 2D ( $\Delta m_Z, \Delta R(\ell, E_T^{miss})$ ) method for correct Z boson reconstruction in different three lepton signal regions.

| signal region | $4l\text{-}DF\text{-}1b$<br>efficiency | $4l\text{-}DF\text{-}2b$<br>efficiency | $4l\text{-}SF\text{-}1b$<br>efficiency | $4l\text{-}SF\text{-}2b$<br>efficiency |        |
|---------------|--|--|--|--|--------|
| 4L            | $eeee$                                 | 76.92%                                 | 100%                                   | 93.41%                                 | 89.86% |
|               | $eeem$                                 | 95.45%                                 | 90.00%                                 | 96.74%                                 | 97.31% |
|               | $eem\mu$                               | 95.65%                                 | 80.00%                                 | 95.41%                                 | 96.18% |
|               | $e\mu\mu\mu$                           | 90.41%                                 | 100%                                   | 96.79%                                 | 97.17% |
|               | $\mu\mu\mu\mu$                         | 80.11%                                 | 92.86%                                 | 90.84%                                 | 89.83% |

Table A.11: Efficiencies of the 2D ( $\Delta m_Z, \Delta R(\ell, E_T^{miss})$ ) method for correct Z boson reconstruction in different four lepton signal regions.

**3D  $\Delta m_Z, \Delta R(\ell, \ell), \Delta R(\ell, E_T^{miss})$  method signal region efficiencies**

| signal region | 3l-Z-1b4j-PCBT<br>efficiency | 3l-Z-2b3j-PCBT<br>efficiency | 3l-Z-2b3j-diff<br>efficiency |        |
|---------------|------------------------------|------------------------------|------------------------------|--------|
| 3L            | $eee$                        | 97.30%                       | 97.20%                       | 97.34% |
|               | $ee\mu$                      | 99.90%                       | 99.95%                       | 99.94% |
|               | $e\mu\mu$                    | 99.90%                       | 99.92%                       | 99.91% |
|               | $\mu\mu\mu$                  | 96.53%                       | 96.71%                       | 96.70% |

Table A.12: Efficiencies of the 3D ( $\Delta m_Z, \Delta R(\ell, \ell), \Delta R(\ell, E_T^{miss})$ ) method for correct Z boson reconstruction in different three lepton signal regions.

| signal region | 4l-DF-1b<br>efficiency | 4l-DF-2b<br>efficiency | 4l-SF-1b<br>efficiency | 4l-SF-2b<br>efficiency |        |
|---------------|------------------------|------------------------|------------------------|------------------------|--------|
| 4L            | $eeee$                 | 84.62%                 | 100%                   | 93.65%                 | 90.40% |
|               | $eee\mu$               | 97.73%                 | 95.00%                 | 96.74%                 | 97.43% |
|               | $ee\mu\mu$             | 97.83%                 | 100%                   | 95.97%                 | 96.63% |
|               | $e\mu\mu\mu$           | 93.15%                 | 92.59%                 | 96.63%                 | 97.17% |
|               | $\mu\mu\mu\mu$         | 87.23%                 | 92.86%                 | 92.68%                 | 91.38% |

Table A.13: Efficiencies of the 3D ( $\Delta m_Z, \Delta R(\ell, \ell), \Delta R(\ell, E_T^{miss})$ ) method for correct Z boson reconstruction in different four lepton signal regions.



# List of Figures

|      |   |    |
|------|---|----|
| 2.1  | Interactions of the Standard Model particles [12]. . . . .  | 5  |
| 2.2  | Lowest-order Feynman diagrams of single top quark production [15]. . . . .                            | 9  |
| 2.3  | Lowest-order Feynman diagrams of top quark pair production [15]. . . . .                              | 10 |
| 2.4  | Decay channels of a top quark. . . . .  | 11 |
| 2.5  | Branching ratios and first order Feynman diagrams of $t\bar{t}$ decay channels [15].                  | 11 |
| 2.6  | neutrino-electron scattering. . . . .   | 13 |
| 2.7  | Z boson production through annihilation of particle-anti-particle pairs of leptons or quarks. . . . . | 14 |
| 2.8  | Emission of Z boson by a sufficiently energetic quark. . . . .  | 14 |
| 2.9  | Higgs boson decay into two Z bosons leading to a four lepton final state. . .                         | 15 |
| 2.10 | Z boson decay channels with respective branching ratios. . . . .                                      | 15 |
| 2.11 | Main production channels for $t\bar{t}Z$ events in hadron colliders. . . . .                          | 16 |
| 2.12 | Total branching ratio of the decay of $t\bar{t}Z$ events. . . . .                                     | 17 |
| 3.1  | CERN Accelerator Complex [27]. . . . .  | 19 |
| 3.2  | The ATLAS Detector [30]. . . . .  | 21 |
| 4.1  | Simulation process of a proton-proton collision [41]. . . . .   | 28 |
| 4.2  | Bin migration matrix. . . . .   | 32 |
| 5.1  | Decay of tauons via weak interaction into leptons or quarks. . . . .                                  | 36 |
| 5.2  | Bin migration matrix after decay channel selection and signal regions. . . . .                        | 39 |
| 5.3  | Selected $t\bar{t}Z$ decay channels. . . . .  | 40 |
| 5.4  | Branching ratios of the selected $t\bar{t}Z$ decay channels. . . . .                                  | 41 |
| 6.1  | Initial three lepton event efficiencies of the Z boson reconstruction. . . . .                        | 44 |
| 6.2  | Initial four lepton event efficiencies of the Z boson reconstruction. . . . .                         | 44 |
| 6.3  | $\Delta m_Z$ truth-level testing for three lepton events. . . . .                                     | 48 |
| 6.4  | $\Delta m_Z$ truth-level testing for four lepton events. . . . .                                      | 48 |
| 6.5  | $\Delta R(\ell, \ell)$ truth-level testing for three lepton events. . . . .                           | 49 |
| 6.6  | $\Delta R(\ell, \ell)$ truth-level testing for four lepton events. . . . .                            | 50 |
| 6.7  | $E_T^{miss}$ of correctly and incorrectly reconstructed events. . . . .                               | 51 |
| 6.8  | $\Delta R(\ell, E_T^{miss})$ truth-level testing for three lepton events. . . . .                     | 52 |
| 6.9  | $\Delta R(\ell, E_T^{miss})$ truth-level testing for four lepton events. . . . .                      | 52 |

|      |  |    |
|------|--|----|
| 6.10 | $\Delta R(Z_{\ell\ell}, E_T^{miss})$ truth-level testing for three lepton events. . . . .  | 53 |
| 6.11 | $\Delta R(Z_{\ell\ell}, E_T^{miss})$ truth-level testing for four lepton events. . . . .   | 54 |
| 6.12 | $\frac{p_{T\ell_1}}{p_{T\ell_2}}$ truth-level testing for three lepton events. . . . .   | 55 |
| 6.13 | $\frac{p_{T\ell_1}}{p_{T\ell_2}}$ truth-level testing for four lepton events. . . . .  | 55 |
| 6.14 | D ( $\Delta m_Z$ ) reference histogram. . . . .  | 57 |
| 6.15 | 1D $\Delta R(\ell, \ell)$ reference histogram. . . . .   | 57 |
| 6.16 | 1D $\Delta R(\ell, E_T^{miss})$ reference histogram. . . . .   | 58 |
| 6.17 | 2D ( $\Delta m_Z, \Delta R(\ell, \ell)$ ) reference histogram. . . . .   | 59 |
| 6.18 | 2D ( $\Delta m_Z, \Delta R(\ell, E_T^{miss})$ ) reference histogram. . . . .   | 59 |
| 6.19 | Masked1D ( $\Delta m_Z$ ) reference histogram. . . . .   | 61 |
| 6.20 | Masked 1D $\Delta R(\ell, \ell)$ reference histogram. . . . .  | 61 |
| 6.21 | Masked 1D $\Delta R(\ell, E_T^{miss})$ reference histogram. . . . .  | 62 |
| 6.22 | Masked 2D ( $\Delta m_Z, \Delta R(\ell, \ell)$ ) reference histogram. . . . .  | 63 |
| 6.23 | Masked 2D ( $\Delta m_Z, \Delta R(\ell, E_T^{miss})$ ) reference histogram. . . . .  | 63 |
| 6.24 | Z boson reconstruction efficiencies of the 1D ( $\Delta m_Z$ ) reference histogram for three lepton events. . . . .  | 66 |
| 6.25 | Z boson reconstruction efficiencies of the 1D ( $\Delta m_Z$ ) reference histogram for four lepton events. . . . .   | 66 |
| 6.26 | Z boson reconstruction efficiencies of the 1D ( $\Delta R(\ell, \ell)$ ) reference histogram for three lepton events. . . . .  | 67 |
| 6.27 | Z boson reconstruction efficiencies of the 1D ( $\Delta R(\ell, \ell)$ ) reference histogram for four lepton events. . . . .   | 68 |
| 6.28 | Z boson reconstruction efficiencies of the 1D ( $\Delta R(\ell, E_T^{miss})$ ) reference histogram for three lepton events. . . . .                                      | 69 |
| 6.29 | Z boson reconstruction efficiencies of the 1D ( $\Delta R(\ell, E_T^{miss})$ ) reference histogram for four lepton events. . . . .                                       | 69 |
| 6.30 | Z boson reconstruction efficiencies of the 2D ( $\Delta m_Z, \Delta R(\ell, \ell)$ ) reference histogram for three lepton events. . . . .                                | 70 |
| 6.31 | Z boson reconstruction efficiencies of the 2D ( $\Delta m_Z, \Delta R(\ell, \ell)$ ) reference histogram for four lepton events. . . . .                                 | 71 |
| 6.32 | Z boson reconstruction efficiencies of the 2D ( $\Delta m_Z, \Delta R(\ell, E_T^{miss})$ ) reference histogram for three lepton events. . . . .                          | 71 |
| 6.33 | Z boson reconstruction efficiencies of the 2D ( $\Delta m_Z, \Delta R(\ell, E_T^{miss})$ ) reference histogram for four lepton events. . . . .                           | 72 |
| 6.34 | Z boson reconstruction efficiencies of the 3D ( $\Delta m_Z, \Delta R(\ell, \ell), \Delta R(\ell, E_T^{miss})$ ) reference histogram for three lepton events. . . . .    | 73 |
| 6.35 | Z boson reconstruction efficiencies of the 3D ( $\Delta m_Z, \Delta R(\ell, \ell), \Delta R(\ell, E_T^{miss})$ ) reference histogram for four lepton events. . . . .     | 73 |
| 6.36 | Z boson reconstruction efficiencies of the 2D ( $\Delta m_Z, \Delta R(\ell, \ell)$ ) method for three lepton events while old three lepton signal regions apply. . . . . | 77 |

# List of Tables

|     |   |    |
|-----|---|----|
| 2.1 | Fermions of the Standard Model [10, 11]. . . . .  | 4  |
| 2.2 | Masses of fermions [10]. . . . .  | 5  |
| 2.3 | Bosons of the SM [10]. . . . .  | 6  |
| 4.1 | List of used Monte Carlo samples. . . . .   | 30 |
| 5.1 | Electron and muon definitions according to [5]. . . . .   | 34 |
| 5.2 | Jet definitions according to [5]. . . . .   | 34 |
| 5.3 | Three lepton signal regions from [5]. . . . .   | 38 |
| 5.4 | Four lepton signal regions from [5]. . . . .  | 38 |
| 6.1 | Comparison between the initial and the new 2D ( $\Delta m_Z, \Delta R(\ell, \ell)$ ) method for Z boson reconstruction. . . . .                                       | 74 |
| 6.2 | Comparison between the initial and the new 1D ( $\Delta m_Z$ ) method for Z boson reconstruction. . . . .   | 75 |
| 6.3 | Efficiencies of the 2D ( $\Delta m_Z, \Delta R(\ell, \ell)$ ) method for correct Z boson reconstruction in different three lepton signal regions. . . . .             | 76 |
| 6.4 | Efficiencies of the 2D ( $\Delta m_Z, \Delta R(\ell, \ell)$ ) method for correct Z boson reconstruction in different four lepton signal regions. . . . .              | 77 |
| 6.5 | Comparison between the 2D ( $\Delta m_Z, \Delta R(\ell, \ell)$ ) method's efficiency for Z boson reconstruction with new and old three lepton signal regions. . . . . | 78 |
| 6.6 | Efficiencies of the 2D ( $\Delta m_Z, \Delta R(\ell, \ell)$ ) method for correct Z boson reconstruction in the old three lepton signal regions. . . . .               | 78 |
| 6.7 | Comparison between the initial and the new 1D ( $\Delta m_Z$ ) method for Z boson reconstruction. . . . .   | 79 |
| 6.8 | Comparison between the initial and the new 1D ( $\Delta m_Z$ ) method for Z boson reconstruction. . . . .   | 80 |
| A.1 | Previously used three lepton signal regions. . . . .  | 83 |
| A.2 | Efficiencies of the initial method for correct Z boson reconstruction in different three lepton signal regions. . . . .   | 84 |
| A.3 | Efficiencies of the initial method for correct Z boson reconstruction in different four lepton signal regions. . . . .  | 84 |

|      |   |    |
|------|---|----|
| A.4  | Efficiencies of the 1D ( $\Delta m_Z$ ) method for correct Z boson reconstruction in different three lepton signal regions. . . . .   | 85 |
| A.5  | Efficiencies of the 1D ( $\Delta m_Z$ ) method for correct Z boson reconstruction in different four lepton signal regions. . . . .  | 85 |
| A.6  | Efficiencies of the 1D ( $\Delta R(\ell, \ell)$ ) method for correct Z boson reconstruction in different three lepton signal regions. . . . .   | 86 |
| A.7  | Efficiencies of the 1D ( $\Delta R(\ell, \ell)$ ) method for correct Z boson reconstruction in different four lepton signal regions. . . . .  | 86 |
| A.8  | Efficiencies of the 1D ( $\Delta R(\ell, E_T^{miss})$ ) method for correct Z boson reconstruction in different three lepton signal regions. . . . .                                   | 87 |
| A.9  | Efficiencies of the 1D ( $\Delta R(\ell, E_T^{miss})$ ) method for correct Z boson reconstruction in different four lepton signal regions. . . . .                                    | 87 |
| A.10 | Efficiencies of the 2D ( $\Delta m_Z, \Delta R(\ell, E_T^{miss})$ ) method for correct Z boson reconstruction in different three lepton signal regions. . . . .                       | 88 |
| A.11 | Efficiencies of the 2D ( $\Delta m_Z, \Delta R(\ell, E_T^{miss})$ ) method for correct Z boson reconstruction in different four lepton signal regions. . . . .                        | 88 |
| A.12 | Efficiencies of the 3D ( $\Delta m_Z, \Delta R(\ell, \ell), \Delta R(\ell, E_T^{miss})$ ) method for correct Z boson reconstruction in different three lepton signal regions. . . . . | 89 |
| A.13 | Efficiencies of the 3D ( $\Delta m_Z, \Delta R(\ell, \ell), \Delta R(\ell, E_T^{miss})$ ) method for correct Z boson reconstruction in different four lepton signal regions. . . . .  | 89 |

# Bibliography

- [1] Joseph John Thomson. Discovery of the electron. *Philosophical Magazine*, 44:93, 1897.
- [2] ATLAS Collaboration et al. Observation of a new particle in the search for the standard model higgs boson with the atlas detector at the lhc. *Physics Letters B*, 716(1):1–29, 2012.
- [3] CMS Collaboration et al. Observation of a new boson at a mass of 125 gev with the cms experiment at the lhc. *Physics Letters B*, 716(1):30–61, 2012.
- [4] M. L. Perl et al. Evidence for anomalous lepton production in  $e^+ - e^-$  annihilation. *Phys. Rev. Lett.*, 35:1489–1492, Dec 1975.
- [5] ATLAS Collaboration et al. Measurements of the inclusive and differential production cross sections of a top-quark-antiquark pair in association with a  $Z$  boson at  $\sqrt{s} = 13$  TeV with the ATLAS detector. Technical Report ATLAS-CONF-2020-028, CERN, Geneva, Aug 2020.
- [6] Gerhard Ecker. *Teilchen, Felder, Quanten: Von der Quantenmechanik zum Standardmodell der Teilchenphysik*. Springer-Verlag, 2017.
- [7] Lim Chong-sa, Morii Toshiyuki, and Mukherjee Shankar Nath. *The physics of the standard model and beyond*. World Scientific, 2004.
- [8] David Griffiths. *Introduction to elementary particles*. John Wiley & Sons, 2008.
- [9] Super-Kamiokande Collaboration et al. Y. Fukuda et al., evidence for oscillation of atmospheric neutrinos. *Phys. Rev. Lett*, 81(8):1562–1567, 1998.
- [10] Particle Data Group, PA Zyla, RM Barnett, J Beringer, O Dahl, DA Dwyer, DE Groom, C-J Lin, KS Lugovsky, E Pianori, et al. Review of particle physics. *Progress of Theoretical and Experimental Physics*, 2020(8):083C01, 2020.
- [11] Bogdan Povh, Klaus Rith, Christoph Scholz, and Frank Zetsche. *Teilchen und Kerne: eine Einführung in die physikalischen Konzepte*. Springer-Verlag, 2006.
- [12] Eric Drexler. Summary of interactions between particles described by the standard model — Wikipedia, the free encyclopedia, 2014. [Online; accessed 25-August-2020].

- [13] M Herrero. The standard model. In *Techniques and Concepts of High Energy Physics X*, pages 1–59. Springer, 1999.
- [14] C. S. Wu, E. Ambler, R. W. Hayward, D. D. Hoppes, and R. P. Hudson. Experimental test of parity conservation in beta decay. *Phys. Rev.*, 105:1413–1415, Feb 1957.
- [15] Maximilian Riepe. Studien zur Verbesserung der Zuordnung von Zerfallsteilchen zu Top-Quarks, 2018.
- [16] Christine Sutton and Robert Curley. Electroweak theory. 2006. [Online; accessed 25-August-2020].
- [17] K. Kodama et al. Observation of tau neutrino interactions. *Physics Letters B*, 504(3):218 – 224, 2001.
- [18] S. Abachi et al. Observation of the top quark. *Phys. Rev. Lett.*, 74:2632–2637, Apr 1995.
- [19] ATLAS Collaboration et al. Evidence for  $t\bar{t}\bar{t}$  production in the multilepton final state in proton-proton collisions at  $\sqrt{s} = 13$  TeV with the ATLAS detector. Technical Report ATLAS-CONF-2020-013, CERN, Geneva, Jun 2020.
- [20] FJ Hasert et al. Observation of neutrino-like interactions without muon or electron in the gargamelle neutrino experiment. *Nuclear Physics B*, 73(1):1–22, 1974.
- [21] G Arnison, A Astbury, B Aubert, C Bacci, G Bauer, A Bezaguet, R Böck, TJV Bowcock, M Calvetti, P Catz, et al. Experimental observation of lepton pairs of invariant mass around 95 gev/c<sup>2</sup> at the cern sps collider. *Physics Letters B*, 126(5):398–410, 1983.
- [22] M Banner et al. Observation of single isolated electrons of high transverse momentum in events with missing transverse energy at the cern  $\bar{p}p$  collider. *Phys. Lett. B*, 122(CERN-EP-83-25):476–485, 1983.
- [23] A Salvucci. Recent higgs  $\rightarrow zz^{(*)} \rightarrow 4l$  results with the atlas experiment. *Il nuovo cimento C*, 36(6):283–290, 2013.
- [24] Florian Fischer. Studies on the measurement of the  $\bar{t}tZ$  production cross section in the 1-lepton channel at 13TeV mit dem ATLAS detektor, 2017.
- [25] Alessandro Broggio, Andrea Ferroglia, Rikkert Frederix, Davide Pagani, Benjamin D Pecjak, and Ioannis Tsinikos. Top-quark pair hadroproduction in association with a heavy boson at nlo+ nml including ew corrections. *Journal of High Energy Physics*, 2019(8):39, 2019.
- [26] CERN. About: <https://home.cern/about>, 2020. [Online; accessed 25-August-2020].
- [27] CERN. Accelerator Complex CERN, 2020. [Online; accessed 25-August-2020].

- [28] ATLAS Collaboration et al. Expected performance of the atlas experiment-detector, trigger and physics. Technical report, SLAC National Accelerator Laboratory (SLAC), 2011.
- [29] ATLAS Collaboration et al. Atlas detector and physics performance technical design report. *CERN/LHCC*, 15:1999, 1999.
- [30] Joao Pequenao. The ATLAS Detector, 2008. [Online; accessed 25-August-2020].
- [31] M Capeans, T Flick, R Vuillermet, G Darbo, H Pernegger, K Einsweiler, M Garcia-Sciveres, M Elsing, O Rohne, and C Gemme. Atlas insertable b-layer technical design report. Technical report, ATLAS-TDR-019, 2010.
- [32] ATLAS Collaboration et al. Inner detector technical design report, vol. ii. Technical report, CERN/LHCC/97-17, 30 April, 1997.
- [33] A Vogel. ATLAS Transition Radiation Tracker (TRT): Straw Tube Gaseous Detectors at High Rates. Technical Report ATL-INDET-PROC-2013-005, CERN, Geneva, Apr 2013.
- [34] Eric Schanet. Sensitivity studies for a search for charginos in final states with one lepton with the ATLAS detector and interpretation of a search for gluinos and squarks in the pmssm, 2018.
- [35] ATLAS Collaboration et al. *ATLAS detector and physics performance: Technical Design Report, 1*. Number CERN-LHCC-99-014. ATLAS-TDR-014, 1999.
- [36] Clive Andrew Edwards. Search for the Higgs Boson in the process  $H \rightarrow ZZ \rightarrow ll\nu\nu$  produced via Vector-Boson Fusion with the ATLAS detector, 2012. Presented in 2012.
- [37] ATLAS Collaboration et al. The atlas experiment at the cern large hadron collider. *Jinst*, 3:S08003, 2008.
- [38] Ed Daw. Special relativity, 2012.
- [39] Andreas Jäger. Analyse von  $d_0$ - $\bar{d}_0$ -mischung mit dem cdf-detektor. 2009.
- [40] Tung-Mow Yan and Sidney D Drell. The parton model and its applications. *International Journal of Modern Physics A*, 29(30):1430071, 2014.
- [41] Matt Dobbs and Jørgen Beck Hansen. The hepmc c++ monte carlo event record for high energy physics. *Computer Physics Communications*, 134(1):41–46, 2001.
- [42] Johan Alwall, R Frederix, S Frixione, V Hirschi, Fabio Maltoni, Olivier Mattelaer, H-S Shao, T Stelzer, P Torrielli, and M Zaro. The automated computation of tree-level and next-to-leading order differential cross sections, and their matching to parton shower simulations. *Journal of High Energy Physics*, 2014(7):79, 2014.

- 
- [43] Torbjörn Sjöstrand, Stefan Ask, Jesper R Christiansen, Richard Corke, Nishita Desai, Philip Ilten, Stephen Mrenna, Stefan Prestel, Christine O Rasmussen, and Peter Z Skands. An introduction to pythia 8.2. *Computer physics communications*, 191:159–177, 2015.
- [44] Andrew Buckley. ATLAS Pythia 8 tunes to 7 TeV data. Technical Report ATL-PHYS-PROC-2014-273, CERN, Geneva, Dec 2014.
- [45] David J Lange. The evtgen particle decay simulation package. *Nuclear Instruments and Methods in Physics Research Section A: Accelerators, Spectrometers, Detectors and Associated Equipment*, 462(1-2):152–155, 2001.
- [46] ATLAS Collaboration et al. Performance of electron and photon triggers in atlas during lhc run 2. *The European Physical Journal C*, 80(1):47, 2020.
- [47] Federico Meloni. Primary vertex reconstruction with the atlas detector. *Journal of Instrumentation*, 11(12):C12060, 2016.
- [48] ATLAS Collaboration et al. Electron efficiency measurements with the atlas detector using 2012 lhc proton–proton collision data. *The European Physical Journal C*, 77(3):195, 2017.
- [49] M Cacciari, GP Salam, and G Soyez. The anti-k t jet clustering algorithm (2008) jhep, 4. *2008JHEP*, 4:063.
- [50] Antonio Miucci, Claudia Merlassino, Sigve Haug, John Kenneth Anders, Hans Peter Beck, Antonio Ereditato, Laura Franconi, and Thomas Daniel Weston. Atlas b-jet identification performance and efficiency measurement with  $t\bar{t}$  events in pp collisions at  $\sqrt{s} = 13$  tev. *The European physical journal. C, Particles and fields*, 79(970), 2019.

# Eidesstattliche Erklärung

Hiermit erkläre ich, die vorliegende Arbeit selbständig verfasst zu haben und keine anderen als die in der Arbeit angegebenen Quellen und Hilfsmittel benutzt zu haben.

München, 10. September 2020

Maximilian Riepe